Electrochemical Behavior of Carbon Nanostructured Electrodes: Graphene, Carbon Nanotubes, and Nanocrystalline Diamond

by

Akshay Sanjay Raut

Department of Electrical and Computer Engineering
Duke University

Date:_____

Approved:

_____
Jeffrey T. Glass, Supervisor

_____
Jie Liu

_____
Martin Brooke

_____
Christopher Dwyer

_____
Edmond Bowden

Dissertation submitted in partial fulfillment of
the requirements for the degree of Doctor
of Philosophy in the Department of
Electrical and Computer Engineering in the Graduate School
of Duke University

2014

ABSTRACT

Electrochemical Behavior of Carbon Nanostructured Electrodes: Graphene, Carbon Nanotubes, and Nanocrystalline Diamond

by

Akshay Sanjay Raut

Department of Electrical and Computer Engineering
Duke University

Date:_____

Approved:

_____
Jeffrey T. Glass, Supervisor

_____
Jie Liu

_____
Martin Brooke

_____
Christopher Dwyer

_____
Edmond Bowden

An abstract of a dissertation submitted in partial fulfillment of the requirements for the degree of Doctor of Philosophy in the Department of Electrical and Computer Engineering in the Graduate School of Duke University

2014

Abstract

The primary goals of this research were to investigate the electrochemical behavior of carbon nanostructures of varying morphology, identify morphological characteristics that improve electrochemical capacitance for applications in energy storage and neural stimulation, and engineer and characterize a boron-doped diamond (BDD) electrode based electrochemical system for disinfection of human liquid waste.

Carbon nanostructures; ranging from vertically aligned multiwalled carbon nanotubes (MWCNTs), graphenated carbon nanotubes (g-CNTs) to carbon nanosheets (CNS); were synthesized using a MPECVD system. The nanostructures were characterized by using scanning electron microscopy (SEM) and Raman spectroscopy. In addition to employing commonly used electrochemical techniques such as cyclic voltammetry (CV) and electrochemical impedance spectroscopy (EIS), a new technique was developed to evaluate the energy and power density of individual electrodes. This facilitated comparison of a variety of electrode materials without having to first develop complex device packaging schemes. It was found that smaller pore size and higher density of carbon foliates on a three-dimensional scaffold of carbon nanotubes increased specific capacitance. A design of experiments (DOE) study was conducted to explore the parametric space of the MWCNT system. A range of carbon nanostructures of varying

morphology were obtained. It was observed that the capacitance was dependent on defect density. Capacitance increased with defect density.

A BDD electrode was characterized for use in a module designed to disinfect human liquid waste as a part of a new advanced energy neutral, water- and additive-free toilet designed for treating waste at the point of source. The electrode was utilized in a batch process system that generated mixed oxidants from ions present in simulated urine and inactivated *E. Coli* bacteria. Among the mixed oxidants, the concentration of chlorine species was measured and was found to correlate to the reduction in *E. Coli* concentration. Finally, a new operating mode was developed that involved pulsing the voltage applied to the BDD anode led to 66% saving in energy required for disinfection and yet successfully reduced *E. Coli* concentration to less than the disinfection threshold.

Dedicated to

My parents, Varsha and Sanjay Raut,

My wife Ketki,

And my sister Priyanka Raut

Contents

List of Tables

List of Figures

Acknowledgements

I would like to thank my advisor Dr. Jeffrey Glass for proving to me that with a passion for science and a deep sense of commitment, a software engineer could indeed become a scientist. He is one of the best teachers I have ever had. He has taught me more about science and management than I could ever recount. I believe that his guidance has made me not just a good researcher but also a much better professional. He gave me the space and time I needed to grow as a graduate student. I will be eternally thankful to him for his guidance and support.

I would like to thank Dr. Brian Stoner for pushing me out of my comfort zone and giving me a truly invaluable real-world experience. I learnt a lot about translating fundamental research to real-world applications. He was present for most of my conference presentations and I drew immense support from that.

Dr. Charles Parker has been as much of a friend as my manager. He was always there to help me with lab work, data analyses and writing papers and my dissertation. Charles was also a source of support for me in my professional and personal life.

I would like to thank Dr. Jeffrey Piascik, Dr. Ethan Klem and Dr. Garry Cunnigham. I learnt a lot about engineering and basic science from them and they made my time at RTI both enriching and fun.

I would also like to thank my colleagues and friends – Dr. Billyde Brown, Dr. Qing Peng, Dr. Jason Amsden, Zachary Russell, Barbara Raynal, Isvar Cordova and

Erich Radauscher for being the perfect lab mates and officemates. It has been a learning experience discussing research as a part of work. Our coffee breaks and e-social have been quite memorable.

I would not be where I am in my life today if it were not for my parents – Varsha and Sanjay Raut. Thank you for helping me realize my true calling and supporting me all the way, sometimes in times of adversity. I owe everything I have to you.

My sister – Priyanka Raut has always been like a compass in my life. She always helped me identify the right direction in life. She boosted me when I was at a low. She is the first and the best friend I have. I will not forget the midnight pep talks that she gave me when I was feeling demotivated and lost.

And last but my no means the least, my loving wife – Ketki. You have been the rock solid foundation of my life for the past 3 years. I cannot imagine how I would have completed my graduate studies without your love, care and sacrifice. You are a worthy stakeholder in my successes.

List of Abbreviations

ALD	-	Atomic layer deposition
BDD	-	Boron doped diamond
CCS	-	Chlorine containing species
CNS	-	Carbon nanosheets
CNT	-	Carbon nanotubes
COD	-	Chemical oxygen demand
CV	-	Cyclic voltammetry
CVD	-	Chemical vapor deposition
DFT	-	Discrete functional theory
DOE	-	Design of experiments
DSA	-	Dimensionally stable anodes
EDGE	-	Electron density of graphene edges
EDLC	-	Electrochemical double layer capacitor
EIS	-	Electrochemical impedance spectroscopy
ESD	-	Energy storage devices
ESR	-	Equivalent series resistance
g-CNT	-	Graphenated carbon nanotubes
HOPG	-	Highly oriented pyrolytic graphite
MPECVD	-	Microwave plasma enhanced chemical vapor deposition
MWCNT	-	Multiwalled carbon nanotubes
OCP	-	Open circuit potential
PEC	-	Photoelectrochemical
ROS	-	Reactive oxygen species
SEM	-	Scanning electron microscopy
SHE	-	Standard hydrogen electrode
SMES	-	Superconducting magnetic energy storage
SWCNT	-	Single walled carbon nanotubes
TEM	-	Transmission electron microscopy
UNCD	-	Ultra nanocrystalline diamond

1 Introduction and Background

1.1 Goals

The principle goal of this study was to investigate the electrochemical behavior of carbon nanostructures of varying morphology — from carbon nanotubes (CNTs) to synthetic diamond — for application in the field of electrochemical energy storage, neural stimulation, and electrochemical disinfection.

First, an electrochemical technique to evaluate the energy and power performance of individual electrodes was required. This facilitated direct comparison of electrodes with varying morphology. The next step varied the morphology of vertically aligned multiwalled carbon nanotubes (MWCNTs) in order to improve capacitive performance. On achieving this, a design of experiments study (DOE) was initiated to investigate the parametric space for sp^2-bonded carbon deposition in a MPECVD system. A variety of carbon nanostructures with widely different morphologies were obtained. Chief amongst these were MWCNTs with graphene-like foliates growing from the sidewalls, termed graphenated CNTs (g-CNTs). g-CNTs combine the high surface area of CNTs and high edge capacitance of graphene. g-CNTs were further studied to understand the effect of these edges on the frequency dependent capacitance. These results combined with the electrochemical results from the DOE enhanced the understanding of the effects of various carbon nanostructure morphologies on electrochemical behavior.

The final goal of this research was to use boron doped diamond (BDD) diamond electrodes for disinfection of human liquid waste. A module was developed as a part of an energy-neutral, water- and additive-free toilet being developed for the less developed world. This included a study of the electrochemical generation of mixed oxidants at a BDD electrode and their effect on bacteria concentration in human liquid waste. Lastly, operating techniques to minimize energy consumption were explored.

1.2 Motivation

Traditional electrolytic (parallel plate) capacitors have high power density but very low energy density. However, batteries have high energy density but low power density. This means that although batteries can run on a single charge for hours, they are not capable of delivering high current, *i.e.*, high-energy delivery, in short time period. This is a big issue today where sustainable energy sources such as wind and solar generate power discontinuously over relatively shorter periods of time. An energy storage device is required that can rapidly capture charge when it is available and deliver it efficiently to loads as required. This also finds application in electric vehicles. Electric vehicles capture energy from braking regeneratively to recharge their batteries to increase their effective range. The absence of a fast-charging energy storage device affects the efficiency of electric vehicles to a great extent. Moreover, battery technology has not progressed as rapidly as semiconductor technology. This has left us with smartphones and tablets that need to be recharged every day or even more frequently.

Carbon nanostructured electrodes have the physical and chemical properties to potentially work as electrodes in an energy storage device that can fit all above requirements. This will require a deeper understanding of these nanostructures and their electrical and electrochemical behavior. This was a significant motivation for me to pursue research in this field.

Millions of people across the world are affected by lack of sanitation and proper hygiene. According to the World Health Organization (1), ~2 billion people across the planet lack access to proper sanitation. This leads to disease and death. Improving sanitation the traditional way will require trillions of dollars of investments in sewage and toilet infrastructure in a world with scarce investment resources. What is required is a novel solution that uses advanced but affordable technology to avoid the spread of disease while treating waste at the point of source without using external energy or water. Carbon nanostructures again hold promise to provide such a solution. Synthetic diamond films have the ability to disinfect wastewater by using solar power. The potential for this technology is immense. The potential to change the lives of millions for the better has been a strong source of inspiration for me.

1.3 Fundamentals of CNTs

Carbon nanotubes in their simplest form can be thought of as graphene planes rolled up to form tubular structures (2). Hence their electronic properties are closely related to graphene. Carbon has the electronic structure $1s^2\ 2s^2\ 2p^2$. Carbon forms a

variety of bonds by promoting one of its 2s electrons to 2p. In graphite, one of these 2s electrons hybridizes with the 2p electrons to form three σ-bonded sp^2 orbitals with an angles of 120°. The remaining electron is in a pz (π) configuration perpendicular to the plane of the other three bonds. This π orbital provides weak van der Waals forces between the planes. The overlap of the π orbitals of adjacent atoms in graphene gives it its relatively high conductivity (3). How a nanotubes inherits these electronic properties of graphene depends greatly upon the axis or direction along which the plane is rolled vis-à-vis its lattice structure. The density of states spectra of single-walled carbon nanotubes (SWCNTs) has a strong dependence on the chirality of the tubes (4). This orientation is quantified by means of a chiral vector $C_h = na_1 + ma_2$ which joins two points on the lattice as shown in Figure 1 (5).

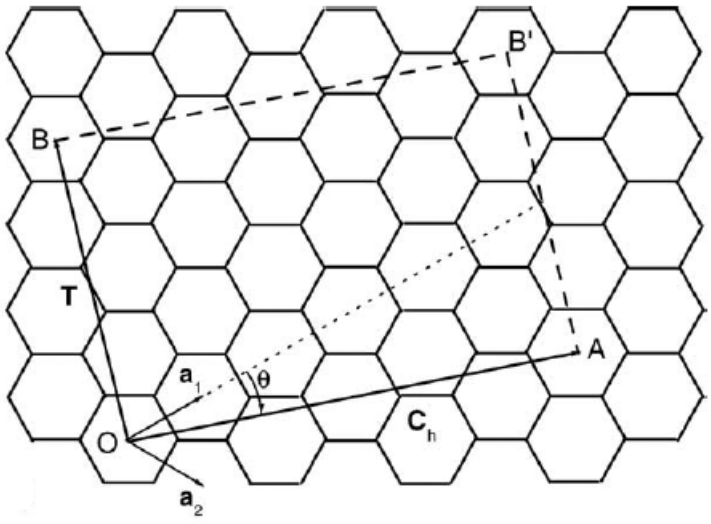

Figure 1: Chiral vector on graphene plane (5)

a_1 and a_2 are the base lattice vectors and n and m are numbers that give the tube their unique structure. A nanotube can be thought to be made by taking a long sectional cut perpendicular to the chiral vector and then rolling the resulting strip to form a hollow tube. The chiral angle θ is the given by the following (3):

$$\theta = \sin^{-1}[\sqrt{3}\, m/(2\sqrt{(n2 + nm + m2)}] \quad \textbf{- 1}$$

The chirality of the tubes change based on this angle which ranges from 0° to 30°. Tubes with θ = 0° are called zigzag tubes while those with θ = 30° are called armchair tubes. All other tubes are called chiral tubes (Figure 2 (5)).

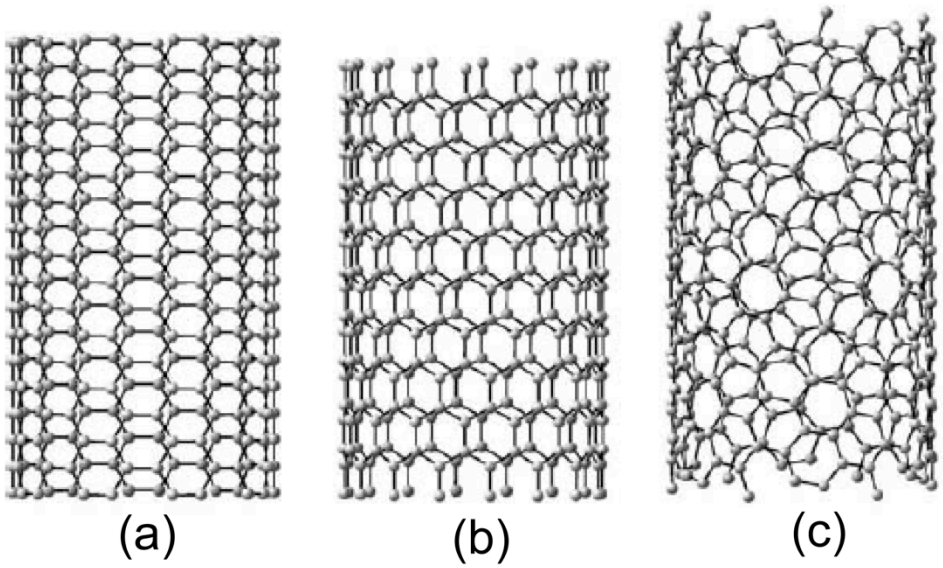

Figure 2: Tubes with different structures (a) Armchair tubes (b) Zigzag tubes (c) Chiral tubes (5)

In general SWNTs with (n,m) an integer multiple of 3 are metallic or semi-metallic while all other tubes are semiconducting (6). MWCNTs in their simplest form consist of parallel graphene planes rolled up to make concentric cylinders. In such a case

the concentric walls are parallel to each other. MWCNTs have been shown to be ballistic conductors at room temperature. This conduction is due 1D transport through the surface layer (7). In what are called the bamboo structured MWCNTs (Figure 3 (8)), the dangling bonds at the ends of the graphite basal planes are passivated by hydrogen passed during the MPECVD growth (9).

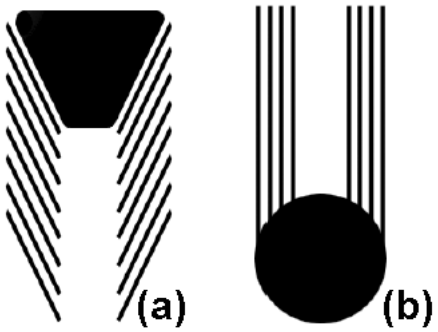

Figure 3: Basal plane alignment in multiwalled CNTs (a) Bamboo structure (b) Perfectly parallel planes (8)

1.4 CNT Growth

Chemical Vapor Deposition (CVD) of CNTs involves decomposition of hydrocarbons in the gas phase onto catalyst particles. In thermal CVD methods, alignment is achieved by the so-called crowding effect where adjacent tubes help alignment due to Van der Waals interaction (8). MPECVD techniques, such as that utilized in the present research, can provide alignment due to the electric field in the glow discharge (10) in addition to crowding. Properties of the catalyst particles dictate the morphology of the tubes to a great extent. The size of the catalyst particle can control the morphology, ranging from the number of walls in a multi-walled tube to the

formation of a bamboo/coned structure (11). Cui, *et al* (12) have shown that the length of the tubes is dependent on the plasma temperature. They have also demonstrated that the inter-bamboo (cone) sub-structure distance is dependent on the ammonia/methane gas ratio and the temperature. Because alignment is not dependent on adjacent van der Waals interaction, free standing or isolated tubes can be grown.

In the MPECVD system utilized in the present research, standing electromagnetic waves were used to strike a glow discharge. Growth occurred on a heated sample stage in a stainless steel chamber (Figure 4 (13)). The substrate was coated with a film of the catalyst material between 1 and 5 nm in thickness and placed in the plasma chamber. In the pretreatment phase, the sample was heated to ~800° C in a hydrogen environment. This results in the dewetting of the catalyst wherein the catalyst "beads up" to form nanoparticles on the substrate surface. A microwave plasma was then struck, which initiated tube growth when methane/acetylene and ammonia gases were passed into the chamber.

The parameters that were controlled during the growth of CNTs in the MPECVD system included gas composition, pressure, temperature, and RF power. Growth happened in 3 phases.

1. Heat up: In this phase the chamber was heated to about 830° C at low pressure.
2. Pre-treatment: In this phase the plasma was struck and gas was released into the chamber. The microwave power is regulated to minimize the reflected power.

3. Growth: In this phase gas with the growth mixture was passed for a defined period of time after which the microwave source was switched off and heating stopped.

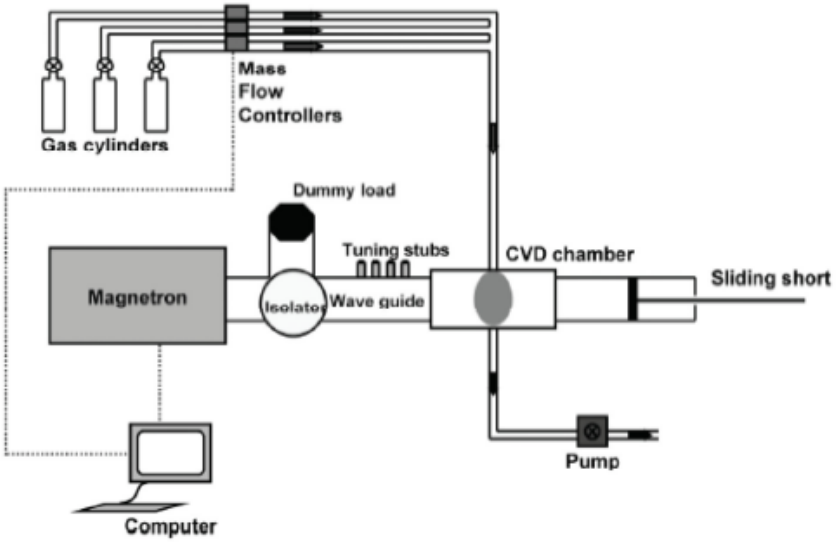

Figure 4: Schematic of a microwave plasma enhanced chemical vapor deposition system (13)

Heat-up, pre-treatment, and growth occur in sequence. The runtime of the growth phase determines the length of the vertically aligned tubes. For the 915 MHz MPECVD used in this research, a growth time of 120 seconds in an ammonia and methane environment yields tube of ~20 μm length.

1.5 The Electrochemical Double Layer

The electrochemical double layer at the interphase between an electrode and an electrolyte is essentially the storage of opposite charges or charged species by application of an external voltage. The voltage causes charges to accumulate on either side of the interface, separated by a small distance (Figure 5 (14)). The maximum charge

density due to electrostatic physisorption is at the outer Helmholtz plane (15). The double layer capacitance is given by,

$$C_{dl} = \varepsilon A/4\pi d \quad \textbf{- 2}$$

And the power is calculated as,

$$P = V^2/4R \quad \textbf{- 3}$$

where V is applied voltage and R is the Equivalent Series Resistance (ESR) in ohms. Thus to improve the performance of a supercapacitor, it is important that the ESR is low and specific capacitance is high (16). Similarly, ESR and the resistivity of the electrolyte also affects the frequency response of the device (17).

It is important to note the difference between Faradaic and Non-Faradaic processes. Processes in which charge accumulation occurs electrostatically, with opposite charges residing on opposite sides of an interface are non-Faradaic. On the other hand, charge storage achieved by electron transfer across the interface that produces a chemical change in the electrode material is faradaic (18).

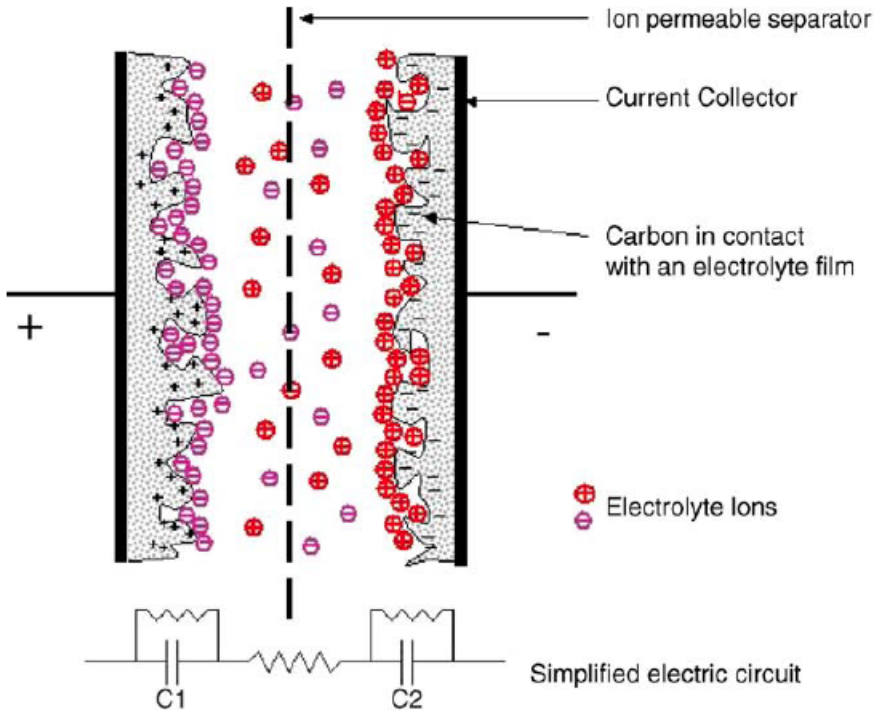

Figure 5: Schematic representation of an electrochemical double layer capacitor in its charged state and its equivalent circuit (14)

1.6 Current State of Development of Supercapacitors

Carbon nanotubes of all varieties (MWCNT and SWCNT) have been used for double layer charge storage. Along with CNTs, a host of other carbon materials such as activated carbon are being used. Amongst commercially available supercapacitors with aqueous electrolytes, energy densities in the range of 6-13 Wh/kg and power densities in the range of 1-5 kW/kg have been reported (19). Supercapacitors using activated carbon have reported specific capacitances in the range of 20-100 F/g (15). The specific capacitance of a two electrode carbon-carbon supercapacitor with electrodes made from MWCNTs (85%), acetylene black (10%) and a binding agent (5%) was reported to be 70

F/g and when treated with nitric acid (69.5%) for 1 hour was 120 F/g (15). Tubes treated with KOH developed cracks and irregularities along the surface while still maintaining the nanotube structure (20).

There is evidence that surface functionalization increases the specific capacitance of MWCNTs in aqueous electrolytes by increasing the hydrophilicity of the tubes. For instance, introduction of carboxyl groups leads to a 3.2x increase in capacitance (21). B. Zhang *et. al.* (22) used nanotubes mixed with polytetrafluoroethylene (PTFE) in 1M lithium perchlorate ($LiCLO_4$) with propylene carbonate as background electrolyte. They reported a high energy density of 20 Wh/kg and an ESR of 14 ohms. Acid-functionalized tubes also tend to exhibit higher capacitance. CNTs activated by a mixture of sulfuric and nitric acid showed a 2.5x increase in capacitance (22).

Another approach to increase performance of CNT-based supercapacitors is the introduction of materials exhibiting pseudocapacitance. Chen *et al* (23) reported a dramatic increase in specific capacitance by adding In_2O_3 nanowires to CNTs. Conducting polymers have also been shown to enhance capacitance. Zhou *et al* (24) obtained a 7x improvement in capacitance by using pyrrole treated SWNTs over buckypaper.

Recent trends have been towards modified CNT electrodes such as by functionalizing tubes and fabricating CNT-based electrodes from polymers and other compounds exhibiting pseudocapacitance. By loading CNTs with transition metal

oxides like ruthenium oxide, the specific capacitance was shown to increase 2x (25). Although CNT-based supercapacitors have reported lower specific capacitance compared to activated carbon supercapacitors, their higher conductivity results in better power density (19).

Recently, a variety of carbon nanostructures have been employed apart from CNTs and activated carbon. Jiang *et al.* (26) have classified the broad types of carbon electrodes that are being used as electrodes for supercapacitor applications based on their dimensionality, conductivity, capacitance, and cost (Figure 6 (26)).

Material	Carbon onions	Carbon nanotubes	Graphene	Activated carbon	Carbide derived carbon	Templated carbon
Dimensionality	0D	1D	2D	3D	3D	3D
Conductivity	High	High	High	Low	Moderate	Low
Volumetric capacitance	Low	Low	Moderate	High	High	Low
Cost	High	High	Moderate	Low	Moderate	High
Structure		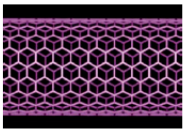	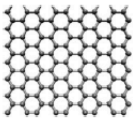	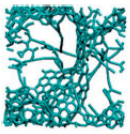	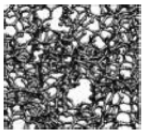	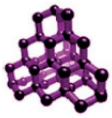

Figure 6: Different types of carbon nanostructures used as electrode material is supercapacitors (26)

Many of these carbon electrodes with different dimensionality are combined along with conductive polymers or pseudocapacitive nanoparticles to enhance capacitance. Table 1 summarizes recent advances in various carbon and non-carbon electrodes for supercapacitors.

Table 1: Summary of recent literature reports for various electrode materials for supercapacitor applications

Reference	Year	Electrode	Setup	Electrolyte type	Specific Capacitance (F/g)
Zhou *et al* (27)	2014	CNT + a-C + Co nanoparticles	3 -terminal	Aqueous	512
Kim *et al* (28)	2013	Activated graphene derived carbon	2 -terminal	Ionic liquid	174
Zhou *et al* (29)	2013	3D CoO on Polypyrrole Nanowire Array	2 –terminal (asymmetric)	Aqueous	2223
Cui *et al* (30)	2014	Mesoporous Graphene Nanofibers	2 –terminal	Non-aqueous	193
Yu *et al* (31)	2014	Porous hollow spheres of NiO nanosheets	3 -terminal	Aqueous	600
Zhang *et al* (32)	2014	Split vertically aligned CNTs	2 - terminal	Aqueous	106
Bai *et al* (33)	2014	Reduced graphene oxide/carbon nanotubes/NiO	3 -terminal	Aqueous	1180

1.7 Fundamentals of Disinfection

Disinfection can be defined as a process designed for the deliberate reduction of the number of pathogenic microorganisms in a given medium (35). The most popular technique for water disinfection is chlorination, which can eliminate most harmful microorganisms (27). Other alternate techniques for disinfection are (1) chemical systems based on ozone, silver, copper, ferrate, iodine, bromine, hydrogen peroxide, and potassium permanganate; (2) physico-chemical means such as photocatalysis; (3) electrochemical disinfection; and (4) physical treatments such as ultraviolet irradiation,

ultrasonication. (36) Amongst these, electrochemical disinfection technology is environmentally friendly, low cost, and can be used to inactivate a variety of bacteria and viruses (36).

Electrochemical disinfection involves generation of disinfecting oxidants from the constituents of the liquid being treated. Specifically, electrochlorination involves the generation of disinfecting species of chlorine such as hypochlorous acid (HClO) and hypochlorite ion (OCl^-) from the chloride ions in the liquid. At the anode, hypochlorous acid/hypochlorite ions are produced as a side reaction to oxygen evolution. Initially, chlorine is produced from chloride ions as:

$$2Cl^- \rightarrow Cl_2 + 2e^-$$

Chlorine reacts with water to yield hypochlorous acid:

$$Cl_2 + H_2O \rightarrow HClO + HCl$$

Hypochlorous acid and the hypochlorite ion have a pH-dependent equilibrium as (Figure 7) (37):

$$HClO \leftrightarrow ClO^- + H^+$$

In disinfection, the sum of the hypochloruous acid and hypochlorite ion is called “free chlorine” or “active chlorine.”

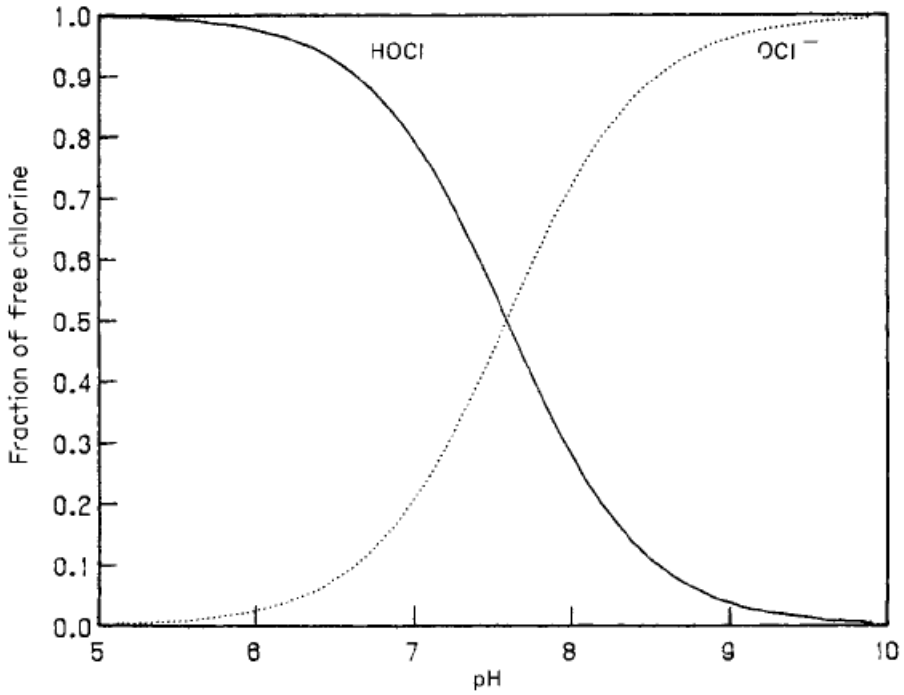

Figure 7: Effect of pH on relative amount of hypochlorous acid and hypochlorite ion at 20° C (37).

During this process, chloride ions that were consumed by free chlorine generation are reformed.

In the presence of ammonia and amino nitrogen compounds, free chlorine reacts to form less biocidal forms. In the presence of ammonium ions, free chlorine reacts in a stepwise manner to form chloramines. The following reactions lead to the formation of three different forms of chloramines:

Monochloramine formation: $NH4^+ + HOCl = \mathbf{NH_2Cl} + H_2O + H^+$

Dichloramine formation: $NH_2Cl + HOCl = \mathbf{NHCl_2} + H_2O$

Trichloramine formation: $NHCl_2 + HOCl = \mathbf{NCl_3} + H_2O$

The chloramines are collectively referred to as combined chlorine. The sum of free and combined chlorine is referred to as total chlorine. Chloramines are disinfectants but their biocidal potency is far less than free chlorine. The formation reactions of the various chloramines are competing reactions that are dependent on pH and controlled to a large extent by the Cl_2:NH_4-N ratio. Figure 8 (37) shows the relative amounts of the three chloramines as a function of pH.

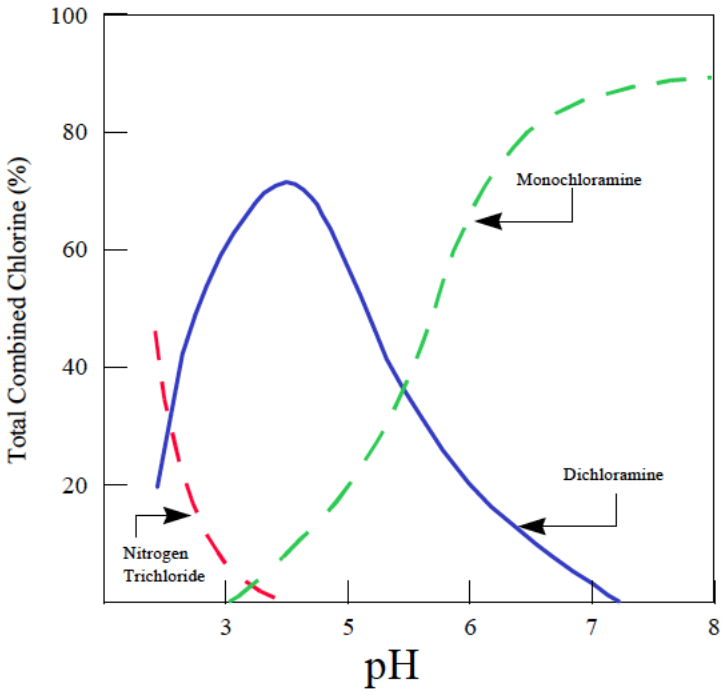

Figure 8: Relative amounts of various chloramines as a function of pH (37)

The stepwise formation behavior of chloramines can be controlled by controlling the Cl_2:NH_4-N ratio. Figure 9 (37) shows the relationship between the three chloramines at varying Cl_2:NH_4-N ratio for pH range of 6.5 – 8.5.

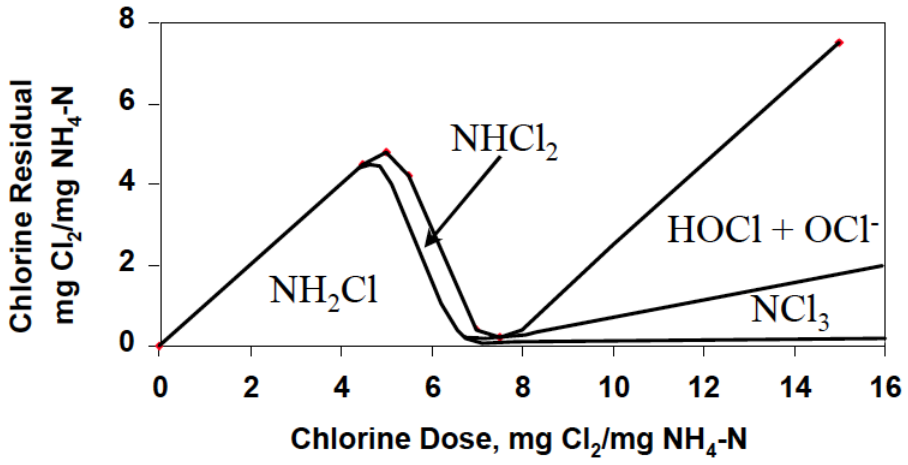

Figure 9: Relationship between the three chloramine forms as a function of Cl_2: NH_4-N ratio for pH range 6.5-8.5 (37)

It can be seen that up to the Cl_2:N ratio of 5:1, predominantly monochloramine is formed. As the ratio increases further up to 7.6:1, the breakpoint reaction occurs that reduces the concentration of residual chlorine to a minimum. Breakpoint chlorination results in the formation of nitrogen gas, nitrate and dichloramine. Above 7.6:1 ratio, free chlorine and trichloramine are present.

The biocidal potency of the three chloramines are in the order of $HOCl > OCl^- > NH_2Cl > NHCl_2 > NCl_3$. So it is preferable to have monochloramine formed as the main chloramine. This can be controlled by controlling the pH and Cl_2:NH_4-N ratio, if possible.

1.8 Fundamentals of Boron-doped Diamond (BDD)

Diamond is a form of carbon where each carbon atom is tetrahedrally bonded to four other carbon atoms by means of sp^3 hybridized bonds. Diamond possesses

properties such as extreme hardness, high electrical resistance, high thermal conductivity, high electron and hole mobility, and a wide band gap of 5.5 eV (38).

When doped with boron, diamond films possess semi-metal electrical properties. At higher doping levels, the electrochemical behavior of BDD films is almost metallic, exhibiting high kinetic reversibility (39). Energetically, the boron dopant atoms (electron acceptors) form a band located at 0.35 eV above the valence band edge (Figure 10 (40)) and at room temperature some valence band electrons get promoted to the impurity band, leaving holes in the valence band for current conduction. (38). This impurity band formation model has been reported elsewhere as well (41). Electrical conductivity is also affected by surface impurities and grain boundaries for polycrystalline films. However for single crystal films, the effect of doping on conductivity and reactivity is dominant (38). This electronic behavior has consequences on the electrochemical behavior of diamond as well. BDD films have a relatively large overpotential for oxygen and hydrogen evolution and low background currents (42-44).

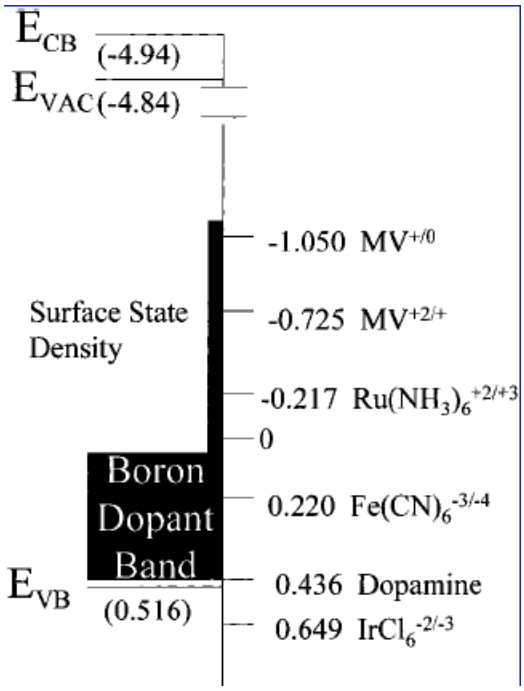

Figure 10: Energy band diagram of boron doped diamond film compared to standard reduction potentials of select redox couples (40)

Background current for diamond films is lower than that of glassy carbon. This could be due to low carbon-oxygen functionalities on the surface and lower density of surface electronic states causing a reduction in the counter-balancing ions in the solution (38).

The aforementioned properties make diamond a suitable anode for electrochemical oxidation of undesirable organic compounds. Table 2 summarizes such applications of BDD reported in the literature.

Table 2: Summary of applications of BDD electrodes for oxidation of various organic compounds as reported in literature

Reference	Year	Application
Troster *et al* (45)	2002	Chemical oxygen demand (COD) removal from industrial waste water
Chang *et al* (44)	2009	Cleaning of residual organics left on a liquid crystal display LCD device
Hagans *et al* (46)	2001	Oxidation of phenol
Sarada *et al* (47)	2000	Oxidation of Histamine and Serotonin
Rao *et al* (48)	1999	Oxidation of nicotinamide adenine dinucleotide (NADH)
Brillas *et al* (49)	2004	Oxidation of of chlorophenoxy herbicides
Gandini *et al* (50)	2000	Oxidation of carboxylic acids

2. A method to obtain a Ragone plot for evaluation of carbon nanotube supercapacitor electrodes

This chapter describes a technique that was developed to obtain the energy and power density for individual nanostructured electrodes, with the goal of constructing a Ragone plot (51). Existing techniques require a complete packaged device, which is time consuming to construct and does not enable measurement of a single electrode material. The technique reported here provides a way to assess and compare the performance of electrodes of a supercapacitor as a part of a conventional three terminal electrochemical cell. This allows comparison of different electrode materials and modifications thereof, such as surface engineering and geometric modifications. Electrode development will be critical to the realization of supercapacitors.

This technique has been adapted from a similar technique developed by the U.S. Department of Energy to standardize the evaluation of packaged commercially available supercapacitors for use in electric drivelines and for battery load-leveling (52). This method was adapted for the research environment where a typical setup uses a three terminal cell (53), which includes the electrode under study or the working electrode along with a reference and a counter electrode, which is designed to have no influence on the results. A packaged device typically does not have a reference electrode and the results are an integration of two working electrodes, making data interpretation much more difficult. This chapter covers the experimental setup, procedure and calculations to

obtain Ragone plots for individual electrodes. It also presents results for vertically aligned CNTs in various aqueous electrolytes.

2.1 Introduction

When comparing different energy storage systems, it is essential to use characterization methods that accommodate the differences in the mode of energy storage. Furthermore, for energy storage systems that are electrochemical in nature; such as batteries, fuel cells, and supercapacitors; electrochemical characterization techniques should facilitate matching the storage systems to their potential application areas (54). Ragone plots have been used historically to compare different battery technologies (51); however, with the emergence of supercapacitors, fuel cells, and advanced batteries, Ragone plots are being used to compare the performance of technologies that utilize different modes of energy storage(55). Moreover, Ragone plots can also be used to select an optimum working point (i.e., discharge rate) or the optimum size of an energy storage device (ESD) for a specific application (56). Energy and power densities are frequently given for a packaged device, rather than an electrode or a half cell (electrode, solvent, and electrolyte.) Materials research on new electrodes requires the ability to isolate the performance of individual components, such as the electrode or electrolyte, to understand the effects of changes to these components while avoiding the cost of developing a packaged device. The technique reported here provides a way to assess and compare the performance of components of a

supercapacitor as a part of conventional three-terminal electrochemical cells. The present work has focused on comparing electrodes, as the energy and power performance of different electrode materials and modifications thereof, such as surface engineering and geometric modifications (57). Such materials development will be critical to the realization of supercapacitors that can challenge the energy density of lithium-based batteries.

A Ragone plot is a log-log plot of a device's energy density versus its power density, as shown in Figure 11 (51). A curve on a Ragone plot for a given device represents the range of energy density and power density over which the device can be operated. This facilitates the selection of an optimal working region for a given energy storage system (See inset Figure 11 (51)). Positive unity slope lines on the Ragone plot indicate discharge times. Every point on a Ragone curve is associated with a characteristic discharge time given by the intersection of a unique positive unity slope line with the given point on the curve. For a typical Ragone curve, points with higher energy density have longer discharge times compared to those with higher power density. Additional discussion of the shape of Ragone curves can be found in the Results section.

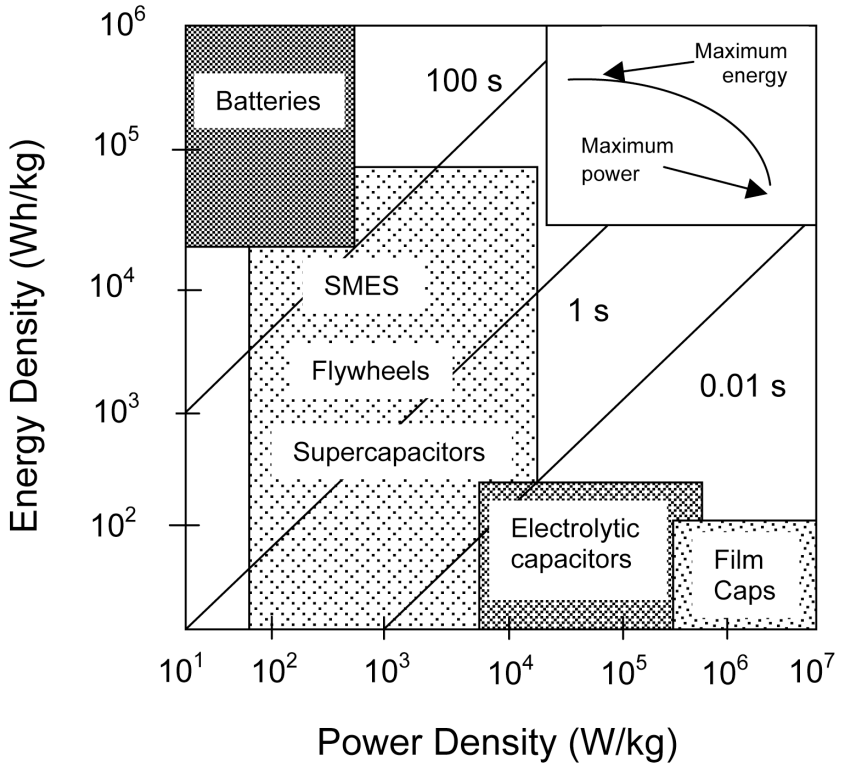

Figure 11: Ragone plot of standard energy storage devices on logarithmic scale on both axes (inset: characteristic Ragone curve with points of maximum energy and power indicated) (51)

Ragone plots can be used for all types of energy storage systems and are not dependent on the way in which is energy is stored, e.g., electrochemically for batteries and mechanically for flywheels. The technique described in this chapter to obtain Ragone plots of supercapacitors was adopted from a similar technique developed for the Department of Energy to standardize performance evaluation of packaged, commercial capacitors for use in electric drivelines and for battery load leveling (58). This method was adopted for the research environment, where a typical system uses a three terminal electrochemical cell to characterize a single electrode (the working electrode in a half

cell) without the similar opposing electrode found in a packaged supercapacitor. Instead, there is a counter electrode that does not affect the measurements, allowing determination of the working electrode characteristics. This technique uses a potentiostat operated in both galvanostatic and potentiostatic modes to obtain key electrochemical parameters of the half-cell to generate a Ragone plot.

2.2 Experimental Methods

2.2.1 Experimental Setup

The electrochemical cell (K0235 by Princeton Applied Research) was a three terminal cell, with a working electrode, counter electrode, and reference electrode (Figure 12 (59)). The working electrode was the carbon nanotube sample. The counter electrode was a platinum mesh. By varying the gasket area (the electrode area exposed to the electrode) and the area of the counter electrode, it was verified that the counter electrode was not a rate-determining factor in the double layer charge storage process. The reference electrode was saturated Ag/AgCl in saturated KCl (MF-2052 by Bioanalytical). The electrolyte was water with either 0.85-0.90 % w/v NaCl or 0.02 N sulfuric acid in solution. The nominal electrode area, as defined by a PTFE gasket, was 0.053 cm2. The reference electrode resided in a separate sub-section of the cell connected to the region near the double layer interface at the gasket opening by a Luggin-Haber capillary tube (Figure 12 (59)). The distance between the electrochemical double layer and the end of the capillary tube was at least twice the diameter of the tube to satisfy the

assumptions underlying a variety of the electrochemical equations used to quantify the cell performance (18). The potentiostat (Model 1287A by Solartron Analytical) had four terminals – WE (working electrode), CE (counter electrode), RE1 (reference electrode 1), and RE2 (reference electrode 2). WE and RE2 were connected to the working electrode of the cell. CE was connected to the counter electrode and RE1 was connected to the reference electrode.

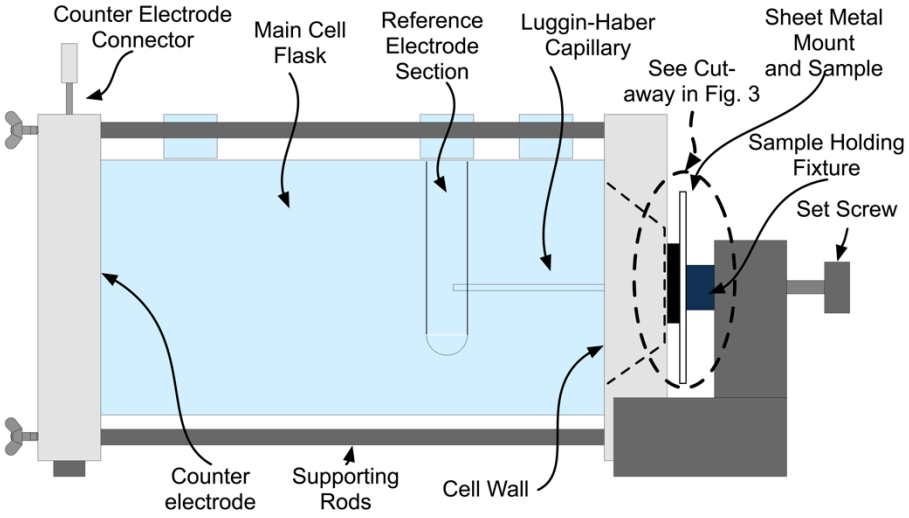

Figure 12: Schematic representation of a three terminal electrochemical cell (59)

2.2.2 Sample Preparation

MWCNT samples were grown in a 915 MHz MPECVD system. MWCNTs that were grown in this system were vertically aligned with a bamboo structure (Figure 13 (59)). The tubes were grown on an oxidized silicon substrate coated with a 5 nm Fe layer. The substrate rested on a heated fused quartz plate. Gas flow in the growth chamber was controlled by mass flow controllers. Prior to growth, the substrate was heated to

850 °C for 3 min. This transformed the smooth iron layer into discrete islands ranging from 20 to 50 nm in diameter as determined by scanning electron microscopy (SEM) (12). These sites formed the sites for MWCNT deposition during the growth phase.

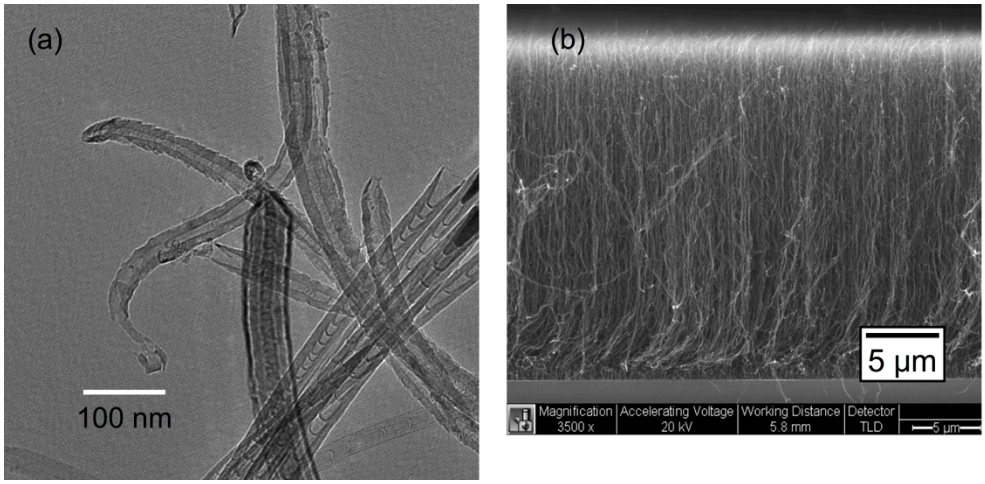

Figure 13: (a) TEM image of MWCNTs. (b) SEM image of vertically aligned MWCNTs (59)

The substrate size was typically 2 x 2 cm. The sample (along with its silicon substrate) was mounted on a glass slide or a piece of sheet metal using copper or carbon tape. An electrical contact was drawn out from the samples using silver epoxy paint. The sample was then pressed against the gasket with a holding fixture as shown in Figure 12 (59). The gasket formed a watertight seal with the sample surface and underlying silicon substrate. The electrolyte did not contact the metal sheet or the silver epoxy. Inspection of samples with SEM after electrochemical measurements confirmed that the electrolyte did not leak outside the exposed gasket area and wet other parts of the sample (see Figure 14 (59)). Additionally, when a size series of gaskets with

diameters from 2.38 to 9.53 mm were measured the extrapolated line of capacitance values vs gasket diameter crossed the origin within the error of the measurement (i.e., a gasket of zero diameter would have zero capacitance). Leaking electrolyte would cause a significant non-zero intercept on the capacitance axis.

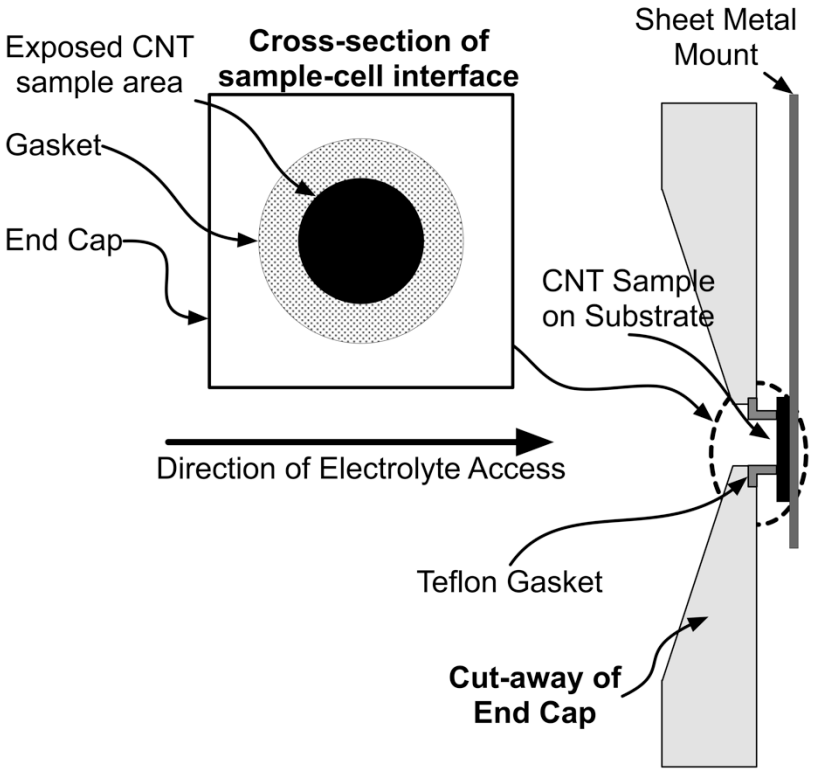

Figure 14: Cross-section of electrochemical cell end cap (cross-section line marked in Figure 12) showing the gasket and mounted MWCNT sample (59)

2.2.3 Electrochemical Measurement Procedure

A current versus time plot of three charge-discharge cycles is shown in Figure 15 (59). For each measurement, at least five different current values were measured for the galvanostatic regions of the experiments so that the discharge times varied from 2 to 100 s. The discharge time regime is between 2 s and 100 s, which is recommended for electric

drivelines and load leveling (58), a common application for supercapacitors. However, this technique can be easily used for higher or lower frequencies depending on the ultimate application of interest. It is expected that at higher frequencies, there are two factors that may serve to reduce the energy density of the system. The first is impedance, mainly inductance, from the test fixture. The second is a change in the ability of the electronic double layer to react. For our experimental setup, the resonant frequency is in the range of 800 Hz to 1 kHz. At this point and at higher frequencies (shorter charge-discharge times), the electronic double layer is not acting as a capacitor, but rather a short circuit. The ESR does not vary with frequency. The cell was charged with a positive constant current to the upper limit of the electrochemical voltage window. For aqueous solutions, the upper limit is 1 V, above which electrolysis of water occurs. For the purpose of characterization in this case, the upper limit was set at 0.7 V. For non-aqueous solutions, this upper limit can be higher than 1 V (2.5–3 V for acetonitrile) (60). The voltage was then held constant for 10 s in potentiostatic mode. This step allowed the double layer at the electrode interface to stabilize. After holding for 10 s in the potentiostatic mode, the cell was galvanostatically discharged by passing the negative of the charging current until the voltage reached either 0 V or a set lower limit of the voltage window. The lower limit was set close to the open circuit potential (OCP) of the uncharged cell, because if the cell was discharged to voltages much higher or lower, the

cell had a tendency to return to its uncharged OCP. The charge, hold, and discharge steps constituted one charge-discharge cycle (Figure 15 (59)).

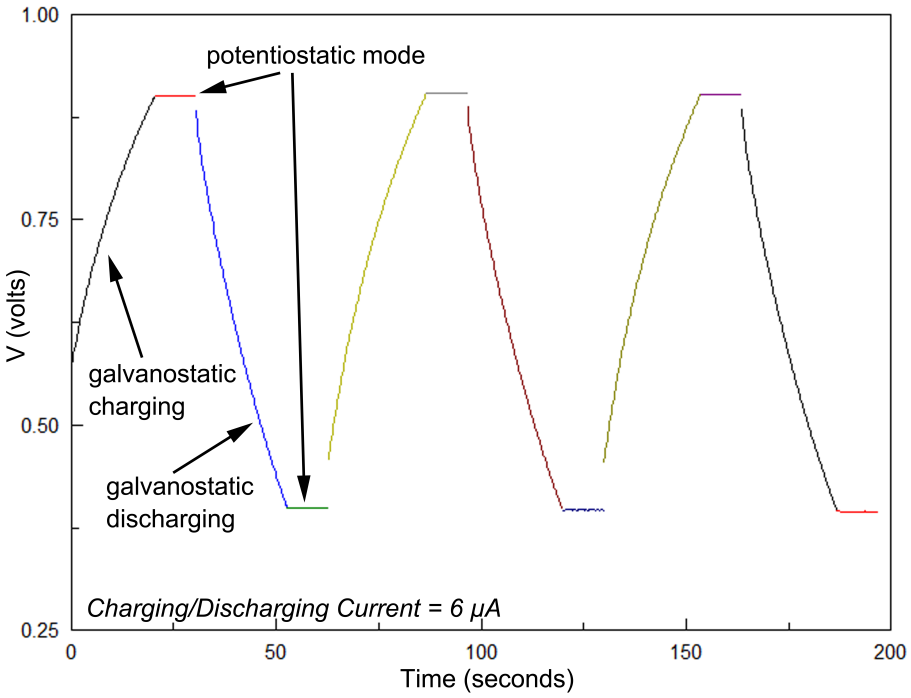

Figure 15: Galvanostatic and potentiostatic curves from three successive charge-discharge cycles (59).

For a given current value, three such cycles were recorded. The voltage and time values were averaged over the second and third cycles. The averaging helped minimize the effects of transients. Since the entire measurement was automated and each current cycle was performed immediately after the previous cycle, the first cycle was not included because during the first cycle, the electronics settle.

2.2.4 Data Measurement and Calculations

The following sections describe the parameters that were measured for both the second and third cycles for each current value (Figure 15 (59)).

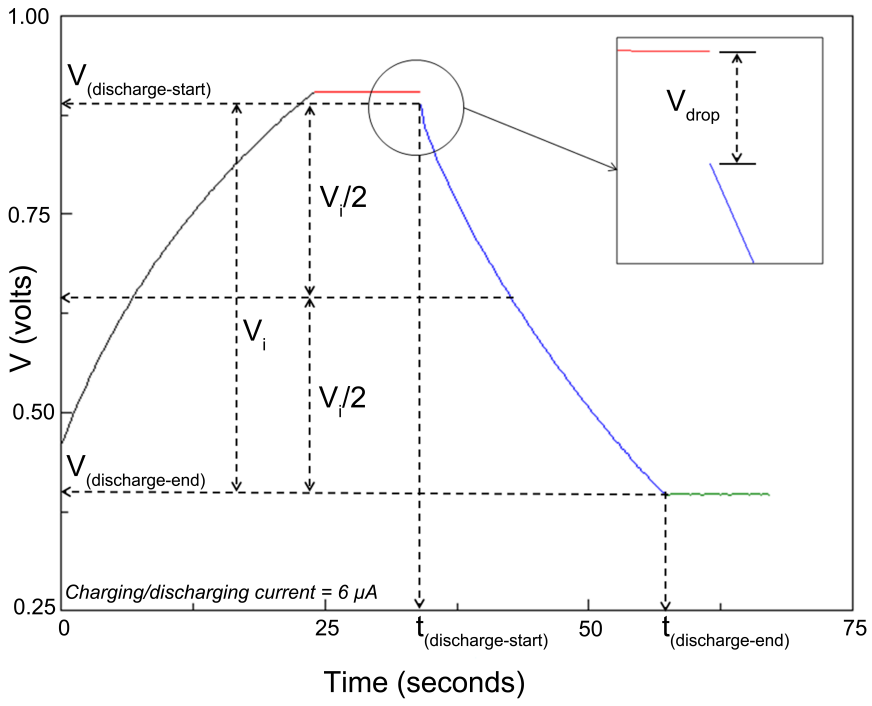

Figure 16: A single galvanostatic charge-discharge cycle showing various points for data measurement (59).

2.2.4.1 Total Capacitance

For each cycle, the total discharge time is measured, as well as the difference between the voltage at the beginning and the end of the discharge phase such that (see Figure 16 (59)):

$$t_{test}[s] = t_{(discharge-end)} - t_{(discharge-start)}$$
$$V_{test}[V] = V_{(discharge-start)} - V_{(discharge-end)} \quad \text{- 4}$$

where time t is in seconds and voltage V is in volts. The discharge time ends when the voltage reaches the lower limit of the voltage window. The capacitance C in farads is then calculated as the following:

$$C_{test}[F] = \frac{(I_{test}[A] \times t_{test})}{V_{test}} \quad \text{- 5}$$

where I_{test} is the constant current in amperes, applied in the galvanostatic cycles.

2.2.4.2 ESR (Equivalent Series Resistance)

The drop in voltage between the end of the first potentiostatic phase and the start of the galvanostatic discharge phase is Vdrop (see inset Figure 16 (59)). This drop is caused by the ESR of the cell. The ESR is the resistance of the entire device, including the electrodes, solution, and fixturing. For supercapacitors, the ESR dissipates energy, so a low value is more desirable. ESR is calculated as the following:

$$ESR[\Omega] = \frac{V_{test}}{I_{test}} \quad \text{- 6}$$

2.2.4.3 Energy Density (Energy Stored Per Unit Mass)

Energy density is in the industry-standard Wh/kg. This is determined from the following relation:

$$E\left[\frac{Wh}{kg}\right] = \frac{(0.75 \times I_{test} \times t_{test} \times V_{test})}{(3600 \times m[kg])} \quad \text{- 7}$$

where m is the total mass of the carbon nanotubes on the electrode in kilograms. This is estimated in the next section.

2.2.4.4 Power Density (Power Per Unit mass)

Power density is in the industry-standard W/kg. The power density is determined from the following equation:

$$P\left[\frac{W}{kg}\right] = \frac{(I_{test} \times V_{test})}{(2 \times m[kg])} \quad \text{- 8}$$

where V_{test} is equal to V_i measured in the discharge mode (Figure 16 (59)). It is the difference of the start and end voltages, as noted in Figure 16 (59). The factor 2 appears in the denominator because the energy and power densities are calculated at the condition of maximum power transfer. Maximum power is transferred when the capacitor discharges from Vi to Vi/2 (18). The energy and power density thus obtained for each constant current value is plotted on a log-log plot of energy density versus power density. This is a Ragone plot.

2.3 Estimation of Weight of MWCNT Samples

In order to calculate the energy and power densities, the weight of either the electrode material used or that of the entire package must be known. When comparing the gravimetric energy and power densities of two ESDs, it is important to make sure that the systems being compared have their weights calculated in the same way, that is,

weight of only the electrodes of the two systems or the weight of the full package of the systems. In the present case, the weight of only the working electrode, that is, the weight of the MWCNTs without the substrate, will be considered. Peigney et al. have calculated the theoretical external surface area of single- and multi-walled CNTs (61). Their work has been extended here to obtain the weight of CNTs with an arbitrary number of walls and ultimately the weight of a CNT film. The weights will be used to obtain the energy density and power density. It is calculated based on the atomic structure of graphene as CNTs are tubular structures formed from graphene (5). The following assumptions are made for the calculation.

2.3.1 Assumptions

i. The sp^2 hybridized C-C bond length in a hexagonal cell of graphene is 0.142 nm (Figure 17 (59)).

ii. MWCNTs can be approximated as concentric cylinders with a variable number of walls.

iii. The graphene inter-shell distance is 0.335 nm. The inter-shell distance is the distance between adjacent graphene planes.

iv. The sp^2 hybridized C-C bond length in the graphene layer remains unchanged even when the layer is curved.

v. The area of the tips of the tubes is negligible.

vi. MWCNTs with r ¼ 25 nm, h ¼ 15 mm, and 35 concentric cylinders are considered. The number of inner walls was obtained by measuring the wall thickness of MWCNTs from transmission electron microscopy (TEM) images (62), and calculating the number of walls using the inter-wall spacing for MWCNTs. These MWCNTs were grown in the same deposition system as the samples analyzed for the Ragone plot (62).

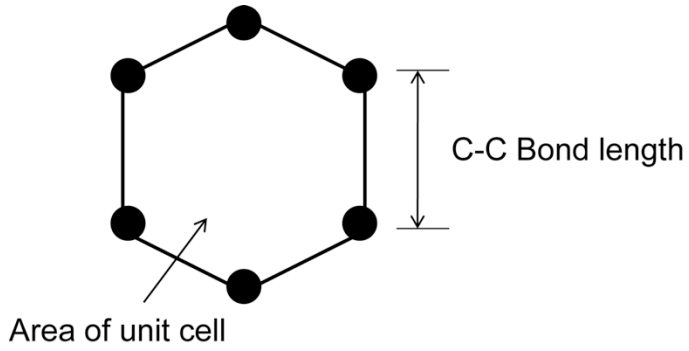

Figure 17: Schematic representation of a hexagonal unit cell of graphene (59).

2.3.2 Calculations

i. The area of a single hexagonal graphene unit cell (Figure 17 (59)) is 5.238×10^{20} m^2.

ii. The curved surface area of the outermost wall 3.00×10^{-12} m^2 while that for the innermost is 2.04×10^{-12} m^2.

iii. The surface area of each tube in a single MWCNT is divided by the hexagonal area of a single graphene unit cell to obtain the total number of carbon atoms in each wall or concentric cylinder (there are 2 C atoms to each hexagonal unit after taking into consideration the sharing of atoms among units). From the total

number of carbon atoms and the atomic weight of a carbon atom, the weight of each tube is calculated as 6.72 x 10^{-17} kg.

iv. From the SEM image (Figure 18 (59)) of nucleated islands of catalyst during growth of MWCNTs in a MPECVD system, it is seen that there are an average of 9 potential growth sites on a substrate area on 250 mm x 250 mm. Thus, the average tube density is 1.5 x 10^{10} MWCNTs/cm^2.

v. The gasket used in the electrochemical cell that defines the exposed MWCNT area has a diameter of 2.62 mm. Thus, the area of the gasket is 0.053 cm^2.

vi. The total number of tubes exposed to the electrolyte is then calculated as 7.95 x 10^8.

vii. From the weight of one tube, the total weight of the MWCNT electrode material is calculated as 53.4 μg.

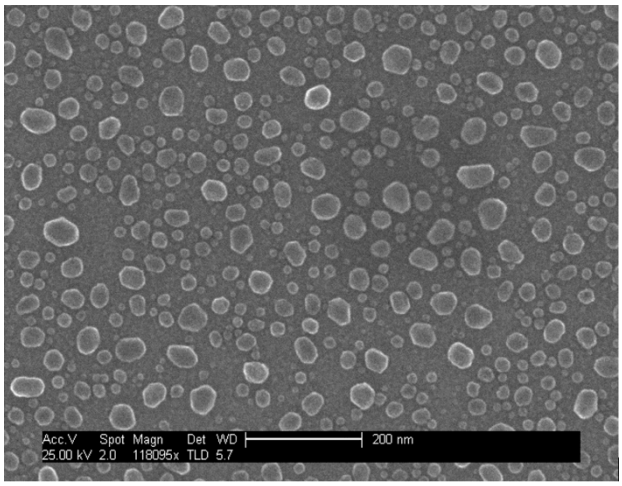

Figure 18: TEM image of nucleation of metal nanoparticles prior to MWCNT deposition (59).

2.3.3 Weight Determination by Scaling of Direct Measurement

The weight of the MWCNTs was also measured directly by means of a precision balance (Mettler Toledo Model AB54-S/FACT). After subtracting the weight of the substrate, the weight of the MWCNTs was 0.01641 g over 9.03 cm^2. The height of the MWCNTs was sampled at 32 locations across the sample to obtain an average. This was determined to be 21.1 μm. The MWCNT density on the substrate is a function of the size and spacing of the catalyst islands upon which the MWCNTs nucleate. Thus, the weight scales linearly with the height of the tubes. Using the weight per cm^2 of the electrode and per mm height for the MWCNTs, the weight of the MWCNTs for the samples used to construct the Ragone plots was determined. The weight of the MWCNTs described in Assumption 6 above, namely the 15 μm height, is determined to be 68.8 μg.

2.3.4 Comparison of the Calculated and Scaled Weight

The 15.4 mg difference between the calculated and the scaled weight is reasonable given the fundamental starting point of the theoretical calculation. The difference is the equivalent of eight walls in the MWCNT diameter. That is, the calculation used the wall thickness as measured by TEM and the expected adjacent wall spacing to give 35 walls. MWCNTs having a weight equal to the scaled measurement would have 43 walls. The extra weight is likely due to the internal bamboo structure in the MWCNTs or small amounts of amorphous carbon present in the film, neither of which was accounted for in the calculation.

2.4 Process Validation

In order to establish the validity of the technique, a commercial supercapacitor (Cap-XX HS106) was tested using both electrochemical impedance spectroscopy (EIS) and galvanostatic tests. The total capacitance was determined by both methods. The Cap-XX capacitor was not tested in the electrochemical cell, but rather using a two-terminal measurement. For this measurement, RE1 and CE were connected to one terminal and RE2 and WE were connected to the other. As the goal of the Cap-XX measurements was to confirm the validity of the EIS and galvanostatic approach, the energy density and power density were not calculated. The results are summarized in Table 3 (59). The value of the total capacitance obtained from the galvanostatic test technique was 1.18 F. Comparison with the manufacturer rated value (1.10 F) gave our measurement an accuracy of 1/10 F (9.09%).

Table 3: Capacitance values of Cap-XX capacitor measured using electrochemical impedance spectroscopy and a galvanostatic approach (59).

Sample	Rated value (F)	Value from electrochemical impedance spectroscopy (F)	Value from galvanostatic measurement (F)
Cap-XX HS106	1.10	1.02	1.18

2.5 Results

The results of the galvanostatic tests for four MWCNT samples are summarized in Figure 19 (59) and Table 4 (59). The Ragone plot for the MWCNT samples is shown in Figure 19 (59). Table 4 (59) summarizes specific capacitance, ESR, and length of the

MWCNT samples. The electrolyte used was saline (details above) unless otherwise indicated. The sample name specifies the run number of the MPECVD system. The samples were grown for 120 s (for NAM465 A and NAM465) or 180 s (NAM509 and NAM511) and thus heights are 15 and 25 μm, respectively, for each group. The first sample, NAM465 A, was measured with 0.02 N sulfuric acid solution as the electrolyte. The specific capacitance values observed in Table 4 (59) are somewhat lower than the literature values for similar nanotubes (19), using the scaled weight. The values for energy and power density are also lower than those in literature. However, variations in the way that the weight and what is included in the weight make direct comparisons difficult. The galvanostatic charge-discharge method used to obtain these parameters is validated by the measurements made on the commercial supercapacitor, as the comparison of the total capacitance determined by both the galvanostatic method EIS agreed with the rated value from the manufacturer. The higher energy density for the sample tested with 0.02 N sulfuric acid electrolyte (instead of saline) confirms that acid solutions result in higher capacitance and energy density, either by chemical modification of the MWCNTs or a higher ionic concentration. The energy and power density using the scaled weight are illustrated on a Ragone plot in Figure 19 (59). The shape of the curves obtained is typical of energy storage systems. The energy densities drop at higher discharge rates (and thus high power) due to an increase in internal losses (51). The effect of ESR on the shape of the Ragone curve is to steepen it as the ESR

increases. Hence NAM465A has a higher ESR and exhibits a sharper drop in energy density at high power than NAM511, which has a lower ESR. The energy and power density of the particular samples reported here are relatively low compared to commercial supercapacitors due to the high ESR associated with the volume of the electrolyte and contact resistance in these experiments. Recent measurements to be reported in another publication indicate that these parameters can be optimized, enabling competitive energy and power densities.

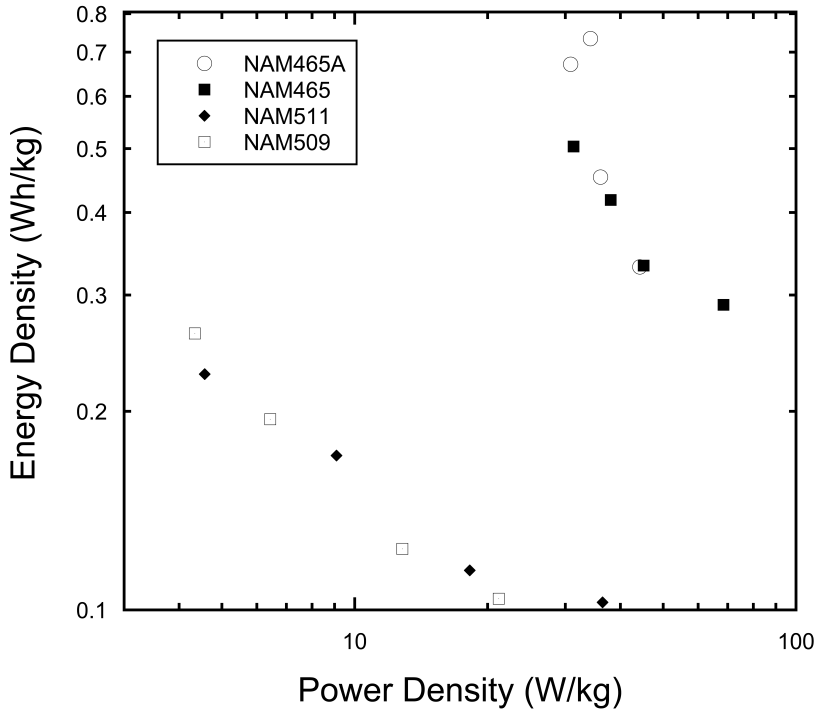

Figure 19: Ragone plot of MWCNT samples using logarithmic scale on both axes (energy and power densities calculated using direct scaled weight measurement of MWCNTs) (59).

Table 4: Specific capacitance, ESR, and length of MWCNT samples shown in Figure 19 (59).

Sample	Specific Capacitance (F/g)	ESR (Ω)	Length of MWCNTs (μm)
NAM465A	14.9	418.5	15
NAM465	15.33	865.76	15
NAM509	10.42	249.08	25
NAM511	10.28	102.99	25

2.6 Conclusions

A galvanostatic charge-discharge method has been developed for a three terminal electrochemical cell to obtain specific capacitance, ESR, and a Ragone plot. Specific energy and power for an electrochemical double layer cell with a vertically aligned MWCNT electrode were obtained and compared to reported values. The weight of the MWCNTs was estimated using a theoretical calculation that was verified with a direct weight measurement. Ragone plots for the MWCNT samples were obtained and compared by plotting on a single plot. The total capacitance of a commercial supercapacitor was measured by this technique and was compared to both the capacitance of that device measured by EIS and the value reported by the manufacturer. The capacitance values agreed to within 0.1 F (9.09%). Other galvanostatic techniques have been used to characterize electrochemical systems, but they have focused on calculating specific capacitance and coulombic efficiency and not obtaining energy or power density and thus not on construction of Ragone plots (63-66). The galvanostatic charge-discharge method facilitates energy and power performance comparison of

different electrode designs for the same electrolyte and cell. It is a powerful technique for those working on engineering electrodes for supercapacitors.

3. Effect of porosity variation on the electrochemical behavior of vertically aligned multi-walled carbon nanotubes

Electrochemical performance, including the capacitance, power density and energy density described in the previous chapter, is influenced by numerous parameters such as the electrolyte, the specific surface area, and the electrode morphology. In this chapter, we examine the effect of morphological variation of vertically aligned CNTs on electrochemical behavior, particularly capacitance. Varying the pretreatment time during the growth of CNTs in the MPECVD system varied the CNT diameter and inter-CNT spacing. It is speculated that increasing the pretreatment time during growth causes a reduction in the dewetted catalyst nanoparticle size and the spacing between the nanoparticles. The electrochemical capacitance of these samples was measured in a three terminal cell in non-aqueous electrolytes. It was found that the specific capacitance increased as the CNT diameter and inter-CNT spacing decreased (see Figure 20 (67)). This trend was compared to the capacitance versus pore size relationships reported in literature. A broad trend between capacitance and pore-size is proposed, based on the combination of results and literatures values. The trend spans a wide range, from macroporous to sub-nanometer pores.

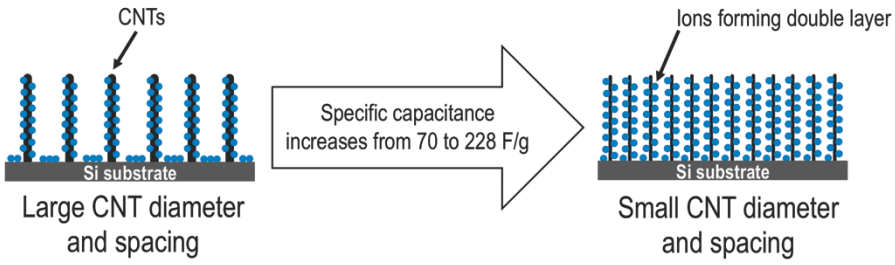

Figure 20: Illustration of increase in specific capacitance with decrease in CNT-diameter and inter-CNT spacing (67)

3.1 Introduction

Carbon Nanotubes (CNTs) are interesting as electrode materials in electrochemical double layer capacitors (ELDCs) (14) because of their nanostructured morphology, regular porosity, and electrical properties. They are also important in electroanalysis (68-70) for these same properties. Specific capacitance of electrodes depends on surface functionalities, surface area, and pore size distribution (71, 72). The relationship between specific capacitance and pore size has been studied extensively for materials with pore size distribution under 100 nm (72-75). For example, Ref. (76) reports the effect of mean pore size on specific capacitance in the sub-10 nm regime. It has been proposed that constriction of the compact ion layer within a sub-1 nm pore increased the capacitance significantly due to distortion of the ion solvation shell (77). Furthermore, specific capacitance increases with increasing surface area to a point (78). To the authors' knowledge, investigation of this relationship has not been extended to materials with pore size greater than 100 nm and a high aspect ratio, such as vertically aligned CNTs.

This work reports on the change in specific capacitance as pore size varies from 230 to 506 nm for vertically MWCNTs and discusses the broader transition from surface area- to pore size-dominated effects.

3.2 Experimental

3.2.1 CNT Film Growth

MWCNTs were grown using a 915 MHz Microwave Plasma Enhanced Chemical Vapor Deposition System. Fe-coated silicon substrates were heated to 850 °C in 150 sccm of NH3 in the MPECVD system, followed by striking and stabilizing a plasma at 21 Torr and 2.1 kW of magnetron input power. Substrates were then pretreated for pretreatment times of 5, 180, 1200, and 2400 s in the plasma to obtain samples with a range of porosity and surface area by varying the tube diameter and spacing. Following pretreatment, growth of the MWCNTs was accomplished by changing the gas flow to 150 sccm CH4 and 50 sccm NH3 for 120 s. The growth conditions were the same for all samples. The CNTs grown using this process are typically vertically aligned and multi-walled (79).

3.2.2 Experimental Setup

The electrochemical setup, sample preparation, and measurement protocol have been discussed in detail in a previous publication (59). Briefly, a three terminal electrochemical cell with working, counter, and reference electrodes (K0235 by Princeton Applied Research) was used. The working electrode was the MWCNT film, the counter electrode was a platinum mesh (3 cm×2.5 cm), and the reference was an Ag wire in 1 M

tetrabutylammonium perchlorate (TBAP) and 0.01 M silver nitrate (AgNO3) in acetonitrile (reference electrode-RE-7 and its solution supplied by BioLogic). The reference electrode resided in a separate subsection of the cell connected to the region near the double layer interface of the working electrode by a Luggin-Haber capillary tube. The distance between the interface and the tube was at least twice the diameter of the tube. The electrolyte used was 1 M lithium perchlorate ($LiClO_4$) in acetonitrile. The potentiostat was a SP-300 (Bio-Logic). All chemicals were used as received.

3.2.3 Sample Preparation

The sample was mounted on a piece of sheet metal using copper tape. An electrical contact was made painting conductive silver epoxy on the MWCNT side. The nominal active area of the electrode was defined by a PTFE gasket.

3.2.4 Electrochemical Testing Purpose

Cyclic voltammetry (CV) was performed on all the samples at a scan rate of 15 mV/s between 0 and 1.1 V vs Ag/Ag+ ion to obtain specific capacitance and detect the presence of Faradaic activity, if any. A three-terminal galvanostatic charge–discharge technique was also used to obtain charge–discharge curves at a current density of 5.7 A/g and a voltage window of −0.1 to 1.2 V. The galvanostatic technique was explained in detail previously (59).

3.2.5 Morphological Measurements

The vertical alignment and multi-walled nature of the CNTs were verified by SEM and TEM. The diameter and spacing of the MWCNTs were measured from high-resolution SEM images using ImageJ software (80). These images were thresholded to detect edges and then measurements were obtained at different points on each sample with a total of 22 measurements each for diameter and inter-MWCNT spacing. A similar approach to measure porosity has been reported previously (76).

3.3 Results and Discussion

Figure 21 (67) shows CV scans of all four samples. The charge storage capacity, represented by the area under the CV curve, increases substantially with reduction in inter-MWCNT spacing (i.e. pore size). No other significant electrochemical activity is apparent in the CV scans, indicating that most of the charge storage capacity comes from non-Faradaic double layer charging.

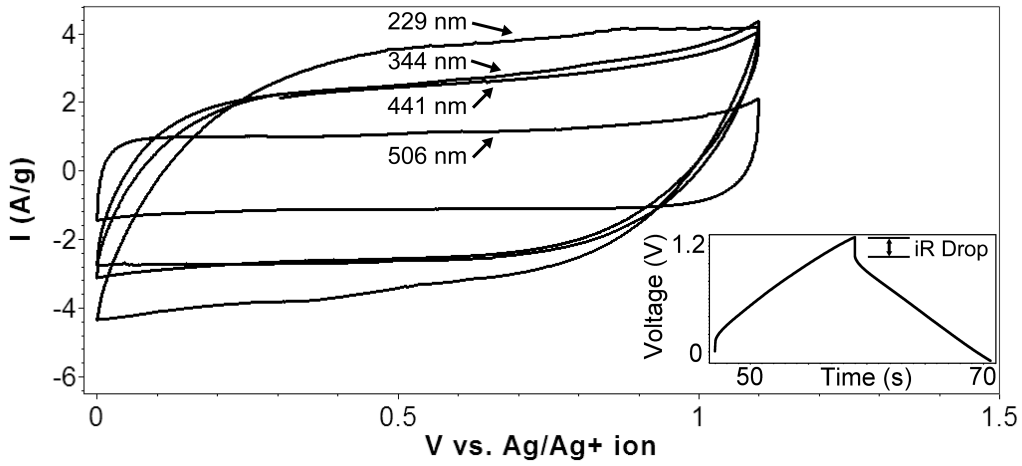

Figure 21: CV scans for MWCNT samples with varying morphology. The numbers on the curves indicate MWCNT pore size. Inset: Galvanostatic charge–discharge curve at a constant current density of 5.7 A/g for sample with inter-MWCNT spacing of 506 nm (67).

Figure 21 (67) inset shows a typical constant current charge discharge curve for the sample with inter-MWCNT spacing of 506 nm at 5.7 A/g. Symmetric and linear anodic and cathodic halves can be seen, consistent with capacitive behavior. Note that following convention (for example, see (81, 82)), the term IR drop has been utilized in this inset to signify equivalent series resistance, although interfacial potential changes would also play a role on these time scales. Such capacitive charge–discharge behavior was observed for all samples. The specific capacitance was calculated for the four MWCNT samples from CV measurements.

Figure 22 (67) shows specific capacitance measured from the CV curves as a function of MWCNT diameter and spacing. For vertically aligned MWCNTs, the inter-CNT spacing is the effective porosity. Specific capacitance increased significantly as

MWCNT diameter and spacing decreased. The same trend and comparable values for specific capacitance were observed for the galvanostatic method and CV scans. The maximum capacitance (228 F/g) was obtained for the sample with the smallest diameter/spacing combination. A contributing factor to the relatively high specific capacitance is the regular pore distribution of aligned CNTs (83). Specific surface area was calculated assuming the nanotubes to be an array of simple cylinders using a method similar to that of Ref. (84). The specific interfacial capacitance obtained in this manner was in the range of 1.6 mF/cm^2 to 3.3 mF/cm^2 with an average value of 2 mF/cm^2. Figure 22 (67) insets show that area specific capacitance remains constant with change in diameter and spacing. This shows that the increase in gravimetric capacitance with reduction in diameter and spacing is largely due to increase in surface area.

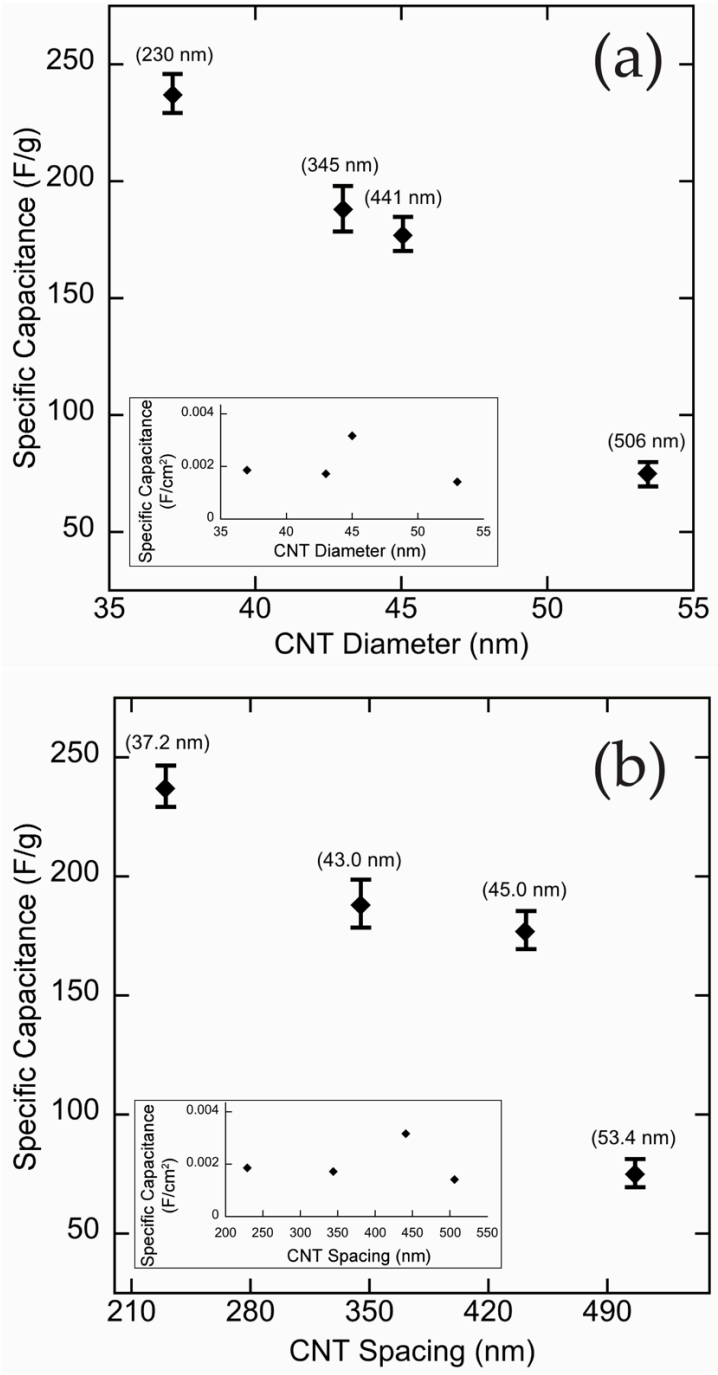

Figure 22: Variation in specific capacitance with varying (a) diameter and (b) inter-CNT spacing. 1σ error bars indicate variation in weight measurement. Numbers in parentheses are the corresponding spacing and diameter values in parts (a) and (b), respectively. Inset: Variation in area specific capacitance as a function of (a) diameter and (b) spacing (67).

Both the spacing and diameter of the CNTs have an influence on the electrochemical properties but the data suggests that diameter may have a greater impact on capacitance. For example, the 345 nm and 441 nm samples have diameters that are very similar and hence the capacitance values are also similar, despite the different spacings. Inter- CNT spacing and diameter were varied simultaneously in the present work and their effects on measured capacitance cannot readily be separated. A numerical analysis of CNT curvature effects on the diffuse double layer has been performed (85) and can be used to deconvolve the effects of diameter and spacing on capacitance. However, that approach is only applicable to nanotubes with radii less than 20 nm and in low supporting electrolyte concentration. Thus, it could not be utilized in the present study because only the sample with the smallest radius meets this criterion and the supporting electrolyte concentration is high. Three explanations were considered for the observed trend and overall improvement in electrochemical performance among these four samples:

1) more defect states (higher surface charge density may result from higher density of electrochemically active defects (86, 87))
2) better ionic access (more CNT film permeation by ions), and
3) higher specific surface area (smaller pores will result in higher effective surface area).

Raman spectroscopy was performed on the samples and there was no significant variation in peak height for the ID/IG ratio. This suggested that the increase in specific

capacitance was not due to a change in defect state density. It was previously observed that the MWCNTs used in this study were relatively more aligned near the base than the tip (88). However, this morphological characteristic was common to all the samples, hence improved ionic access due to pore distribution did not appear to be the dominant factor in the observed trends. These observations supported the explanation that improved capacitance was primarily attributed to an increase in specific surface area by optimizing porosity. Thus, there is potential to further improve the pore structure of vertically aligned CNTs based on tube geometry (diameter, spacing, alignment, etc.). The aspect ratio is higher than is observed in other carbon materials of similar porosity. This large aspect ratio of the pores may be contributing to the high specific capacitance.

Most CNT electrodes are made from non-aligned CNTs where pore size is neither easily controlled nor periodic. To the authors' knowledge, this work is the first to present a trend in specific capacitance for the pore size range of 230 to 506 nm for vertically aligned CNTs. The trend in specific capacitance is a function of the spacing and diameter. Smaller spacing and diameter lead to higher specific surface area and consequently higher specific capacitance. Combining these observations with previous reports reveals a qualitative trend between specific capacitance and pore size spanning the porosity regimes for porous carbon materials, shown in Figure 23 (67).

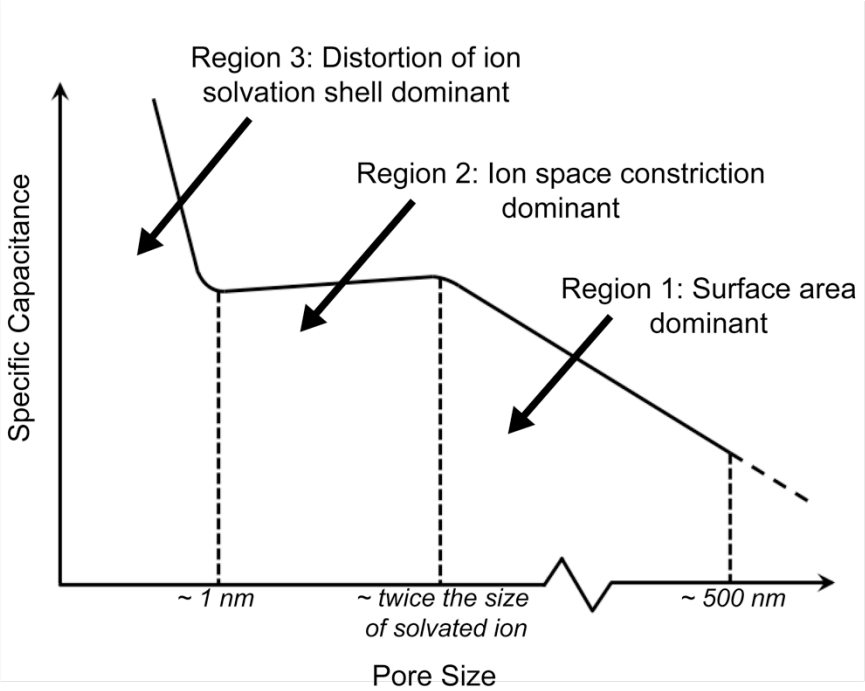

Figure 23: Qualitative trend of specific capacitance versus pore size (67).

The trend can be divided into three regions. In Region 1, specific capacitance is dominated by the electrochemically active surface area, increasing linearly with decreasing pore size. Region 2 begins when the pore size decreases to about 2× the size of the solvated ions. Space constriction effects hinder ion diffusion and cause the slope of the capacitance–pore size relationship to change, resulting in either a local maximum or saturation of specific capacitance as a function of pore size between regions 1 and 2 (74, 78, 89, 90). In Region 3 (b1 nm pore sizes), there is an increase in specific capacitance due to distortion of the solvation shell of the ions (77). This anomalous increase in specific capacitance in the sub-1 nm regime has been explained by using first-principles density functional theory (DFT) calculations (91). This qualitative trend line links the

three regions to provide a continuous description of the effect of pore size on the electrochemical behavior of double layer electrodes and how various phenomena become dominant in different pore size regimes. This understanding will aid engineering materials with hierarchical porosity for electrochemical capacitor applications.

Future work will investigate CNT geometries that extend Region 1 to smaller pore sizes that approach the local maximum and transition between Regions 1 and 2. Additionally, other electrochemical techniques will be used to obtain a deeper understanding of the role of porosity on vertically aligned CNTs.

3.4 Conclusions

Pore size of vertically aligned multi-walled CNTs was varied and the corresponding electrochemical behavior was studied. It was found that specific capacitance increased from 70 to 228 F/g as pore size decreased from 506 to 230 nm. This significant increase was attributed primarily to an increase in specific surface area via a reduction in pore size. Furthermore, a qualitative trend is proposed illustrating the variation in specific capacitance of porous carbon materials as a function of pore size.

4. Growth and Electrochemical Behavior of Graphenated Carbon Nanotubes

This chapter extends our understanding of morphological effects on electrochemical capacitance by examining the effects of carbon edges.. A novel carbon nanostructure composed of graphene-like foliates on vertically aligned CNTs called as graphenated CNTs (g-CNT) was synthesized. The effect of variation in foliate density of g-CNTs on capacitance is investigated. Since g-CNTs are grown in the same MPECVD system as regular CNTs, a design of experiments (DOE) study was planned to understand the range of structures and the degree of morphological control possible within the growth parameter space. Carbon nanostructures of varying morphology and defects were obtained. The effects of morphological defects prevalent amongst these structures on their capacitance are explored.

Randin and Yeger first reported the difference in capacitance between between capacitance densities at edges and basal planes in carbon nanostructures (92). Subsequent studies have confirmed the relative contributions of edges and basal planes of various carbon nanostructures (93, 94) and the even the electrochemical behavior of monolayer and bilayer graphene edges (95). Morphologically, g-CNTs are a combination of carbon basal plane and edges. The contribution of edges (in form of foliate density) on capacitance was studied by employing EIS.

Other carbon nanostructures that were synthesized as a part of the DOE, were characterized and their capacitance was correlated to their morphological properties.

This can lead to the development of carbon electrodes that can be engineered for specific applications. For that to happen, it is crucial to understand the effect of morphological characteristics on specific capacitance and catalytic activity.

4.1 Three-dimensional arrays of graphenated carbon nanotubes

4.1.1 Introduction

The fundamental advantage of a combined CNT-foliate structure is the high surface area framework of the CNTs coupled with the high edge density of the graphene sheets. Graphene edges provide high charge density and reactivity, but they are difficult to arrange in a three dimensional (3D), high-density geometry. CNTs are readily aligned in a high-density geometry (i.e., a vertically aligned forest) but lack high charge density surfaces—the sidewalls of the CNTs are similar to the basal plane of graphene. For example, the capacitance expected for the edge planes of graphene versus the basal plane is 3 versus 50 to 70 $\mu F/cm^2$. (92) Combining these properties by growing protrusions or graphitic foliates from CNT sidewalls can provide a unique and valuable 3D nanoarray of graphene edges. Since the thickness of the foliate structures can vary from 10 to 20 layers in the present study, we will refer to these hybrid structures more generally as "graphenated CNTs" (g-CNTs) and the foliate structures as "graphitic foliates" or just "foliates". They can be considered a foliated CNT because they are reminiscent of a striated, leaf-like structure growing from a CNT stem or a foliated column in gothic architecture.

Many applications require high charge density materials at the nano- or microscale, such as electrical conductors for nanoscale solid state devices, and therefore would benefit from high charge densities at edges. Examples of applications that could benefit from the combined structure include (i) an electrochemical double layer capacitor or "supercapacitor," (59) (ii) a neural stimulation electrode, (96) and (iii) a field emission electron source (97). These g-CNT structures may also be advantageous in CNT–polymer composites (98, 99), providing protrusions to enable mechanical interlocking between the CNTs and the matrix as well as reactive sites along the length of the CNT for chemical binding to the polymer matrix. One of the problems reported for composites that use CNTs as the reinforcing phase is stress transfer from the matrix to the CNT. The edge structure of graphitic foliates can enable a controllable level of chemical interaction with the matrix and the flat surfaces of the foliates, forming an interlocking structure that mechanically transfers the load.

Kurt et al. (98, 100, 101) have grown "decorated C:N Nanotubes" using hot filament growth of surface decorations on CNTs, resulting in structures with some similarities to those presented here. The structures were described as "disordered multi-walled nano-tubes" that were "probably hollow" and the graphitic decorations were described as "lamellar needle-like structure with a preferential radial growth direction (perpendicular to the tube axis)." (100) Mata et al. (102) have also reported what appear to be graphitic nanosheets integrated with CNTs in the context of a study on the

nucleation of carbon nanostructures on nickel foil. Although there is little discussion on the details of the structure, Mata et al. identified the core structures as carbon nanofibers rather than CNTs.

The present research reports the growth and characterization of g-CNTs—a nanostructure that has the potential to integrate the exceptional properties of graphene or graphitic nanosheets with those of CNTs by growing the nanosheets or foliates protruding from the sidewalls of the CNTs. A proposed mechanism for foliate formation during CNT growth is also presented.

4.1.2 Experimental

g-CNTs were grown using a 915 MHz MPECVD system. To prepare the substrates, 5-nm iron films were deposited on Silicon (100) wafers using a CHA electron-beam evaporation system. Prior to growth, the coated substrates were heated to 1050 °C in 150 sccm of NH3, followed by striking and stabilizing a plasma at 21 Torr and 2.1 kW of magnetron input power. The pressure of 21 Torr was maintained throughout the pretreatment and growth steps. Substrates were then pretreated for 180 s in the plasma. Following pretreatment, growth of the g-CNTs was accomplished by changing the gas flow to 150 sccm CH4 and 50 sccm NH3 for 360 s. Details of the deposition system can be found in Cui et al (79).

SEM images of these nanostructures can be seen in Figure 24 (103). Through adjustments in growth conditions, the density of the graphitic features can vary from

none (i.e., only CNTs grow), low density [Figure 24(a)], medium density [Figure 24(b)], to high density [Figure 24(c)]. Increasing density is accomplished by a combination of higher growth temperature, higher methane to ammonia ratio, and/or longer growth time, as described in more detail later. Raman spectroscopy was performed with a Horiba Jobin Yvon LabRam ARAMIS system (Horiba, Kyoto, Japan) that was calibrated using a silicon standard before use. SEM was performed using a FEI XL30 SEM-FEG (FEI, Hillsboro, OR) and TEM was performed with a FEI Tecnai G2 Twin with an accelerating voltage of 200 kV.

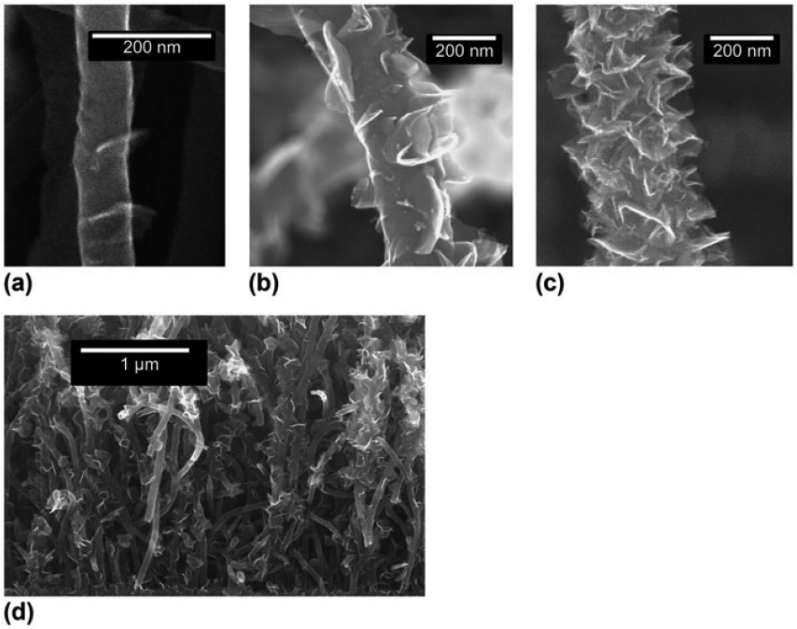

Figure 24: SEM images of g-CNTs. (a) Low-density graphene foliates on a CNT. (b) Medium-density graphene foliates on a CNT. (c) High-density graphene foliates on a CNT. Structures were reproducible and observed over several square centimeters after microwave plasma chemical vapor deposition growth. (d) Cross-sectional SEM image showing a typical aligned g-CNT film (103).

4.1.3 Results and Discussion

g-CNTs consist of perpendicularly oriented foliates growing out from the sidewalls of multiwall CNTs. Figure 24(a)–1(c) (103) show three different densities of foliates. Figure 24(d) (103) depicts an SEM cross section of a typical film of semialigned CNTs with foliates along their length. The density of foliates can be controlled by varying the growth conditions. In Figure 24(a)–Figure 24(c) (103), the foliate density per micron of CNT length increases from 4.2 to 5.3 to >15.0, respectively.

TEM images of the g-CNTs (Figure 25 (103)) provide additional insight into the nucleation and growth of the foliated structures. The hollow core, characteristic of CNTs (104), is clearly observed in Figure 25(a) (103). The CNT sidewalls, however, are unusually thick relative to the diameter, a consistent characteristic for the g-CNTs observed in this work. What appears to be secondary nucleation is also observed in Figure 25(b) (103); smaller foliates protruding from the primary "leaf" itself growing normal to the CNT sidewall. The specific mechanism for secondary nucleation is currently unknown and will be the topic of future studies but defects at the active growth surface of the foliate are expected to play a role (105). The majority of the foliates grow with a curvature vector that is coplanar with the axis of CNT growth, i.e., the curvature being either concave up or concave down, suggesting that the fiber texture of the foliate may have nucleated from the original fiber texture of a fractured CNT.

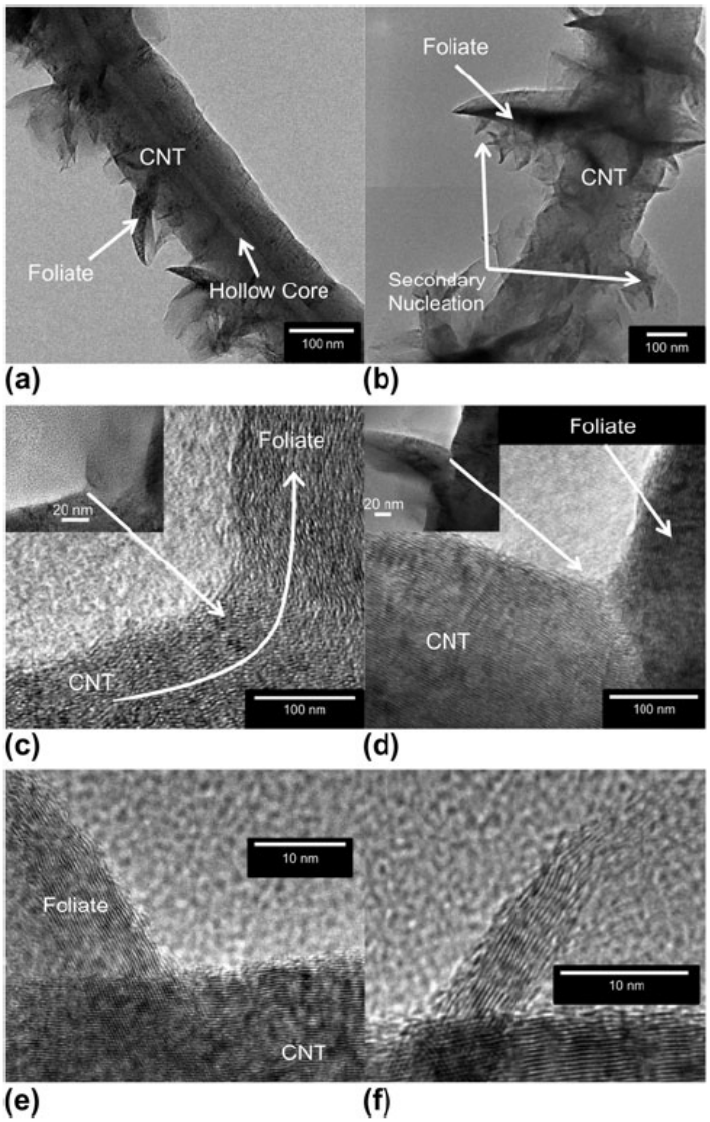

Figure 25: Transmission electron microscopy images of g-CNTs. (a) The hollow core of the nanotube shows graphene foliates in CNTs, rather than nanofibers (b) Secondary nucleation of graphene foliates is indicated by arrows. The presence of secondary nucleation indicates an active growth surface on the graphene foliates. (c) Coherent interface between CNT sidewall and graphene foliates. Inset: lower magnification image of same. (d) Incoherent interface between nanotube sidewall and the graphene foliates. Inset: lower magnification image of same. (e) Lattice fringes from CNT stem and graphene foliate are visible. The average of 11 fringes for the CNT and leaf gives values of 0.362 nm in the foliate and 0.351 nm for the CNT. This is consistent with a range of 0.345 to 0.365 nm for CNTs (104). (f) A foliate around 10 layers thick. As is typical for the foliates, it is thicker near the base where it is attached to the nanotube and gets thinner towards the edge (103).

TEM also indicated that both coherent and incoherent boundaries existed between the CNT sidewalls and the foliates (Figure 25(c) and Figure 25(d) (103)), respectively, where the coherent boundaries tended to be associated with smaller foliates. Theories of interface development in nucleation and growth of a new phase can provide some insights about the CNT–foliate interface (106). As a new phase nucleates on an existing surface, the interface between the two materials generally begins as a coherent boundary if the lattice mismatch is small. As growth of the new phase proceeds, interfacial dislocations tend to form to relieve the strain energy that builds at the interface due to mismatch of the lattices. When the nucleus reaches a critical size, the increase in volumetric elastic energy is greater than the interfacial energy and the interface becomes incoherent to relieve the elastic strain that has developed (106). Similarly, in the present case, the lattice mismatch between the foliates and the CNT sidewalls would result in coherent interfaces for small foliates in the early stages of nucleation and growth and incoherent interfaces between larger foliates and the CNT sidewalls as has been observed by TEM. The coplanar alignment suggests that the graphene foliates may have nucleated from defects or fractures in the CNT sidewall.

Figure 25(c) (103) shows a coherent interface, with the lattice fringes bending from the CNT sidewall to the foliate, suggesting a single continuous carbon layer can be part of both the CNT sidewall and the foliate. Figure 25(d) (103) shows an incoherent interface, where the foliate appears to have a break in the lattice fringes between the

CNT sidewall and the graphene layers. This could indicate a high angle twin (106) or a grain boundary between the CNT sidewall and the foliate. Additional evaluation of the lattice fringes [Figure 25(e) (103)] indicates that the fringe spacing for the CNT and the foliate is consistent with graphene lattice spacing. The lattice fringes were 0.362 nm (average of 11 fringes) for the foliate versus 0.351 nm for the CNT (average of 11 fringes). The trend in the fringe spacing is consistent with previous work on the variation of the layer spacing of graphene sheets as a function of CNT diameter that found a smaller number of layers have a larger lattice spacing (104, 107). Figure 25(f) (103) shows a thin foliate with approximately 10 fringes at the base and narrowing to just a few fringes at the tip.

Raman spectroscopy was used to characterize the different bonding states present in the g-CNTs compared to standard CNTs. Although the peak designations for Raman spectra of CNTs and graphene are still debated (compare designations of the band at 2700 cm^{-1} in Ferrari et al. (108) and Faugeras et al. (109)), there is reasonable consensus about the primary peaks designations. For CNTs and graphene, these peaks are the D, D', G, and G'. Their descriptions follow the review of Raman of CNTs and graphene by Dresselhaus et al. (110) Representative spectra from g-CNTs and standard CNTs are presented in Fig. 3, showing an increase in G' to G ratio when the foliate structures are present on the CNTs. This increase suggests the presence of graphene on the foliated CNTs. In summary, SEM, TEM, and Raman spectroscopy reveal several

characteristics of the g-CNTs. First, the CNTs have hollow cores and straight sidewalls (Figure 25 (103)). Second, the foliates grow out of the CNTs and are not simply attached by van der Waals bonding (Figure 25 (103)). Third, the nanosheets have a fringe spacing that agrees with published values for graphene layer spacing, i.e., greater than 0.35 nm (Figure 25(e) (103)). The thinnest foliates and tips of thicker foliates are graphene-like in their thickness (<10 layers), while the base of the thicker foliates are more graphitic, like the wall of the host CNT (Figure 25(e)). Fourth, Raman spectra of g-CNTs versus standard CNTs suggests, by changes in relative peak intensity, that there is a higher graphene component in the g-CNTs versus standard CNTs (Figure 26 (103)).

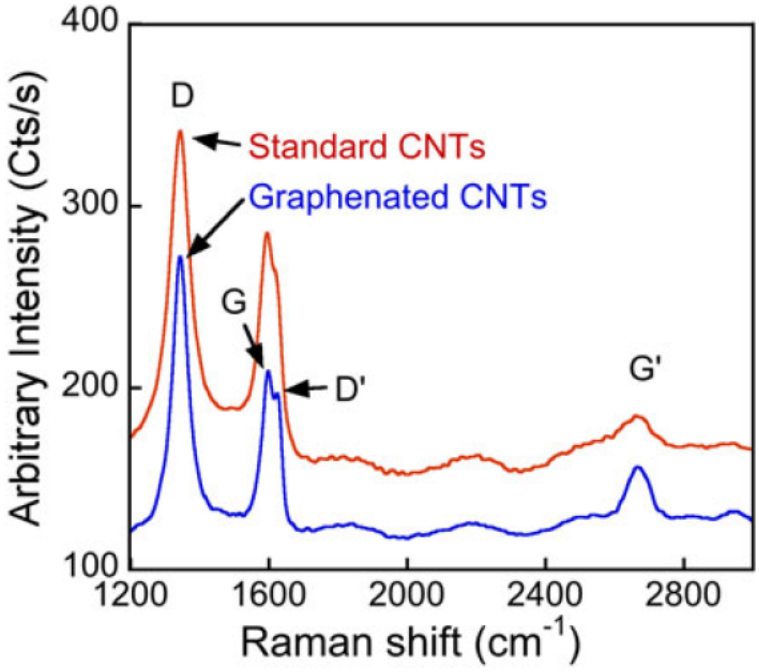

Figure 26: Standard CNTs are compared to g-CNTs. The expected increase for the ratio of G9 to G for the g-CNTs is observed. The spectra are smoothed to remove digitizer noise (103).

4.1.4 Applications for g-CNTs

g-CNTs should be interesting in several application areas, especially those that benefit from high surface area graphene edges. Carbon nanosheets on planar substrates do not utilize the third dimension (i.e., perpendicular to the substrate), limiting any improvement in surface area for applications such as electrochemical electrodes and catalyst supports, where high surface area is important. In addition, since only the outer CNT walls are involved in the foliate growth, the high electrical conductivity of the CNT stem is preserved. Finally, unlike planar structures, the graphenated CNT is a potential candidate for composites, from lightweight conductors to load-bearing structures. Problems reported for the bonding of CNTs to the matrix in these composites (98, 99) can be overcome using the reactivity of graphene edges present in these structures. The protrusions can also act as mechanical interlocking nanostructures to decrease slippage during deformation. An application area of growing interest for carbon nanostructures in general is as electrochemical electrodes for either energy storage (19, 111, 112) or neural stimulation (113-120).

4.1.5 Summary

g-CNTs have been grown with MPECVD. The graphitic foliates nucleate on the CNT surface during deposition and appear uniformly along the length. g-CNTs can be grown with consistency and controllability with respect to shape, size, density, and other morphological properties for both the CNT framework and the foliate structure.

The interface between foliates and the CNT sidewall has been characterized and is either a coherent or low-angle grain boundary. These structures may be ideal candidates for improved charge storage and other electrochemical applications.

4.2 Graphenated carbon nanotubes for enhanced electrochemical double layer capacitor performance

4.2.1 Introduction

Electrochemical double-layer capacitors or "supercapacitors" are gaining in popularity for applications ranging from hybrid structures in automotive energy storage to load leveling in power transmission (121, 122). Electrodes for neural stimulation also require high capacitance with both faradaic and non-faradaic components, and thus may benefit from improvements in electrochemical double layer capacitors (96). To optimize such capacitors, high charge density materials on the nano- and/or micro-scale are required, inspiring opportunities to engineer structures that integrate improvements on both scales. To optimize such capacitors, high charge density materials on the nano- and/or micro-scale are required, inspiring opportunities to engineer structures that integrate improvements on both scales. The growth and characterization of graphene foliates along the length of vertically aligned CNTs was discussed in the previous section. Yu et al. (123) also observed high density multi-layer graphene chemically bound to CNTs and examined their electronic and optoelectronic properties. This section covers structures with varying foliate density and their double layer capacitance is examined to provide insights for electrode applications. A microstructural classification

scheme is also proposed to describe the role of graphene edges, three-dimensional (3D) organization, and other features of hybrid carbon systems on their electrochemical properties.

The fundamental advantage of an integrated graphene- CNT structure is the high surface area three-dimensional framework of the CNTs coupled with the high edge density of graphene. Graphene edges provide significantly higher charge density and reactivity than the basal plane, but they are difficult to arrange in a three-dimensional, high volume density geometry. CNTs are readily aligned in a high density geometry (i.e., a vertically aligned forest) (79) but lack high charge density surfaces—the sidewalls of the CNTs are similar to the basal plane of graphene and exhibit low charge density except where edge defects exist. For example, Rice and McCreery (124) and others (92, 125-127) have reported that the capacitance expected for the basal plane of graphene vs. the edges is 3 vs. 50 to 70 $\mu F/cm^2$, respectively. Integrating the properties of these two nanostructures by growing protrusions or foliates of graphene from CNT sidewalls provides a means to optimize the hybrid structure, enabling significantly higher charge storage capacity than either of the two materials can achieve on their own. These structures are referred to as "graphenated CNTs" and the individual multi-layer graphene protrusions are referred to as foliates due to the leaf-like nature, growing from the CNT stem.

4.2.2 Experimental

The details for the g-CNT growth process have been described in the previous section. The foliate density was controlled by controlling the deposition time in the last step of the MPECVD growth process. As seen in Figure 27(a)-Figure 27(c) (128), the deposition times of 60 s to 480 s resulted in increasing foliate density.

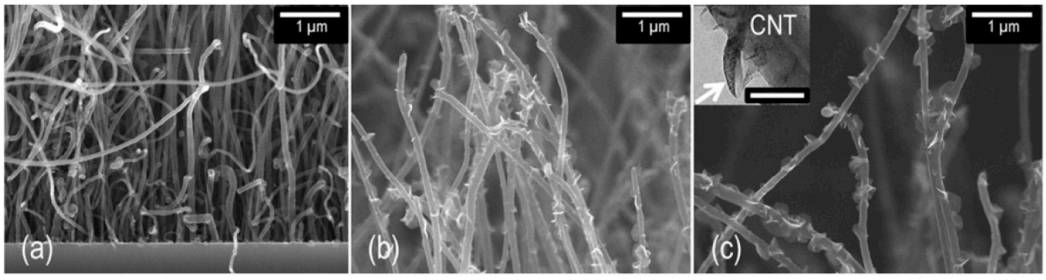

Figure 27: SEM micrographs of the graphenated CNTs as a function of deposition time. The foliate density increases as a function of deposition time (a) 180 s, (b) 360 s, and (c) 480 s (Inset: TEM of graphene foliate showing hollow CNT core. Foliate indicted by the arrow. Scale bar is 100 nm.) (128)

The inset in Figure 27(c) (128) is a TEM image of a typical foliate, showing a multi-layer graphene structure, coherent with the CNT sidewalls. For the purpose of this study, only the deposition time was varied so as to limit effects of microstructural changes to the underlying CNT framework caused by expanding the process space.

The specific capacitance was measured using EIS between 0.1 Hz and 100 kHz using a 1252 frequency response analyzer and 1287 electrochemical interface (Solartron Analytical) with an Ag-AgCl reference electrode in Model ISF, a biological simulant electrolyte. These CNT-electrodes were initially developed for neural stimulation, thus, a biological simulant (129) was utilized as the electrolyte. Other electrolytes with similar

conductivity are expected to provide similar trends in capacitance, and more conductive electrolytes (e.g., 25% KOH a standard aqueous electrolyte used in supercapacitor measurement) should result in a higher initial capacitance due to the lower solution resistance. Future research will evaluate the g-CNT structures in electrolytes optimized for supercapacitor performance. The purpose of this letter is to report on the effect of adding graphene structures to aligned CNTs and the preliminary capacitance trends as a function of foliate density. Capacitance was obtained by performing EIS scans over the above frequency range and then fitting the impedance magnitude and phase data to the electrode equivalent circuit model shown in Figure 28 (128). A model with a parallel combination of C1 and C2 was examined and provided a better fit to the data than a single R-C model (nonetheless, trends of capacitance vs. graphene foliate density were similar for both cases). Given the hybrid structure of the g-CNT, it can be hypothesized that C1 is associated with the double-layer capacitance (attributed primarily to the exposed graphene edges and edge defects in the CNT sidewalls) and C2 with the pseudo-capacitance (attributed to Faradaic charge transfer reactions across the interface). However, our goal for the current work is simply to report on the effect of increasing graphene foliate density on capacitance. Future work will examine such an assignment of C1 and C2 to determine its validity. In this circuit model, resistor R2 is the resistance associated with charge transfer and Rs is the equivalent series (or solution) resistance of the electrolyte.

4.2.3 Results and Discussion

For the purpose of future comparisons, the capacitance data were normalized with respect to area and mass of the exposed g-CNT film. The mass normalized results are shown in Figure 29 (128) and similar trends were observed on a specific nominal area basis (not shown). The data were fit over two frequency regimes: low frequency (1–10 Hz), representing energy storage, or load leveling types of applications for super capacitors; and high frequency (10 Hz–10 kHz), representing applications such as neural stimulation which require pulsed or high frequency operation.

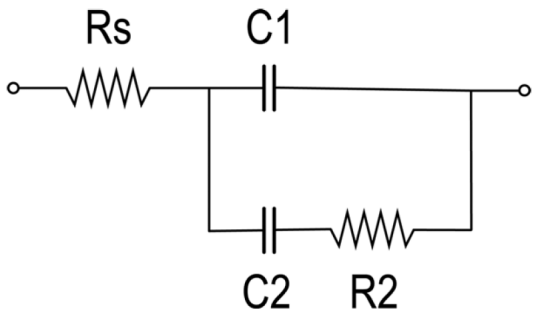

Figure 28: Equivalent circuit model used for EIS analysis of electrode electrolyte interface. Rs represents the solution resistance, C1 the double layer capacitance due to linear edge defects, C2 the Faradaic pseudocapacitance, and R2 the charge transfer resistance (128).

The capacitance data for both low and high frequency regimes are plotted in Figure 29(a) (128) as a function of deposition time. Both C1 and C2 show increases as a function of deposition time, which corresponds to foliate density, at low and high frequency, suggesting that optimization of a hybrid CNT-graphene structure should

lead to further improvements over either of these two structures optimized on their own.

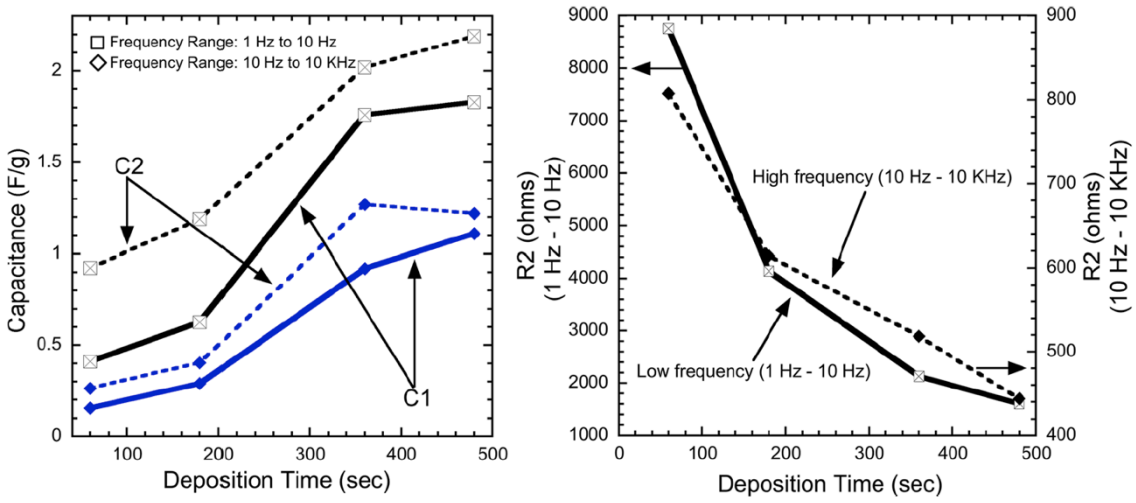

Figure 29: (Color online) Plots as a function of g-CNT deposition time based on EIS analysis for (a) Capacitance, double layer (C1) and pseudo-capacitance (C2) and (b) charge transfer resistance (R2) (128).

It is interesting to note that there are measurable increases in capacitance from 60–180 s, before graphene foliates are observable via SEM. The first foliates are not visible until after 180 s, yet there is already a greater than 2X improvement in capacitance. The initial increase in capacitance prior to noticeable formation of graphene foliates may be due to the formation of edge-type defects along the length of the CNTs; defects that form the nucleation sites for the graphene foliates. In fact, there are noticeable undulations along the length of the CNTs prior to foliate formation (130), suggesting defects and compressive stress. Fracture following excessive compressive stress is hypothesized as a foliate nucleation mechanism and may provide sufficient edge defects even before foliates are observed via SEM. The primary difference between

the high and low frequency data is the charge transfer resistance (R2), shown in Figure 29(b) (128). In both regimes, R2 decreases as a function of deposition time and foliate density, representing a decreasing RC time constant for charge transfer, consistent with an increase in the density of reactive graphene edges. However, over the higher frequency regime, R2 is an order of magnitude lower, suggesting that the R2-C2 combination is more efficient (faster) at higher frequency charge transfer. Ongoing research is designed to isolate this mechanism and study the frequency dependent charge-transfer effect and its correlation to the g-CNT microstructure. In addition, the structures will be optimized for charge storage. A higher density of graphene foliates, as shown in Figure 30 (128), will also be examined during that optimization.

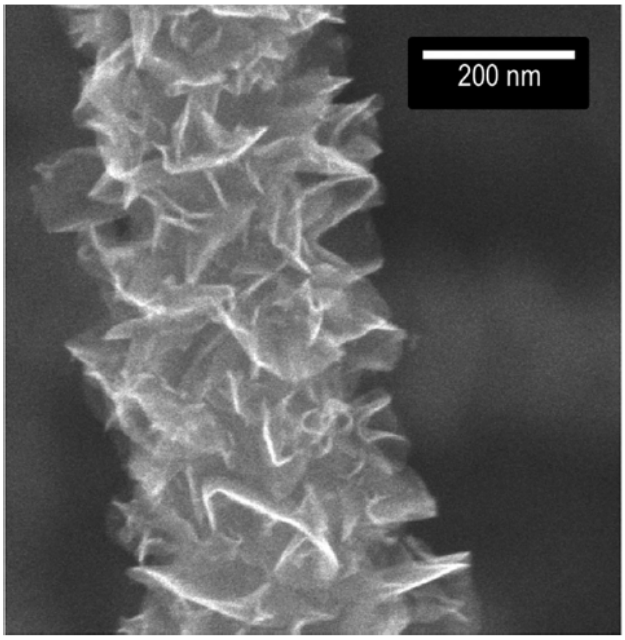

Figure 30: SEM of an ultra high foliate-density graphenated CNT (128).

To help explain the properties of this CNT-graphene hybrid, Table 5 (128)

outlines a microstructural classification of various carbon nanostructures in the context of their edge or basal plane exposure and whether they are predominantly planar or organized in a 3D network. For a comprehensive review of carbon electrode materials for electrochemical applications, the reader is also referred to the excellent review by McCreery (127).

Table 5: Microstructural classification of carbon nanostructures for electrochemical capacitors (128).

Structure schematic	Examples	Description	Reference
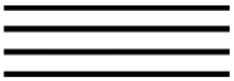	HOPG	Low charge density. Primarily graphene basal plane exposure	Kneten *et al*. (131) and Inaba *et al*. (132)
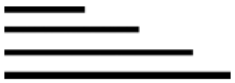	Graphite	Mostly basal plane exposure with moderate density of edges	Flandrois *et al*. (133) and Zoval *et al*. (134)
	Herringbone fibers	Mixture of edge and basal plane exposure	Gulijk (135)
	Edge-textured nanosheets	Mostly edge exposure of graphene or graphite nanosheets	Wang *et al*. (136)
	Activated carbon	Mesoporous structure organized into a 3D network with mixture of edge and basal plane	Ryoo *et al*. (137)
	g-CNTs	Graphene foliates with both edge and basal plane exposure, organized in 3D structure	Yu *et al*. (123) and Parker *et al*. (130)
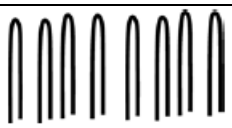	Aligned CNTs	3D organization of CNTs with mostly basal plane exposure	Cui et al. (79)

The present research focuses more on the role of specific carbon nanostructures in relationship to the g-CNT hybrid material. The table starts with highly oriented pyrolytic graphite (HOPG) (131, 132), which is dominated by large areas of basal plane exposure, and then transitions through microstructures that have increasing edge exposure (133-137) but still are essentially two dimensional (i.e., a single unstacked layer of edges), and then on to three-dimensional organization represented by the g-CNTs (Refs. (130) and (123)) and aligned CNTs (79). Optimizing this microstructure for double-layer capacitance involves a combination of geometric, microstructural, and electronic factors, all leading to an increase in charge storage capacity. Graphene nanosheets, with their high density of exposed graphene edges, have significantly higher surface charge density than CNTs and HOPG, but are planar structures and difficult to organize in a 3D network. Aligned CNTs provide a well-organized, high surface area 3D geometry, but have primarily basal plane exposure. The g-CNT structure represents a potential maximum in both charge density and surface area, representing the 3D organization of the high charge-density graphene edges, arranged into a larger electrochemically active volume. Thus, on a specific density or nominal area basis, such structures provide the highest capacitance.

4.2.4 Summary

This section presents enhanced electrochemical double-layer capacitance as a function of increasing graphene foliate density along aligned CNTs. Both high and low

frequency measurements showed significant increases in capacitance with increasing foliate density. This increase is attributed to the higher surface charge density present at graphene edges in combination with the 3D organization of the graphene foliates achieved via a network of aligned CNTs.

4.3 Transitions from vertically aligned carbon nanotubes to graphenated carbon nanotubes to vertically oriented carbon nanosheets and their corresponding electrochemical behavior

4.3.1 Introduction

The MPECVD reactor used to grow vertically aligned CNTs and g-CNTs is very versatile in that the same system can be used to grow different form of nanostructured carbon by changing growth conditions. A systematic parametric study of the MPECVD reactor was conducted gain insights into growth mechanisms and transition between the different types of nanostructured carbons. A DOE approach was utilized to understand the range of growth permitted in a MPECVD reactor, with a focus on identifying graphenated carbon nanotube growth within the process space. One of the key outcomes of the study was that for the first time, three distinct morphologies and dimensionalities of carbon nanostructures (i.e. 1D CNTs, 2D CNSs, and 3D g-CNTs) have been synthesized in the same reaction chamber by varying only a single parameter (temperature). Apart from facilitating prediction and modeling morphological characteristics various nanostructures, a relationship between deposition temperature and specific capacitance emerged as a result of this study.

4.3.2 Experimental

4.3.2.1 Materials Synthesis

N-type conductive silicon (100) wafers with resistivity 1 Ω/cm were coated with iron catalyst at RTI International using a CHA electron beam evaporation system. Wafers were coated with 2, 5, and 10 nm Fe catalyst layers, yielding three different thicknesses for the parametric study. Carbon nanostructures were grown using a 915 MHz MPECVD system. Details of the deposition system can be found in previous chapters and Cui et al (79).

The screening experiments preceding the DOE employed a process space, as seen in Figure 31 (138), comprised of temperature, pretreatment time, and gas ratio. Probing the corners of this cube revealed vertically aligned CNTs on the 800 °C plane, and ribbon-like carbon nanosheets on the 1100 °C face. This nanosheet morphology was achieved using the same substrate and growth conditions, aside from temperature, as carbon nanotube films. The full experimental design incorporated temperature, gas ratio, pretreatment time, deposition time, and catalyst thickness as factors; and for the purpose of this discussion, capacitance as response (for details refer Appendix A).

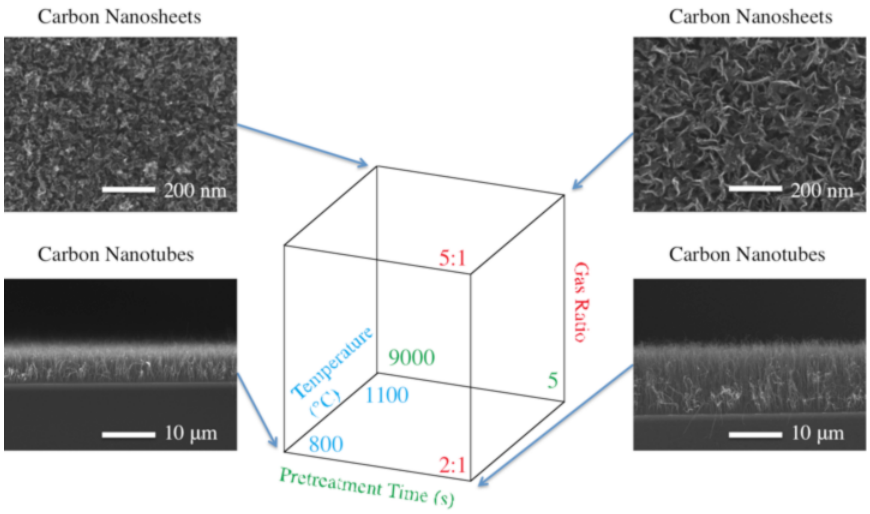

Figure 31: A set of DOE screening experiments preceded the full process space analysis for the purpose of identifying key factors that most strongly affect carbon nanostructure morphology. The screening runs, in this case, highlight the temperature-driven shift from the CNT to CNS morphology (138).

4.3.2.2 Electrochemical Setup

The electrochemical setup, including the cell and sample preparation, has been discussed in detail in a previous publication (59). Briefly, a three terminal electrochemical cell with working, counter, and reference electrodes (K0235 by Princeton Applied Research) was used. The working electrode was the nanostructured electrode under study, the counter electrode was a Pt mesh (3 cm—2.5 cm), and the reference was an Ag wire in 1 M tetrabutylammonium perchlorate (TBAP) and 0.01M silver nitrate ($AgNO_3$) in acetonitrile (reference electrode-RE-7 and its solution supplied by BioLogic). The reference electrode resided in a separate subsection of the cell connected to the region near the double layer interface of the working electrode by a Luggin-Haber

capillary tube. The electrolyte used was 1 M $LiClO_4$ in acetonitrile. The potentiostat was a SP-300 (Bio-Logic). All chemicals were used as received.

4.3.2.3 Sample Preparation and Electrochemical Measurement

The sample was mounted on a piece of sheet metal using copper tape. An electrical contact was made by painting conductive silver epoxy on the nanostructure side. The nominal active area of the electrode as defined by a PTFE gasket was 1.43 mm^2. Cyclic voltammetry, galvanostatic charging/discharging and electrochemical impedance spectroscopy were performed on all the samples. Values of specific capacitance were calculated from cyclic voltammetry performed at a scan rate of 50 mV/s

4.3.3 Results and Discussion

4.3.3.1 Temperature Effects on Morphology

The most influential factor in determining film morphology during the parametric study was temperature (Figure 32 (138)). By varying temperature alone, the resultant film could consist of carbon nanotubes, graphenated carbon nanotubes, or carbon nanosheets. To further illustrate this result, a temperature series was conducted using growth conditions of 180 sec pretreatment time, 120 sec deposition time, 3:1 CH_4:NH_3 ratio, and 5 nm Fe catalyst layer for each experiment. As seen in Figure 32 (138), an increase in process temperature from 950 °C to 1000 °C transitions the resultant nanostructures from CNTs to g-CNTs, and tubes are no longer present in the CNS structure grown at 1100 °C. Thus, g-CNTs have emerged as an intermediate structure

that lies between these two well-studied morphologies with respect to the growth temperature.

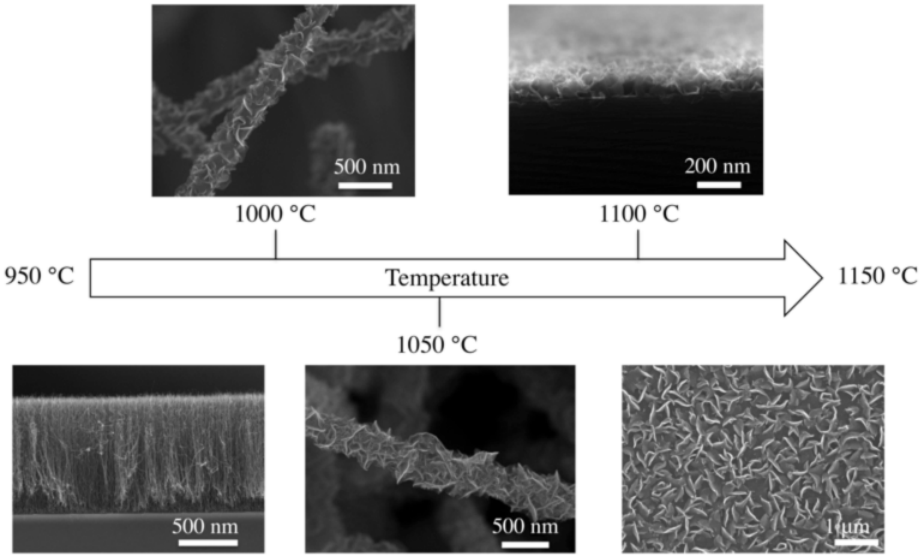

Figure 32: The morphology of the resultant films varies dramatically from the CNT structure at 950 °C, to g-CNTs at 1000 °C and 1050 °C, to CNSs at 1100 °C under constant growth conditions (138).

Recently, Stoner and Glass (139) proposed a classification scheme for characterizing nanostructured carbon materials based on density of exposed graphene edges, called the Electron Density of Graphene Edges (EDGE) Triangle (Figure 33) (139). Based on studies by Randin and Yeager (92, 140, 141) comparing the capacitance of basal- and edge- exposed HOPG, graphene edges have an approximated 20x improvement in specific capacitance compared to planar graphene. As a result, the specific capacitance of a sp^2-bonded carbon structure is a function of the relative concentration of edge plane exposure (92, 142). As shown herein, varying temperature alone allows a transition between aligned carbon nanotubes, graphenated carbon

nanotubes, and vertically oriented graphene nanosheets. Thus, all three corners of the EDGE triangle can be traversed in a counter-clockwise direction by increasing temperature, which produces structural morphologies starting from the bottom edge (a-CNTs) to the right side edge (g-CNTs) to the left edge (CNS). In summary, this corresponds to vertical arrays of 1D structures (a-CNTs) transitioning to 3D structures (g-CNTs), and then finally to 2D structures (CNSs) with increasing temperature.

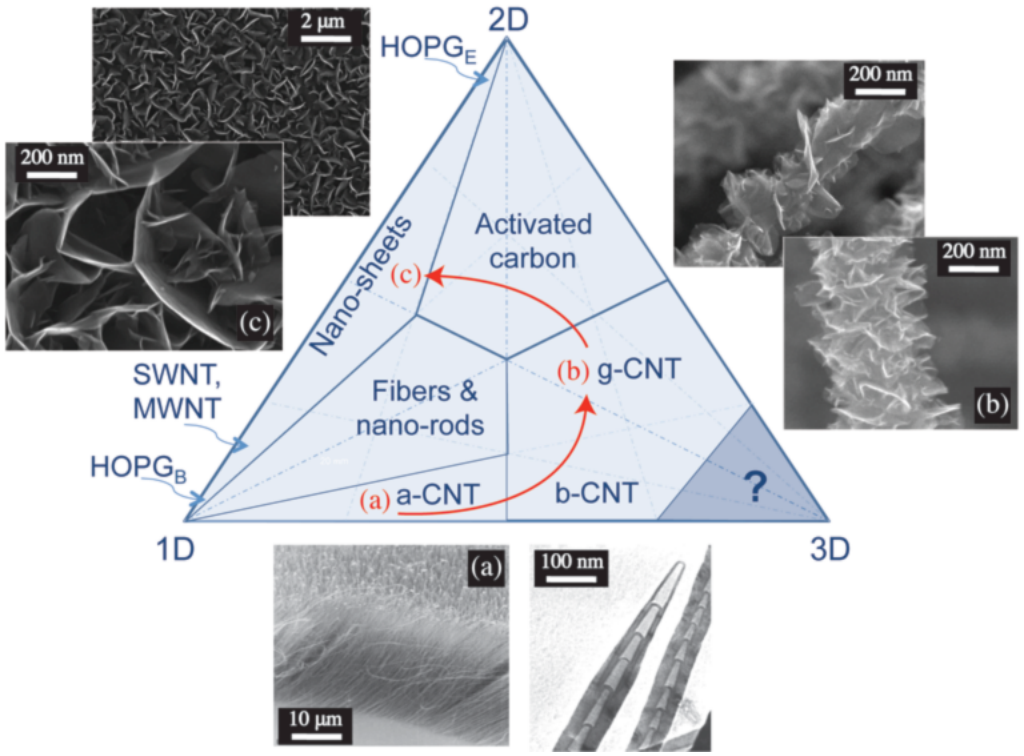

Figure 33: Electron Density of Graphene Edges (EDGE) Triangle, adapted from (143). The arrows indicate morphological changes that occur as process temperature is increased, from (a) aligned CNTs to (b) graphenated CNTs to (c) nanosheets (139)

4.3.3.2 Temperature Effects on Specific Capacitance

A least squares prediction profile from the DOE offers additional evidence of the relationship between temperature, morphology, and capacitance (Figure 34 (138)). The dashed lines in this plot represent 95% confidence intervals, and the solid line is a least squares curve generated from data points obtained during the parametric study. It is noteworthy that while temperature is the only process parameter represented in this plot, data from variations within other process parameters are included here as well. For instance, capacitance data points at a certain temperature may originate from films grown at several pretreatment times or gas ratios, which were included in the least squares model. In this way, capacitance may be analyzed as a function of deposition temperature in the context of the entire parametric study. The local maximum in capacitance that is clear from this plot exists in the temperature regime that resulted in graphenated carbon nanotube growth during this study (925-1050 °C), indicating that the presence of graphenic foliates improves the capacitive response of the material.

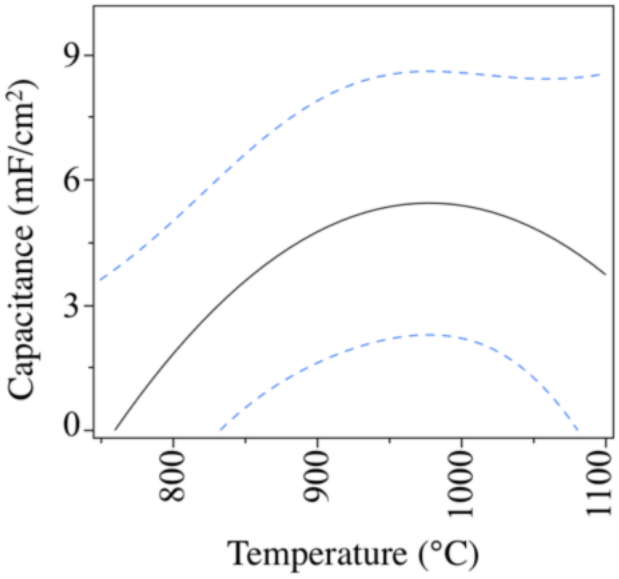

Figure 34: Standard least squares prediction profile of capacitance (mF/cm²) as a function of deposition temperature (°C) across all other variables within the parametric study. The local maximum exists in the g-CNT morphological regime (138).

This effect of foliates on capacitance is further reinforced by correlating the capacitance to the I_D/I_G ratio obtained from the Raman spectra of each sample. Figure 35 shows the mean capacitance for five different ranges of I_D/I_G ratios obtained from the samples. It is clear that the mean capacitance increases with increase in I_D/I_G ratio. Figure 35 (inset) shows the plot of individual capacitances versus the respective I_D/I_G ratios. There is a definite monotonically increasing relationship between capacitance and I_D/I_G ratio.

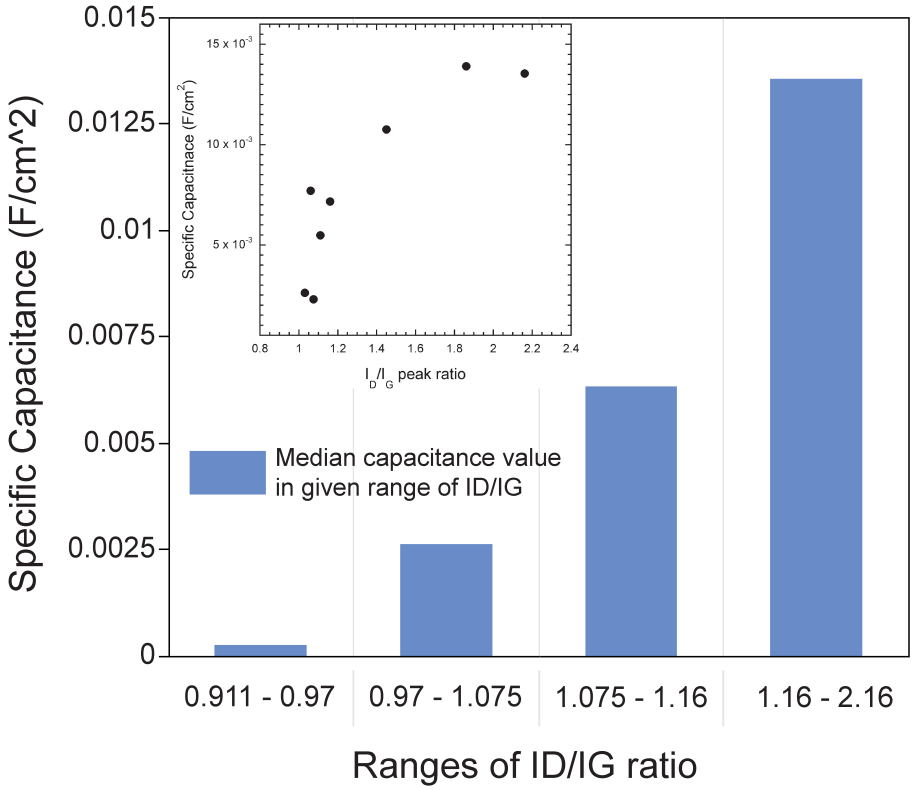

Figure 35: Median values of specific capacitance versus ranges of peak I_D/I_G ratios of the samples from the design of experiment study. Inset: Scatter plot of specific capacitance versus peak I_D/I_G ratio.

It should be noted that five data points from the study have been excluded from Figure 35. Four of the samples had no regular carbon film deposition but instead only had catalyst nanoparticles and sparse and irregular carbon structures. The fifth data point was excluded based on the Grubb's test for outliers with 95% confidence.

From the Raman spectra of all the samples, D peak to G peak ratios were obtained for each sample. The Tuinstra and Koenig (TK) relation states that the cluster diameter or crystallite size is inversely proportional to I_D/I_G ratio (144). Using the TK relation, crystallite sizes for each sample were calculated from I_D/I_G ratio and laser

wavelength (145). The crystallite sizes were plotted against the measured specific capacitance. As seen in Figure 36, there is a linear inverse relationship between specific capacitance and crystallite size. This is in accordance with the observations from previous section of this chapter about g-CNT foliate density and capacitance. A smaller crystallite size means that the density of grain boundaries is higher. Since defects exist at grain boundaries, a smaller crystallite size means higher defect density. In g-CNTs, foliates are formed preferentially in locations where sidewall defects exist (103). Thus specific capacitance is inversely proportional to crystallite size and hence directly proportional to defect/edge density.

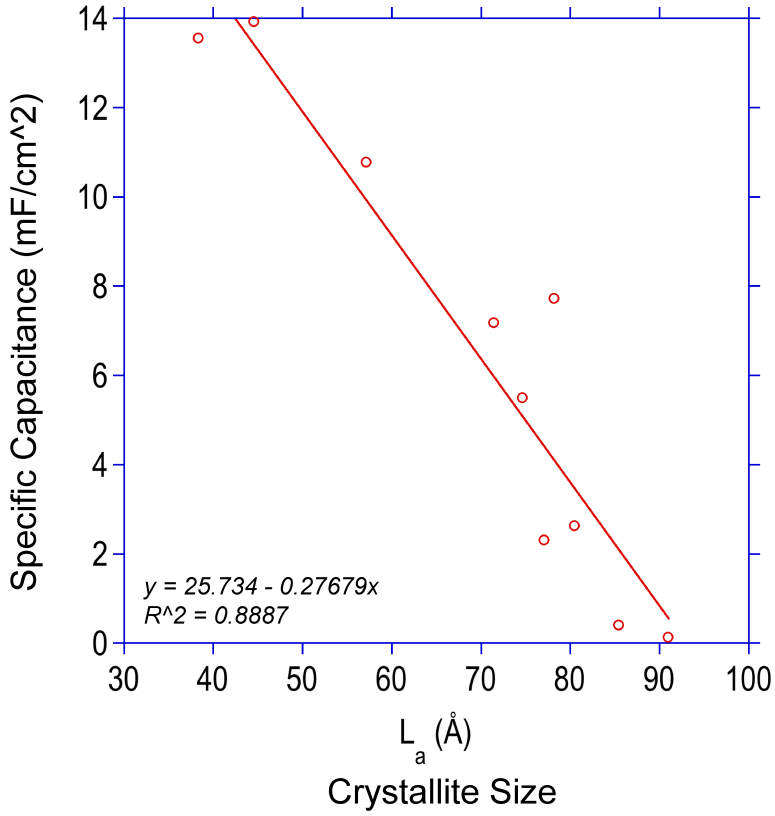

Figure 36: Plot of specific capacitance versus crystallite size.

4.3.4 Summary

The growth temperature of an MPECVD process was used to control the dimensionality and morphology (especially graphene edge density) of carbon nanostructures. Based on statistical trends in this study, a parametric temperature series revealed that deposition temperature is the key factor in controlling nanostructure morphology, and g-CNTs emerged as a temperature-based transitional morphology between CNT and CNS structures. As predicted (143), the edge density had a significant effect on specific capacitance with the nanostructure containing greatest graphene edge density, g-CNTs, exhibiting the highest specific capacitance. That specific capacitance is

proportional to edge density was also observed by comparing specific capacitance to crystallite sizes calculated from the Raman spectra.

4.4 Conclusion

g-CNTs with their edges and high surface area make for a promising material for energy storage, neural stimulation and other electrode applications. Capacitance was higher for g-CNTs with higher foliate density. This is in agreement with literature which states that the edges carbon nanostructures have ~20X higher capacitance than basal plane (92). Moreover g-CNTs exhibit higher capacitance compared to regular CNTs, CNS and other structures synthesized as a part of the design of experiment study. Finally, it was also observed that specific capacitance has a linear inverse relation with crystallite size. Crystallite size is directly proportional to defects owing to grain boundaries. Thus a higher defect density, lead to higher specific capacitance for carbon nanostructures synthesized in the MPECVD system.

5. Electrochemical disinfection of human urine for water-free and additive-free toilets using boron-doped diamond electrodes

Previous chapters have examined the electrochemical behavior of sp^2 bonded forms of carbon, including carbon nanotubes and graphene. The effect of carbon edges were evaluated which are known to be reactive and exhibit high capacitance. In this chapter, another prevalent form of carbon, diamond, is examined due to its three dimensional sp^3 bonded network of carbon with no edge planes. This structure enables what is termed a "wide electrochemical window" for electrochemical reactions in acqueous environments. That is, water electrolysis occurs at high overpotentials. This enables applications that benefit from electrochemical reactions that may not occur on other electrodes because water is reduced or oxidized before the potential can support such reactions. In addition, the diamond is stable in extreme environments compared to CNTs and graphene; again due to the lack of reactive edges. Thus, this chapter focuses on the use of BDD as anodes for electrochemical generation of mixed oxidants for disinfection of bacteria and its demonstration in synthetic human urine with suspended fecal particles. The BDD anodes are used in a liquid disinfection module of a new toilet being designed for the less developed parts of the world where disease due to lack of sanitation is a problem. Techniques to minimize energy consumption in the electrochemical process are also discussed.

5.1 Introduction

According to a World Health Organization report (1), 2.6 billion people on the planet do not have access to adequate sanitation. In the less developed world where the problem is more acute, 1.5 million people (mostly children under the age of 5) die every year due to diarrhea resulting from inadequate sanitation. Improved sanitation can reduce diarrhea morbidity by 32% on average. As a part of the larger project, the overall scope of which is beyond that of this dissertation, an energy-neutral, additive-free, water free outdoor toilet is being developed for use in the developing world. This toilet can treat human liquid and solid waste at point-of-source. As seen in Figure 37(b) the toilet waste treatment unit includes an auger-based solid liquid separation system underneath the squat plate, separates the liquid waste from the solid waste. The solid waste is dried and combusted whereas the liquid waste is disinfected electrochemically by using boron-doped diamond electrodes. Part of the heat from the combustion process of the solid waste is captured and converted to electricity. The electrochemically disinfected wastewater can be used as rinse water for the toilet or as fertilizer supplement. The entire waste treatment unit shown in Figure 37(b) (146) fits inside the toilet housing shown in Figure 37(a) (146).

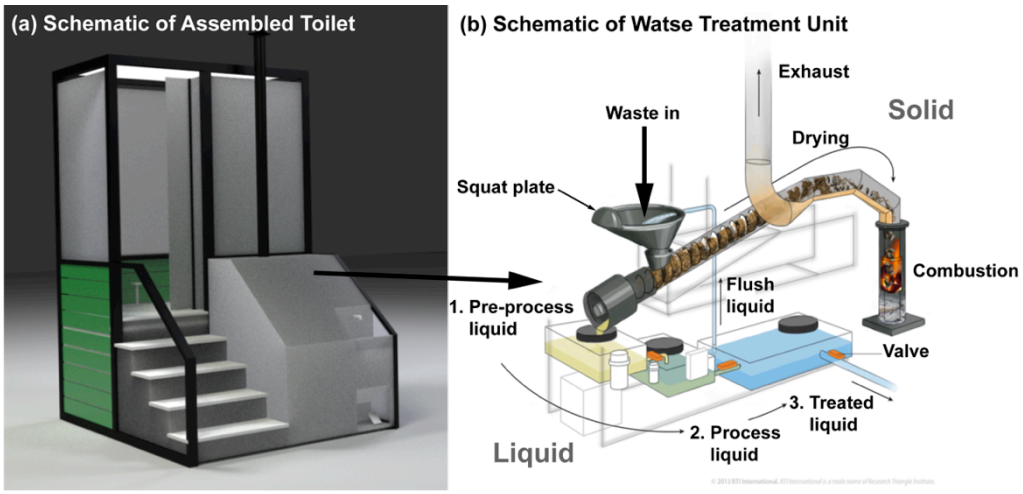

Figure 37: Schematic of the proposed toilet (a) fully assembled toilet (b) schematic of waste treatment unit that goes inside the toilet housing in (a) (146)

Addressing the critical sanitation needs of communities in less developed nations requires disinfection techniques for human waste that do not require added water, chemical reagents, or energy in excess of that which can be easily produced by the waste itself or local energy sources such as solar panels. Electrochemical disinfection of liquid waste refers to the elimination of microorganisms present in the liquid by using suitable electrodes to initiate pathogen-killing electrochemical processes in the influent waste stream. The electrochemical disinfection method reported here produces hypochlorous acid/hypochlorite as a parallel reaction to oxygen evolution at the anode. These chlorine containing species (CCS) are derived from chloride ions present in urine. The generation of other reactive oxygen species (ROS) such as ozone, hydrogen peroxide and hydroxyl radicals is also expected. These ROS and CCS are responsible for bacterial inactivation. Electrochemical techniques have been reported in the past for inactivation of pathogens

(147-151). Electrochemical disinfection has also been shown to be more effective at bacterial inactivation than purely chemical chlorination or ozonation (152), despite the fact that similar species are believed to be key ingredients of the electrochemical disinfection.

A good anode for electrochemical disinfection should possess a large oxygen evolution overpotential so that most of the applied current is utilized for generation of disinfecting oxidants rather than oxygen. This improves the energy efficiency of the electrode as charge is not wasted in evolution of non-disinfecting species. In addition, the electrode must be chemically stable in the electrolyte of interest. BDD possesses both of these attributes in aqueous electrolytes and thus is a suitable electrode for wastewater disinfection (153, 154). For BDD electrodes, hydrogen evolution occurs at -1.25 V versus a standard hydrogen electrode (SHE) and oxygen evolution occurs at + 2.3V versus SHE (36). A higher overpotential means that applied charge is not subverted to the oxygen evolution reaction but is used to generate disinfecting oxidants. BDD electrodes have been utilized previously for removal of phenols (46), biofilms (155), nitrogen-heterocyclic compounds (156), etc. Previous reports about BDD electrodes have covered disinfection of wastewater, ballast water, river water, etc. (157-159).

BDD surface like the one used in this study, is largely hydrogen terminated. There is absence of electroactive carbon-oxygen functional groups. The density of electronic states near the Fermi level in BDD is lower than metals due to the semi-metal-

semiconductor nature of BDD (38). A lower surface charge carrier density causes lesser accumulation of counter-balancing ions causing a reduction in background current and capacitance and there is little surface adsorption on BDD surface (160). All of this contributes to very little fouling on the surface. Also, BDD electrodes can be reverse polarized to remedy fouling. This is not possible in other electrodes such as DSA without causing degradation of the electrode.

Various oxidants such as chlorine, ozone, and hydroxyl radicals are generated at voltages less than 3 V (161) on BDD in NaCl solution. However, reports differ on the ability of diamond to generate these oxidants when compared to other electrodes such as dimensionally stable anodes (DSAs) or mixed-metal oxide electrodes. It has been suggested that diamond electrodes are not efficient in chlorine generation as compared to DSAs and, owing to their high overpotential for oxygen and chlorine evolution, may generate chlorate and perchlorate (162). Wu et al. (163) reported that BDD electrodes were more efficient than DSA electrodes in treating chloride-free dye wastewater but the dye oxidation rate was higher with DSA than BDD at treating chloride-containing wastewater. However, BDD electrodes were shown to be more efficient than Ti/RuO2 and Pt electrodes in OH- radical production (164). It has been reported that bacterial inactivation at BDD anodes may be due to simultaneous presence of different oxidants such as hydroxyl and peroxide radicals rather than only chlorine species (149). Polcaro et al. (165) suggested that the contribution of various oxidants towards removal of

pollutants depends upon the initial chloride concentration and that at high initial chloride concentration; chlorine species are the primary oxidants. In the present study, higher rates of disinfection at higher applied voltages corresponded with higher rates of generation of total chlorine. It is likely that disinfection of wastewater at BDD electrodes is due to a combination of chlorine species and other oxidants such as OH- radicals and ozone. However, the contribution of chlorine species towards disinfection seemed to be higher than other oxidants due to the presence of higher concentration of chloride ions in urine.

5.2 Disinfection of synthetic human urine and synthetic fecal matter using boron-doped diamond electrodes

Herein, we report on the disinfection of synthetic human urine and feces using an electrochemical cell comprised of a boron-doped diamond anode and tungsten cathode at different applied voltages and hence different current densities. Total chlorine was measured and used as an indicator of electrochemically generated oxidants. The effect of suspended synthetic feces (1% and 2% w/v) in synthetic urine on the disinfection process was also studied. Finally the energy and time required for disinfection for different voltages was calculated. To our knowledge, no previous literature reports have focused on developing a liquid disinfection system that can treat undiluted human urine at point of source, operate without flush water or added reagents and will be able to handle small amounts of suspended fecal particles with the associated bacteria.

5.2.1 Experimental

5.2.1.1 Electrodes

Boron doped ultrananocrystalline diamond (UNCD) (166) electrodes were supplied by Advanced Diamond Technologies (Romeoville, IL) were used for this study. The anode was a niobium substrate with a 2 μm thick boron doped ultrananocrystalline diamond film. The film resistivity was <0.1 ohm-cm. The cathode was a tungsten plate. . The electrode area of each electrode was 42 cm^2. A 2 mm spacer separated the two electrodes. As shown in Figure 38, the liquid being treated entered the undivided gap between the two electrodes from flow openings at the bottom of the BDD anode. Because of the flow pressure, it rose through the gap and exited through flow openings at the top of the tungsten cathode. The liquid underwent electrochemical oxidation during its dwell time in the inter-electrode gap.

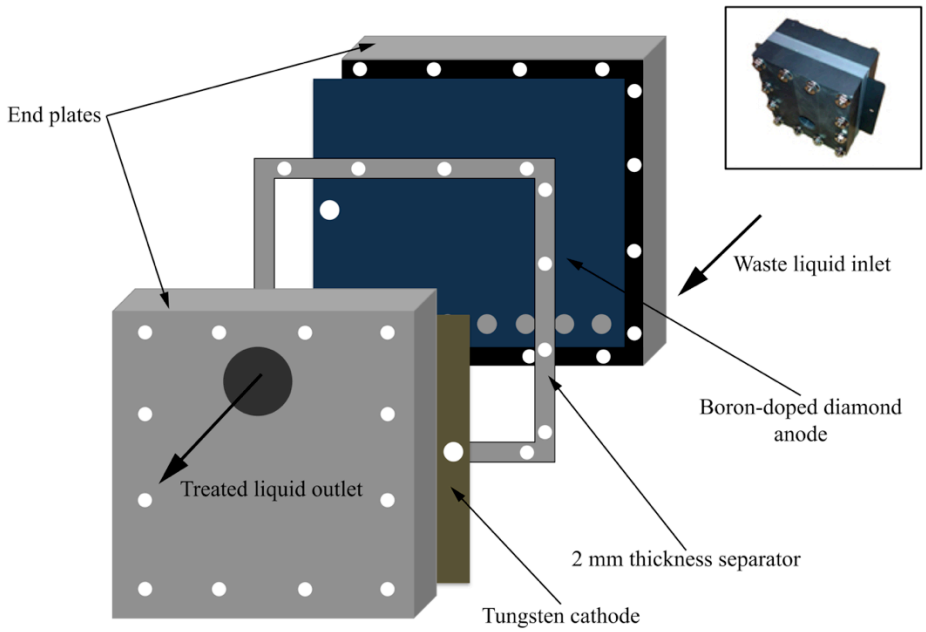

Figure 38: Schematic of disassembled electrochemical cell (Inset: Picture of the assembled cell)

5.2.1.2 Electrolytes

For initial tests in this study, 2 L 0.9% w/v NaCl solution was used as the electrolyte spiked with 1 mL/L of FD&C Green No. 3 dye (ethyl-[4 -[[4- [ethyl-[(3-sulfophenyl) methyl] amino] phenyl]-(4-hydroxy-2-sulfophenyl) methylidene] -1-cyclohexa-2,5-dienylidene]-[(3-sulfophenyl) methyl] azanium dye) as model contaminant. The discoloration of the dye was used as an indirect measure of the amount of oxidants generated.

5.2.1.3 Synthetic Excreta

For studying inactivation of bacteria in human waste, synthetic urine and feces were used as simulants. The recipe (Table 6 (167)) for synthetic urine was adopted from

those suggested in prior literature (168, 169). This synthetic urine electrochemically mimics real human urine (refer Appendix B). Synthetic urine prepared this way was sterilized in an autoclave at 121 °C and 15 psi for 20 minutes. After cooling to room temperature, this sterile urine was spiked with a suspension of E. Coli. Synthetic fecal matter was used to study the effect of suspended organic solid particles on the disinfection process. It was prepared using the recipe given in

Table 7 (167) and kept refrigerated until used. Synthetic fecal matter was added to the E. Coli spiked urine to determine its effects on the disinfection process. 1% w/v and 2% w/v mixtures of fecal matter in spiked urine were prepared.

Table 6: Constituents in Synthetic Urine (167)

Chemical	Quantity (per L of deionized water)
Sodium sulfate	2.34 g
Potassium chloride	3.88 g
Ammonium hydroxide (28-30%)	1.33 mL
Magensium sulfate (heptahydrate)	0.49 g
Phosphoric acid (85% aqueous solution)	0.25 mL
Sodium hydroxide	0.14 g
Sodium chloride	9.93 g
Trisodium citrate (dehydrate)	0.47 g
Urea	30.3 g
Creatinine	1.47 g
Hippuric acid	0.54 g
Uric acid	0.5 g

Table 7 Constituents in synthetic fecal matter (500 g) (167)

Substance	Weight (g)
Dried yeast	30
Microcrystalline cellulose	10
Psyllium husk powder	17.5
Oleic acid	20
Miso paste	17.5
Potassium chloride	2
Sodium chloride	2

5.2.1.4 Indicator Organism

The indicator organism used in this study was Escherichia coli K12 (ATCC #10798). It was grown in a broth containing 10 g/L, tryptone, 5 g/L yeast and 10 g/L NaCl to deionized water. The broth was then sterilized at 15 psi and 122 °C for 15 minutes. After cooling to room temperature, the E. Coli broth was inoculated from a stock culture using aseptic techniques. The culture was incubated at 37 °C for 24 hours. After incubation, the 200 mL of broth mixed with 1.8 L of sterile synthetic urine yielding 2 L total urine.

5.2.1.5 Experimental Setup

The electrochemical cell (Advanced Diamond Technology's Diamonox 40 system) was incorporated into a lab scale setup consisting of an 8 L storage tank, drain valve, strainer, and AC pump. A photograph of this assembly is shown in Figure 39 (167). The liquid being treated is initially held in the storage tank. During disinfection experiments, both electrochemical cell and pump are turned on. The liquid is pumped

from the storage tank through the electrochemical cell and returned to the storage tank, thus forming a closed loop. The filter cartridge in the loop was circumvented to study the effects of fecal matter on disinfection. A Sorensen XHR 33-33 (0-33 V, 0-33 A) power supply was used to power the electrodes at selected voltages ranging from 4 to 12 VDC depending on the experiment. The temperature of the NaCl solution or synthetic urine at the start of the tests was 23.5 °C. The temperature of the liquid increased by approximately 10 °C during the experiments, mostly for experiments conducted at 10 and 12 V. At no point did the final temperature of the liquid in the electrochemical cell exceed 37 °C.

5.2.2 Electrochemical Disinfection Procedure

5.2.2.1 Cell and pump operation with saline and dye

For experiments with the organic dye in a NaCl solution, the saline mixed with the dye was introduced in the storage tank. Thereafter the pump was turned on and samples were drawn and regular intervals. This experiment was conducted for two different electrode voltages: 4 V, and 12 V. Electrochemical treatment causes the discoloration of organic dye. The discoloration was used as a qualitative visual indicator to detect presence of CCS and ROS.

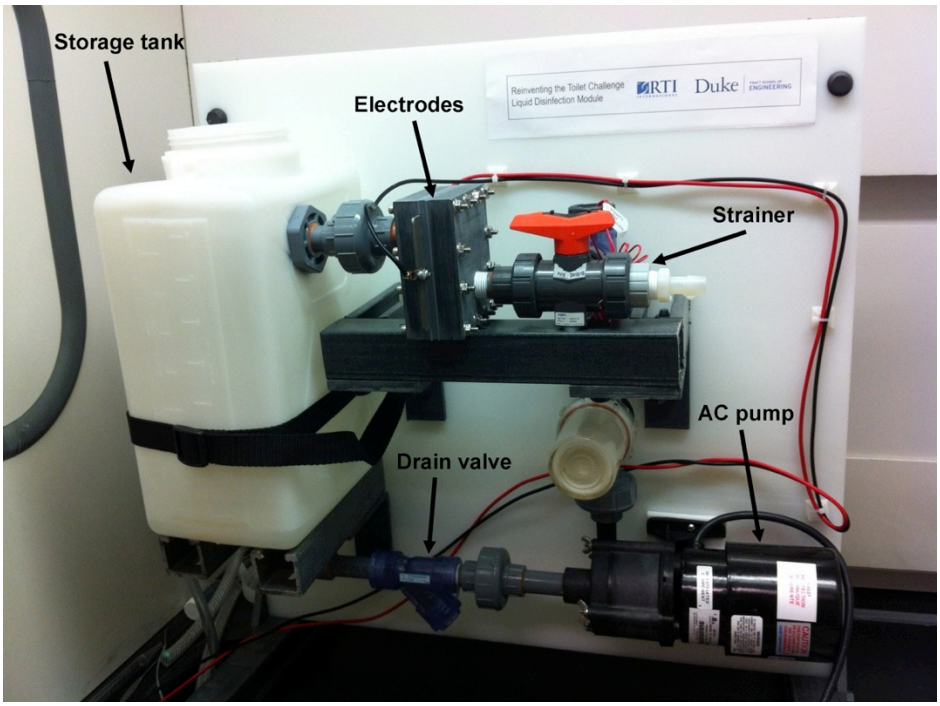

Figure 39: Disinfection system setup (167)

5.2.2.2 Cell and pump operation with synthetic urine and *E. Coli*

At the initiation of the experiment, the E. Coli spiked urine was introduced into the storage tank. Thereafter, the pump was turned on and the urine was allowed to flow through the loop to enable complete mixing. The first sample was drawn from the storage tank using a sterile pipette prior to applying a voltage to the electrodes. The voltage to the electrodes was then turned on to and samples were drawn in a similar manner using a new sterile pipette at each specified time during the course of the experiment. The current values were obtained from the integrated ammeter of the DC power supply that powered the electrodes. A reading was taken with each sample. The reported current is the average of these currents normalized by electrode area. The first

set of experiments utilized only synthetic urine and E. Coli and were conducted at four different electrode voltages: 6 V, 8 V, 10 V and 12 V. The next set of experiments utilized synthetic urine with E. Coli and synthetic fecal matter (1% w/v and 2 % w/v) and were conducted at 6 V.

5.2.2.3 Sample Plating

The samples drawn during the experiment were diluted serially in sterile 8 g/L NaCl solution in a 1:10 ratio. For each dilution, 100 μL were plated onto a 100 x 15 mm Petri dishes prepared with RAPID'E. coli 2 (Bio-Rad Inc.) which is a chromogenic medium for enumeration and differentiation of generic E. coli. The serial dilution and plating of three samples from each experiment was repeated to confirm the CFU count. The plates were incubated at 37 °C for 24 hours after which the colony forming units (CFUs) on each plate were counted and reported as CFU/100 mL.

5.2.2.4 Total chlorine measurement

Total chlorine was measured using DR890 colorimeter (Hach) and the N,N-diethyl-p-phenyldiamine (DPD) method (Hach test #8167). Volume of each sample was 10 mL. The test is approved by the United States Environmental Protection Agency and detects presence of free chlorine (hypochlorous acid/hypochlorite ion) and combined chlorine (monochloramine and dichloramine) (170).

5.2.3 Results and Discussion

5.2.3.1 Saline solution with organic dye

Photographs of aliquot samples versus treatment time for the experiment with Green No. 3 dye and two different electrode voltages are shown in Figure 40 (167). For each voltage, there was a reduction in color intensity over treatment time. The electrochemically-generated oxidants caused chemical breakdown of the dye, leading to this discoloration. The lowest voltage applied in this series of experiments was 4 V, which was higher than the formation potential of chlorine, ozone, chlorine dioxide and hydroxyl radical at BDD electrodes (44). This means that most of the disinfecting oxidants are generated even at the lowest tested electrode potential. The electrode current monotonically increased over the course of the experiment. A typical range over the course of the experiment was 3.4 A to 3.7 A for the experiment at 6 V. This indicates removal of non-conductive organic content and most likely caused the discoloration of the dye. Thus faster discoloration at 12 V as compared to 4 V suggests that the overall rate of oxidants generation is higher at higher voltages. Further experimentation will be required to determine if at higher voltages the kinetics of the oxidation reactions were faster and/or if new oxidants were being generated.

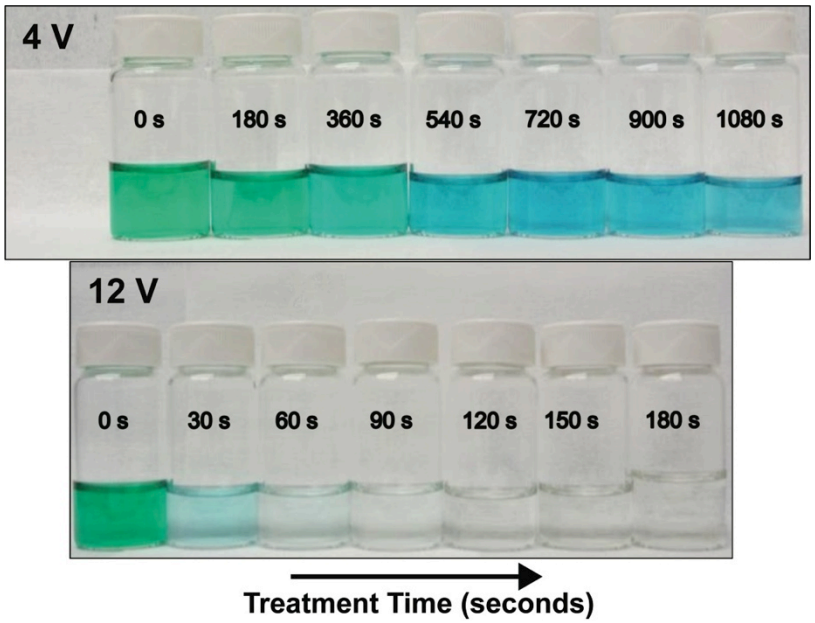

Figure 40: Reduction in color concentration versus treatment time for saline with organic dye for 4 V and 12 V electrode voltage (167)

5.2.3.2 Synthetic urine spiked with *E. Coli*

Figure 41 (167) shows a plot of viable E. Coli cell counts versus treatment time for different electrode voltages. In all cases, there was a reduction in E. Coli viable cell concentration over time, reaching values lower than the 1000 CFU/100 mL threshold recommended by the World Health Organization for treated feces and fecal sludge (171). Since the sample volume for each plate was 100 μL, the detection limit is 1000 CFU/100 mL, which is the same as the disinfection threshold. Hence a non-detect sample was treated as disinfected.

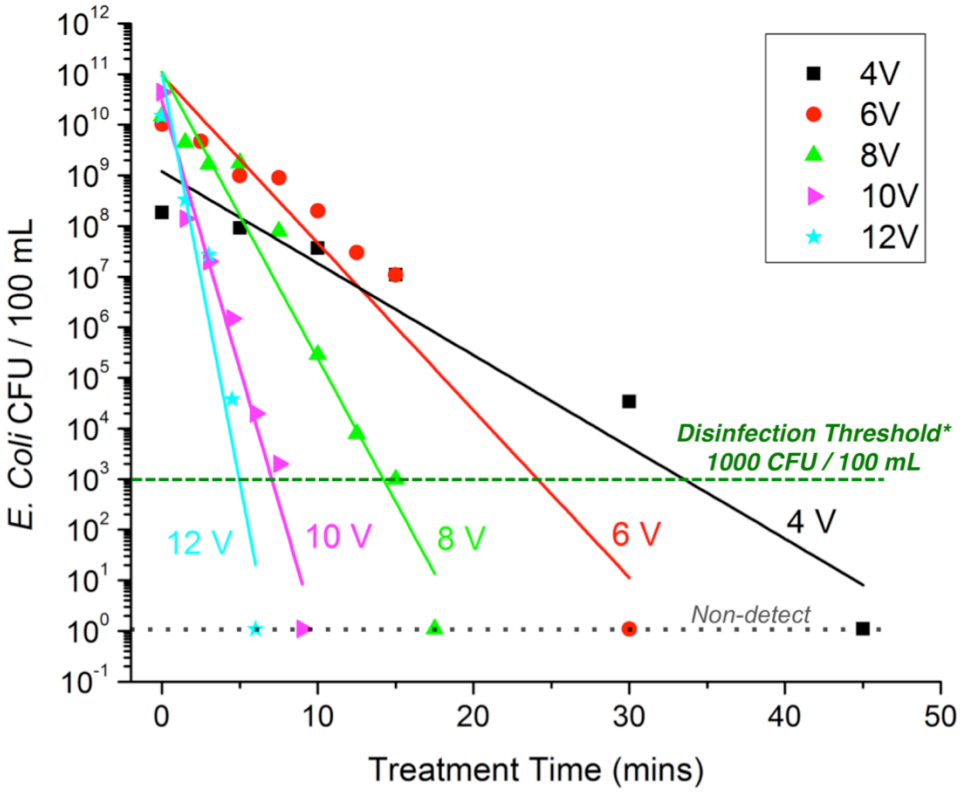

Figure 41: Log-linear plot of E. Coli CFU / 100 mL versus treatment time for different electrode voltages. The dotted line labeled "non-detect" joins points with no CFUs. They have been assigned a value of 1 on the log scale and are not included in the line fitting (167).

A logarithmic function relates the reduction in viable E. Coli to oxidant concentration, treatment time and a rate constant for inactivation as proposed in the Chick-Watson formula (172):

$$\log \frac{N}{N_0} = -k \times C^n \times t \qquad \text{- 9}$$

where,

N = number of microorganisms at contact time t

N0 = number of initial microorganism at contact time, t = 0

k = constant for a specific microorganism and set of conditions

C = disinfectant concentration

N = co-efficient of dilution

The linear relationship between log of bacterial concentration and treatment time is apparent in the plot of log of E. Coli viable count vs. treatment time in Figure 41 (167). The time required for CFU concentration to drop below 10^3 CFU/100 mL (detectable limit), termed the time for disinfection, decreases with increasing voltage. Higher voltages and consequently higher currents favor faster oxidation kinetics since the ROS and CCS are generated at a faster rate. The higher rate and thus concentrations of the oxidants is most likely the cause of faster bacterial inactivation at higher voltages but we cannot rule out that the ratio of oxidant concentrations could change at the higher voltages. This correlation between higher inactivation rate and higher oxidant generation rate at higher electrode voltages has been reported previously for tests in model electrolytes (161).

Figure 42 (167) shows a plot of total chlorine concentration versus treatment time for different electrode voltages. The rate of generation of chlorine was higher at higher voltages. This correlates with the higher rate of *E. Coli* inactivation at higher voltages as shown in Figure 41 (167). This indicates that the electrochemically-generated chlorine-species and the ROS reduce *E. Coli* levels. The free chlorine that is generated reacts with

the available free ammonia in the liquid to form chloramines – monochloramine (NH_2Cl), dichloramine ($NHCl_2$) and trichloramine (NCl_3). Their relative quantities are a function of the chlorine to ammonia (Cl_2:N) weight ratio and solution pH. When certain Cl_2:N (~7:1) ratio is reached, the demand for chlorine is quenched and any excess chlorine will exist as free chlorine (170). The pH range for synthetic urine tested in this study was 7 to 8. As a part of some previous critical experiments, it was observed that free ammonia was generated in the synthetic urine during disinfection due to oxidation of urea and uric acid present in the urine (refer Appendices C and D). This seemed to keep the Cl_2:N ratio low. It also indicates that most of the chlorine in the treated synthetic urine exists mainly as combined chlorine in the form of monochloramine and dichloramine. Monochloramine and dichloramine are also disinfectants and are more stable than hypochloruous acid, which is a weak acid (pKa = 7.6). Thus monochloramine and dichloramine seem to be the main chlorine-related disinfectants responsible for bacterial inactivation in the present study. It has been reported that OH- radicals are also responsible for bactericidal action (173). Since the concentrations of OH^-, H_2O_2 and other oxidants were not measured, their effect on the disinfection rate and efficiency could not be evaluated. The role of such oxidants needs to be investigated further.

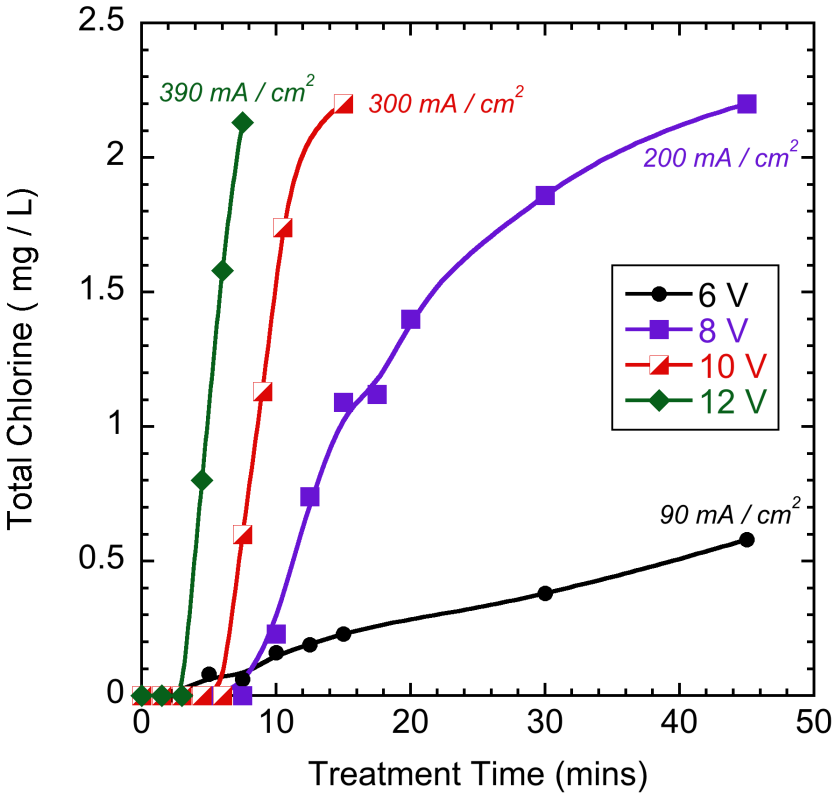

Figure 42: Plot of total chlorine concentration versus treatment time for different electrode voltages. Numbers next to each curve are current densities measured at each voltage (167).

5.2.3.3 Synthetic urine and synthetic fecal matter spiked with *E. Coli*

Synthetic urine mixed with simulant fecal matter and *E. Coli* was also tested to determine the effect of added organic matter and suspended solids on the process. The results are reported in Figure 43 (167). The disinfection time in the presence of fecal matter simulant was similar to the disinfection time without fecal contamination (25-30 minutes). After the completion of these experiments, the BDD and tungsten electrodes were carefully examined under an optical microscope to determine if any scaling or fouling was present. Both electrodes surfaces were found to be free of fouling. This

indicated that fecal matter contamination of up to 2% w/v did not have a significant short-term impact on the disinfection time or the surface quality of the electrodes.

5.2.3.4 Energy data for *E. Coli* disinfection in synthetic urine

The specific energy required for disinfection is defined below (174):

$$E = \frac{V \times I \times t}{L} \qquad \textbf{- 10}$$

where:

E = energy required for disinfection in Wh/L

V = electrode voltage in volts

I = electrode current in amperes

t = time required for disinfection in hours

L = treated volume in liters

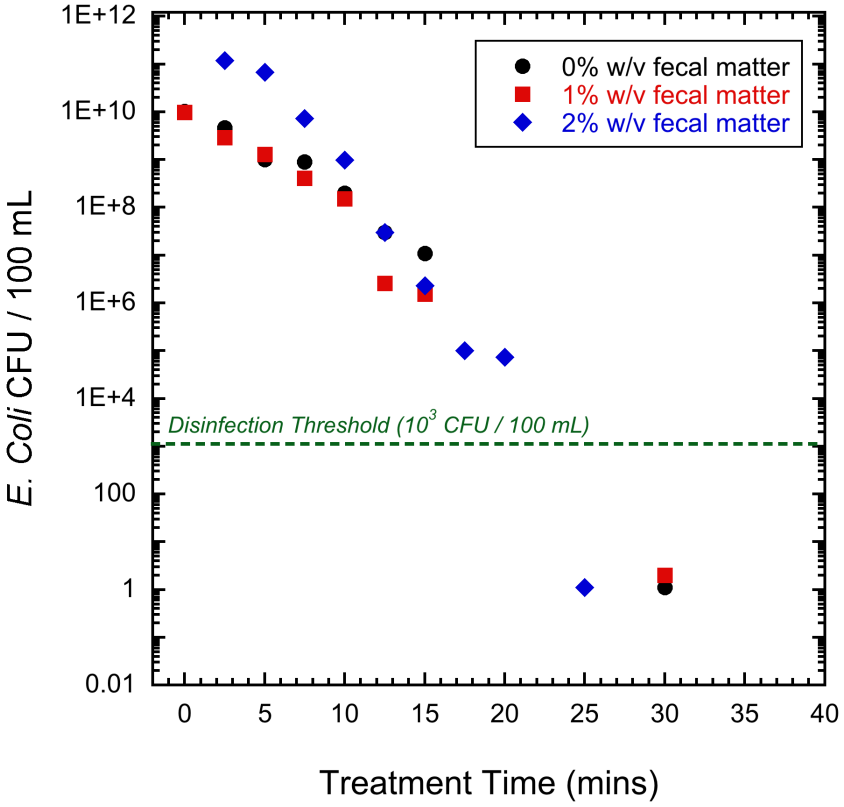

Figure 43: Plot of *E. Coli* in CFU / 100 mL versus treatment time for 0%, 1% and 2% v/w synthetic fecal matter and synthetic urine with *E. Coli* at 6 V electrode voltage (167)

Figure 44 (167) shows a plot of disinfection energy and disinfection time as a function of the electrode voltage. The disinfection time decreased whereas the disinfection energy increased non-linearly with increasing electrode voltage. This suggests that the selection of electrode voltage is a trade-off between disinfection time and disinfection energy. The non-linearity of the plots in Figure 44 (167) could mean that potentially faster kinetics of side reactions involving non-disinfectants such as evolution of oxygen maybe making the disinfection process less efficient especially at higher voltages. The actual time required for urine disinfection during service will depend on

the volume of urine to be disinfected, which is a function of the number of expected users.

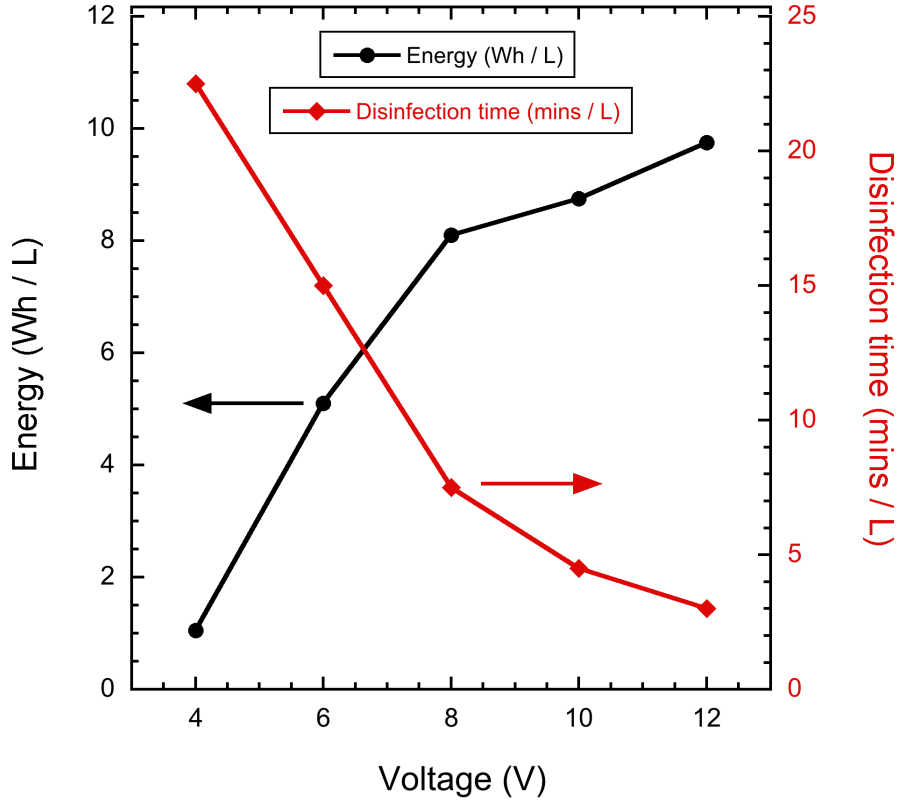

Figure 44: Plot of energy required for disinfection per liter of synthetic urine on Y1 axis and disinfection time per liter for disinfection of synthetic urine on Y2 axis versus electrode voltage (167)

5.2.4 Summary

Synthetic urine spiked with *E. Coli* was disinfected by means of electrochemically-generated ROS and CCS at a BDD anode. This process exhibited an inverse relationship between electrode voltage and time taken for disinfection. Data indicated a linear relationship between the log of *E. Coli* in CFU / 100 mL versus treatment time. The rate of electrochemical generation of total chlorine was found to be

higher at higher voltages. This indicated that total chlorine, along with other oxidants, contributed to the inactivation of *E. Coli*. The energy required for disinfection per liter of urine increased non-linearly with increasing voltage whereas the time required for disinfection per liter decreased exponentially with increasing electrode voltage. Addition of synthetic fecal matter (1% and 2% w/v) did not significantly affect the time for disinfection. Future work will involve investigation of the identification of oxidants other than chlorine species, their rate of generation and evaluation of appropriate electrode voltage in order to optimize energy consumption and disinfection time.

5.3 Minimization of Energy in Electrochemical Disinfection Process

As seen in Figure 44 (167), the energy required for disinfection is higher at higher electrode voltage but the time required for disinfection is also lower. For disinfection of larger volumes of liquid, the electrode voltage should be chosen such that the time required for disinfection and the energy consumed meets the constraints for the application of interest. The toilet design requires all the energy to be derived from solar and thermoelectric power. This section discusses an operation scheme that minimizes energy consumption while still keeping the disinfection time compatible for use by a family of 5 people per day as required by the toilet design requirement.

5.3.1 Experimental Setup and Procedure

5.3.1.1 Synthetic Excreta and Indicator Organism

The recipe and quantity of synthetic urine and *E. Coli* broth used were the same as that in section 5.2.1.3. The indicator organism is *E. Coli* and is the same as the one described in section 5.2.1.4.

5.3.1.2 Experimental Setup

The experimental setup is same as that described in section 5.2.1.5.

5.3.1.3 Testing Procedure

At the initiation of the experiment, the *E. Coli* spiked synthetic urine was introduced into the storage tank. Thereafter, the pump was turned on and the urine was allowed to flow through the loop to enable complete mixing. The first sample was drawn from the storage tank using a sterile pipette prior to applying a voltage to the electrodes. The voltage to the electrodes was then turned on to and samples were drawn in a similar manner using a new sterile pipette at each specified time during the course of the experiment. The electrode voltage and current were noted from the power supply display each time a sample was drawn. In section 5.2.3.2, it was shown that in the same setup, disinfection of synthetic urine was achieved for a given electrode voltage and the corresponding energy consumption was also calculated. In that study the electrode voltage was kept ON until complete disinfection was achieved. This mode of operation is called continuously ON mode. In the present study, two more modes of operation

were investigated. In the short-time mode, voltage was applied to the electrode for a smaller duration of time than that in the continuous ON mode for a given voltage. In the pulsed mode, the same voltage was applied in forms of pulses with varying duty cycle. In the pulsed mode, the total ON time (ON time for each pulse + total number of pulses) was equal to the total ON time in the short-time mode. The three different modes of operation are illustrated in Figure 45

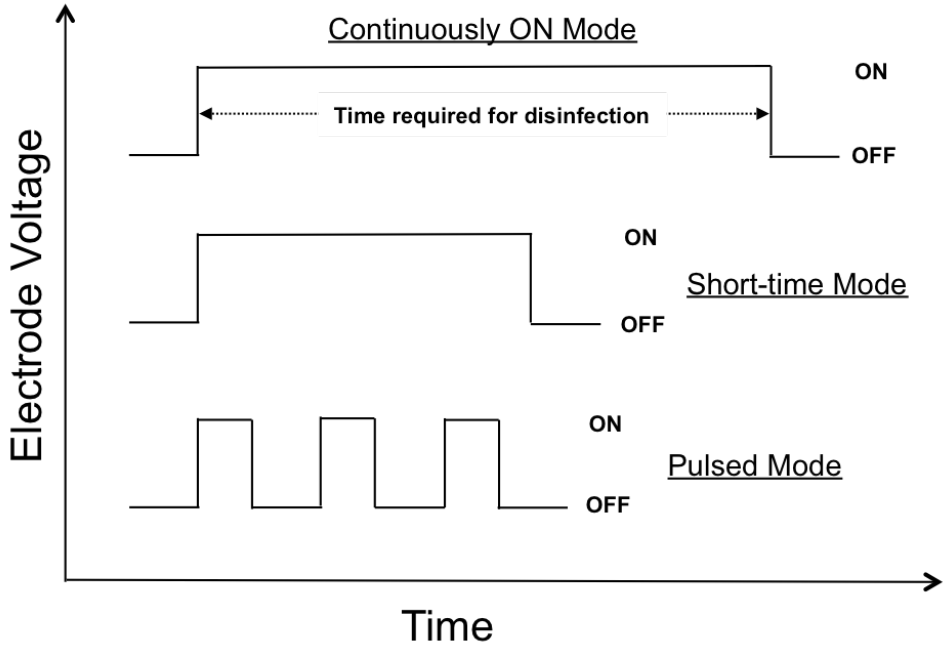

Figure 45: Different modes of applying electrode voltage in order to minimize energy consumption during electrochemical disinfection.

5.3.1.4 Sample Plating and Total Chlorine Measurement

The sample plating procedure and total chlorine measurement procedure was the same as that describes in section 5.2.2.3 and 5.2.2.4.

5.3.1.5 Energy Calculations

The formula for calculating the energy for disinfection is the same as that described in section 5.2.3.4. It should be noted that the time *"t"* in the formula for energy in case of short-time and pulsed mode operation is the total time for which the voltage to the electrode is ON.

5.3.2 Results and Discussion

5.3.2.1 Short-time Mode at 6 V

Previously, with continuous ON mode at 6 V, complete disinfection (no detectable colonies) was achieved in 30 minutes (see section 5.2.3.2). In the short-time mode at 6 V, the electrode voltage was turned OFF after 20 minutes and corresponding bacteria count and total chlorine levels were measured for a total of 100 minutes. Although the electrode voltage was turned OFF after 20 minutes, the pump was kept ON for 100 minutes to allow for mixing of oxidants. Figure 46 shows that there was roughly a 4-log reduction in CFU count in 100 minutes but it did not drop below the WHO recommended level of 10^3/100 mL. The total chlorine concentration was below the detection limit during this time. As discussed previously in section 5.2.3.2, total chlorine (sometimes referred to as "residual chlorine") in form of free and combined chlorine appears after all the demand for chlorine from the organics and nitrogen compounds has been met. Incomplete disinfection in the case of the short-time mode test indicates

that there is still demand for the chlorine and explains the absence of detectable total chlorine.

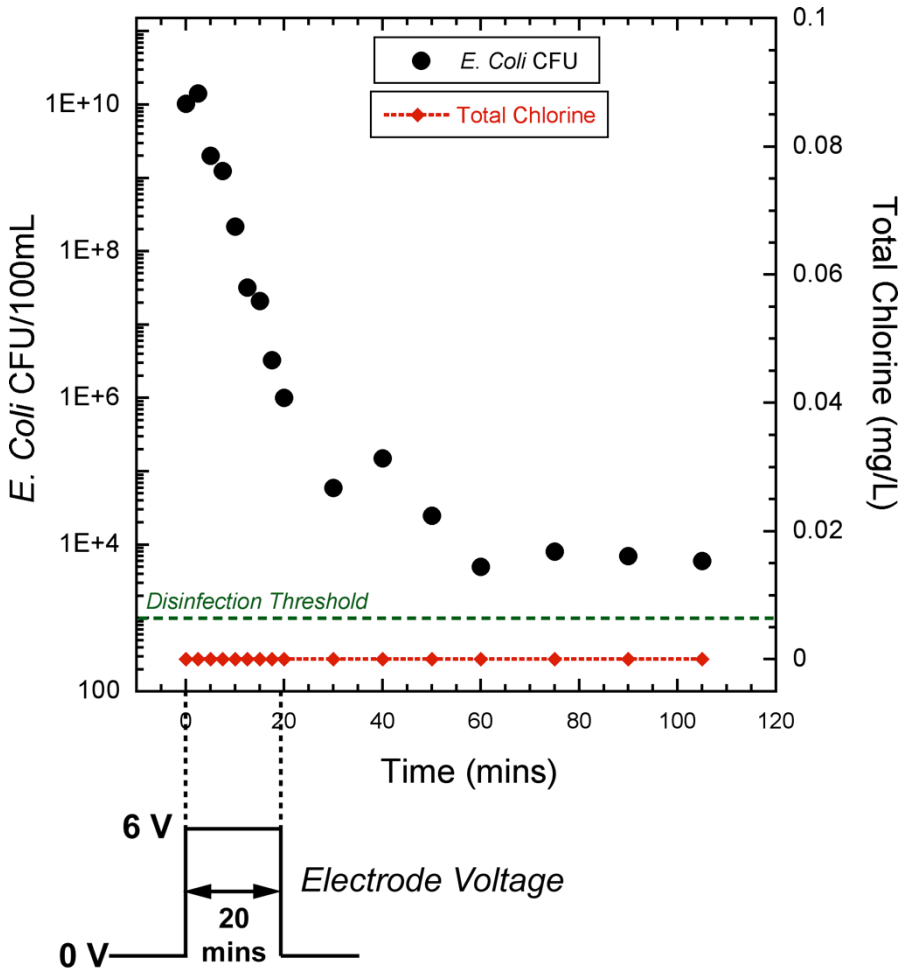

Figure 46: *E. Coli* CFU count and total chlorine concentration versus treatment time for short-time mode operation at 6 V

5.3.2.2 Fifty Percent Duty Cycle Pulsed Mode at 6 V

In the 50% duty cycle pulsed mode operation, electrode voltage was appliedin the form of a pulse with 4 minutes ON time and 4 minutes OFF time. The period was thus 8 minutes. A total of 5 pulses were applied i.e. a total ON time of 20 minutes which

is the same as in the case of the short-time mode. The pump was kept ON for 105 minutes (until the time a spike in total chlorine concentration was detected) to allow for mixing of oxidants. However as seen in Figure 47, the *E. Coli* count fell below the disinfection threshold in 40 minutes.

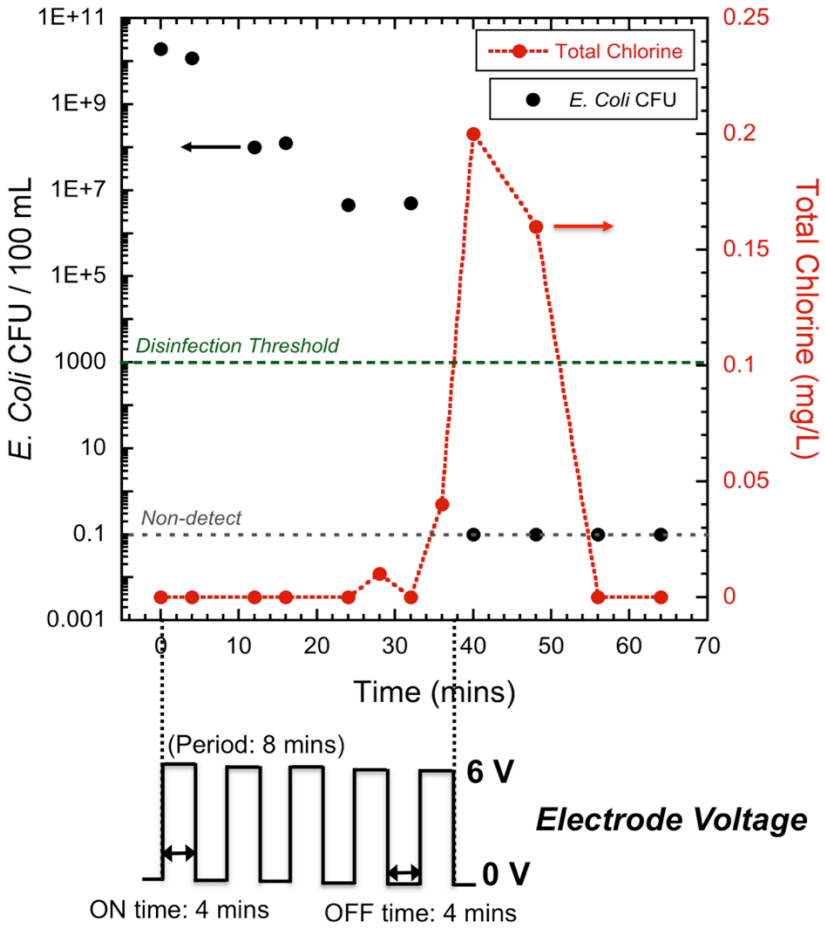

Figure 47: *E. Coli* CFU count and total chlorine concentration versus treatment time for 50% duty cycle pulsed mode operation at 6 V

Note that the disinfection threshold only relates to the WHO guidelines for permissible CFU count and does not relate to the total chlorine concentration. A spike in

the total chlorine concentration was observed at about the same time the CFU count fell below the disinfection threshold. This means that the chlorine demand was met and the organics including *E. Coli* were removed after which total chlorine was detected. The chlorine demand in the urine consumes chlorine species generated during the ON time. It is analogous to incremental dosing with chlorine. In addition to the chlorine demand, in pulsed mode the oxidants are able to diffuse and come in contact with the bacteria during the OFF time. For inactivation of bacteria, there needs to be a certain contact time with a given concentration of oxidants. This contact time depends upon the bacteria and the oxidant concentration. Energy waste is decreased by turning OFF the voltage and allowing for the previously generated chlorine to diffuse and come in contact with the bacteria. It should be noted that in this mode of operation, the total ON time was the same as in the case of short-time mode. However, unlike in the case of the short-time mode, disinfection was achieved.

5.3.2.3 Ten Percent Duty Cycle Pulsed Mode at 6 V

In the 10% duty cycle pulsed mode operation, electrode voltage was applied in the form of a pulse with 48 seconds ON time and 432 seconds OFF time. The period was 8 minutes. A total of 25 pulses were applied; i.e., a total ON time of 20 minutes, which is the same as in the case of the short-time mode and 50% duty cycle pulsed mode. The pump was kept ON for 185 minutes (until the time a spike in total chlorine

concentration was detected) to allow for mixing of oxidants. As seen in Figure 48, the CFU count fell below the disinfection threshold in 100 minutes.

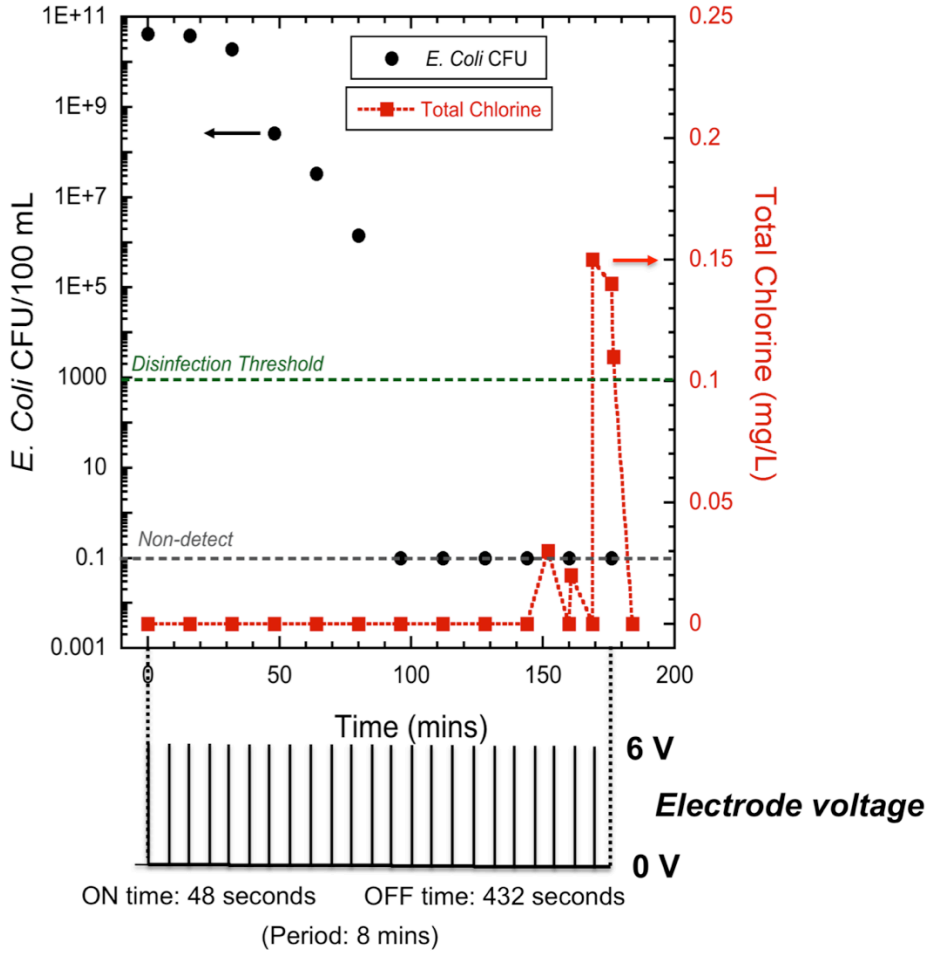

Figure 48: *E. Coli* CFU count and total chlorine concentration versus treatment time for 10% duty cycle pulsed mode operation at 6 V

Just as in case of the 50% duty cycle pulsed mode, a spike in total chlorine concentration was observed. However, the spike appears ~75 minutes after the CFU count drops below the disinfection threshold. This suggests that at 10% duty cycle, it takes longer for the chlorine demand to be met. Inactivation of bacteria by oxidants

depends upon the product of the concentration of the oxidants and their contact time with the bacteria. A smaller ON time may cause a lesser concentration of oxidants to be generated but the longer OFF time allows for more time for diffusion and contact. Thus, as seen in Figure 49, varying duty cycle in the pulsed mode offers a trade-off between oxidant concentration and contact time.

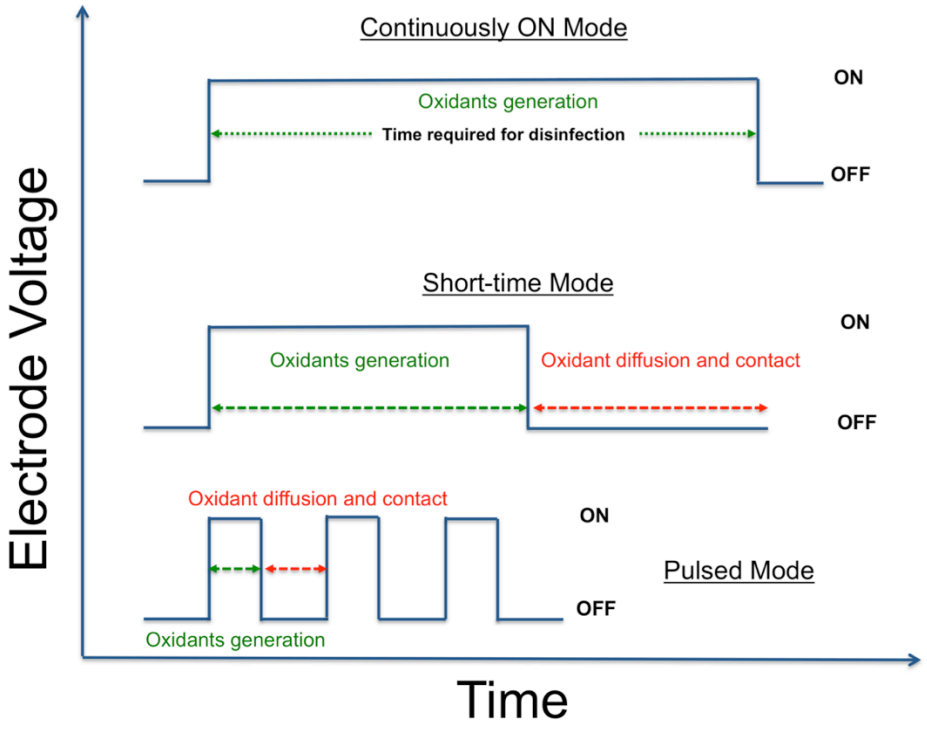

Figure 49: Mechanism of disinfection in different modes of operation

The energy consumed in the electrochemical disinfection process was calculated using the formula stated in section 5.2.3.4. In the energy calculation, the energy consumed by the pump was not included and time *"t"* was the time taken for the CFU count to drop below the disinfection threshold. Note that the electrode voltage was not ON for the entire duration *"t"* but only during the ON time of the pulse. Based on that

duration, Table 8 shows the disinfection energy and disinfection time for each of the operating modes. It is evident that the energy consumed during 10% duty cycle pulsed mode operation is ~66% less than that in continuous ON mode. On the other hand, the time required for disinfection is higher in pulsed mode as compared to the continuous mode.

Table 8: Disinfection energy and time for different operating modes

Mode	Energy for Disinfection (Wh/L)	Time for Disinfection (mins/L)
Continuous ON	5.59	15
Short-time	3.71*	NA*
Pulsed (50% duty cycle)	3.76	20
Pulsed (10% duty cycle)	1.91	48

** Disinfection was not achieved*

It is clear that there are significant energy savings by operating in the pulsed mode. However the time required for disinfection needs to be considered while selecting an operating mode for a given application including such parameters as volume of liquid to be processed and time between uses.

5.3.3 Summary

In summary, it was demonstrated that the energy required for electrochemical disinfection can be greatly reduced by applying the electrode voltage for short-times in a pulsed-fashion. Pulsing allows for diffusion of oxidants and contact time with the pathogens during the OFF time of the pulse. In this mode, the oxidant concentration is optimized for more effective disinfection as compared to the continuous ON mode. With

a 10% duty cycle at 6 V, ~66% energy savings was realized as compared to continuous ON mode at the same voltage for the same volume of urine.

6. Summary, Conclusions and Future Work

Following were the main conclusions from this study:

1. An electrochemical technique was developed to evaluate energy and power performance of individual electrodes for supercapacitor applications. This allowed for comparison of different electrode materials without constructing packaged devices.
2. Carbon nanostructures of varying morphology were synthesized including a novel nanostructures called graphenated carbon nanotubes (g-CNTs). These foliates comprising the g-CNTs were shown to enhance capacitive behavior at various frequencies. .
3. A design of experiments study was conducted to understand the parametric control over the synthesis process in the MPECVD system. Carbon nanostructures with varying morphology were obtained. The effects of morphological variation of these nanostructures on their electrochemical behavior were studied. Local maximum in capacitance was obtained in the temperature regime that resulted in g-CNT growth during this study (925-1050 °C), indicating that the presence of graphene-like foliates improves the capacitance of the material.
4. Electrochemical disinfection of human liquid waste by using BDD electrodes and techniques to minimize energy consumption are also discussed. Finally, directions for future work are identified including development of novel CNTs and

preliminary data for photoelectrochemical disinfection of *E. Coli* spiked liquid using TiO_2 nanowires are discussed.

6.1 Summary and Conclusions

6.1.1 Technique to obtain Ragone plot for carbon nanostructure electrodes

A galvanostatic charge-discharge technique was developed to evaluate the energy and power performance, in the form of Ragone plots, of individual nanostructured electrodes in a lab-scale three-terminal electrochemical system. This technique has been adapted from a similar technique developed for evaluation of commercial, packaged two-terminal capacitors. The technique reported in the present work allows for evaluation of energy and power density of individual electrodes rather than a packaged device. It facilitates engineering of electrodes by allowing investigation of individual electrochemical performance for double layer charge storage. Moreover, it allows the construction of a Ragone plot, which allows for comparison with other energy storage systems or materials that employ different technologies such as Li-intercalation, superconducting magnetic energy storage (SMES), and hydrogen fuel cells.

6.1.2 Growth and electrochemical behavior of g-CNTs

The relationship between specific capacitance and both CNT-diameter and inter-CNT spacing was investigated for vertically aligned CNTs. Controlling the pretreatment time during growth in the MPECVD system varied the CNT-diameter and inter-CNT spacing. It was found that the specific capacitance increased from 70 F/g to 228 F/g as the

value of the two morphological parameters decreased. This significant increase in specific capacitance was attributed to an increase in surface area via a reduction in pore size. Based on these results and literature reports, a qualitative trend was proposed that related specific capacitance of carbon materials to their pore size. This relationship spanned the macroporous to nanoporous regime. According to this proposed trend, specific capacitance does not increase monotonically with decreasing pore size. The trend changes because different mechanisms are dominant at different pore size regimes.

6.1.3 Disinfection of human liquid waste using BDD anode

Synthesis of a novel carbon nanostructure described as graphenated CNTs in the MPECVD system was reported. This nanostructure consists of graphene foliates growing on the outer sidewalls of multiwalled CNTs. It was possible to control the density of foliates by controlling the deposition time. The effect of varying g-CNT foliate density on their electrochemical behavior was investigated. It was found that the there was an increase in capacitance and decrease in charge transfer resistance as foliate density increased. To gain a better understanding of the effect of growth parameters on morphology and of morphology (variation in CNT diameter, inter-CNT spacing and foliate density variation in g-CNTs) on properties, a design of experiments study to investigate the range of morphological variation possible in the parametric space for MPECVD growth was conducted. A variety of carbon nanostructures ranging from

vertically aligned CNTs to carbon nanosheets were grown. Electrochemical analysis revealed that specific capacitance increased with increasing defects (peak I_D/I_G Raman ratio). Crystallite size was also calculated from Raman data utilizing the Tuinstra-Koenig (TK) relation. A similar inverse relationship was found to exist between crystallite size and capacitance. Thus higher defect density in MPECVD synthesized carbon nanostructures led to an increase in capacitance.

A BDD anode was employed to disinfect synthetic human liquid waste for application in a new energy-neutral, water-free, additive-free toilet being developed for the developing world. BDD anodes facilitate the electrochemical generation of mixed oxidants, including free and combined chlorine. Some of these oxidants, such as chlorine species and hydroxyl radicals, have disinfection capability. This leads to reduction in *E. Coli* CFU count.

The effect of small quantities of suspended synthetic fecal matter particles was also studied. It was observed that up to 2% w/v fecal matter had no significant effect on disinfection time. Short time and pulsed mode operation for disinfection were studied with the goal of reducing energy consumption during disinfection. There was up to 66% energy saving at a 10% duty cycle (pulsed mode), compared to continuous electrode operation at the same voltage. This increase in efficiency was mainly attributed to the diffusion and higher contact time of oxidants with the bacteria during the OFF time of the pulse train.

6.2 Direction for Future Work

6.2.1 Atomic Layer Deposition on CNTs

Atomic layer deposition (ALD) allows deposition of atomically thin layers onto three-dimensional scaffolds with very precise control. It is a self-limiting process that provides highly conformal coating and has a large chemistry library. There is great potential for atomic layer coated CNTs in various application ranging from solar cells (175) to transistors and logic devices (176). The in-house ALD capability employed in this study allowed for deposition of a variety of materials, such as TiO_2, Pt, and RuO_2, onto CNTs, g-CNTs, and CNSs. A TEM image of CNTs coated with a thin layer of TiO2 using ALD shows the conformal nature and uniformity of the film (Figure 50).

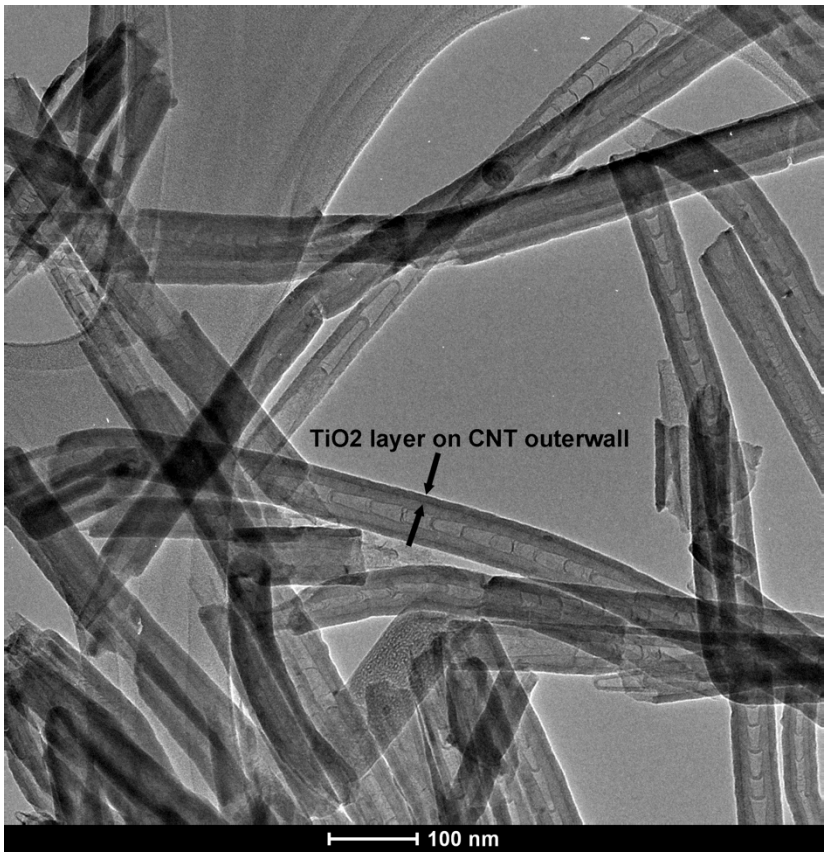

Figure 50: TEM image of multiwalled CNTs coated with TiO_2 using ALD

Pt ALD coated g-CNTs have potential application as neural stimulation electrodes and anode material for mixed oxidant generation. g-CNTs coated with a thin layer of high-k materials can potentially mitigate leakage current through foliate edges and serve as a good electrode for supercapacitors. Similarly, ALD coatings of pseudocapacitive materials on CNTs and g-CNTs can greatly improve specific capacitance. I recommend that ALD be utilized for coating MWCNT with pseudocapacitive material such as MnO_2 or RuO_2 to enhance capacitive performance.

Furthermore, ALD coating with dielectric material such as Al_2O_3 on g-CNTs can be used to minimize leakage from foliates.

6.2.2 Photoelectrochemical Disinfection using TiO_2 nanowires

Preliminary work has been performed to evaluate whether photoelectrochemical (PEC) disinfection is a viable technique for disinfection of human liquid waste. Solar energy is the most abundant source of energy available on earth Figure 51 (177). If this readily available source of energy is harnessed PEC generation of oxidants, the need for external electrical overpotential is reduced, thereby significantly increasing energy efficiency.

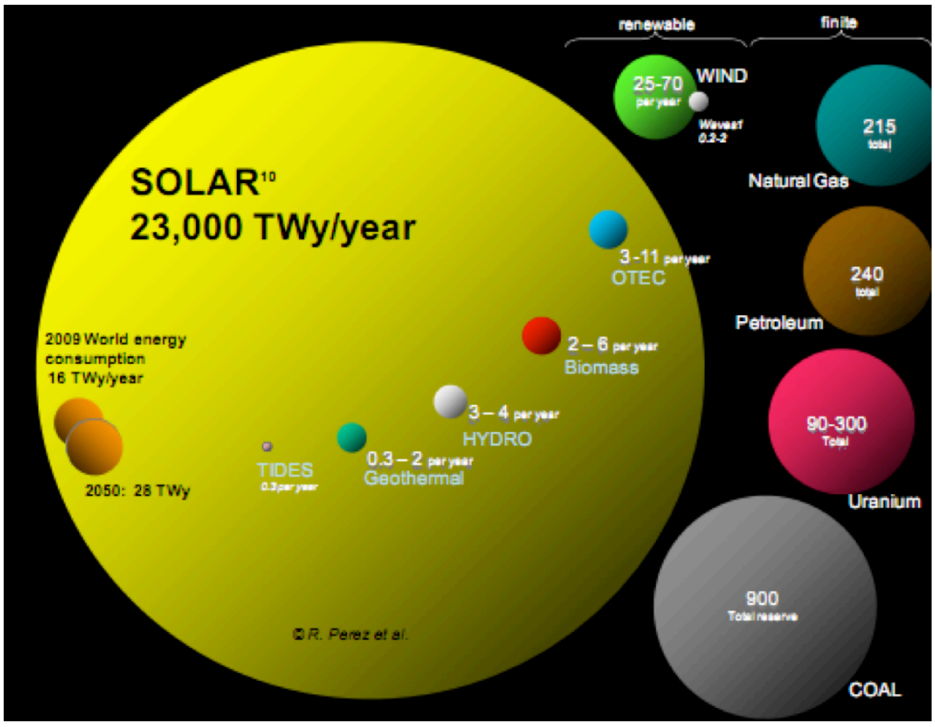

Figure 51: Solar energy output compared to other sources of energy on earth (177)

The electrode used to evaluate PEC disinfection was TiO_2 nanowires on a fluorine doped tin oxide (FTO) substrate (see Figure 52). The setup included a three terminal electrochemical cell with a window to shine simulated solar light obtained from a Xenon light source with 1.5 airmass filter with an intensity of 100 mW/cm^2. The counter electrode was Pt mesh and the reference electrode was Ag/AgCl (sat'd.). Initially, the PEC electrode was tested with 200 mL 9 g/L NaCl solution, 9 g/L NaCl solution with 0.5 M urea, and synthetic urine from the recipe describes in section 5.2.1.3. No bacteria were added.

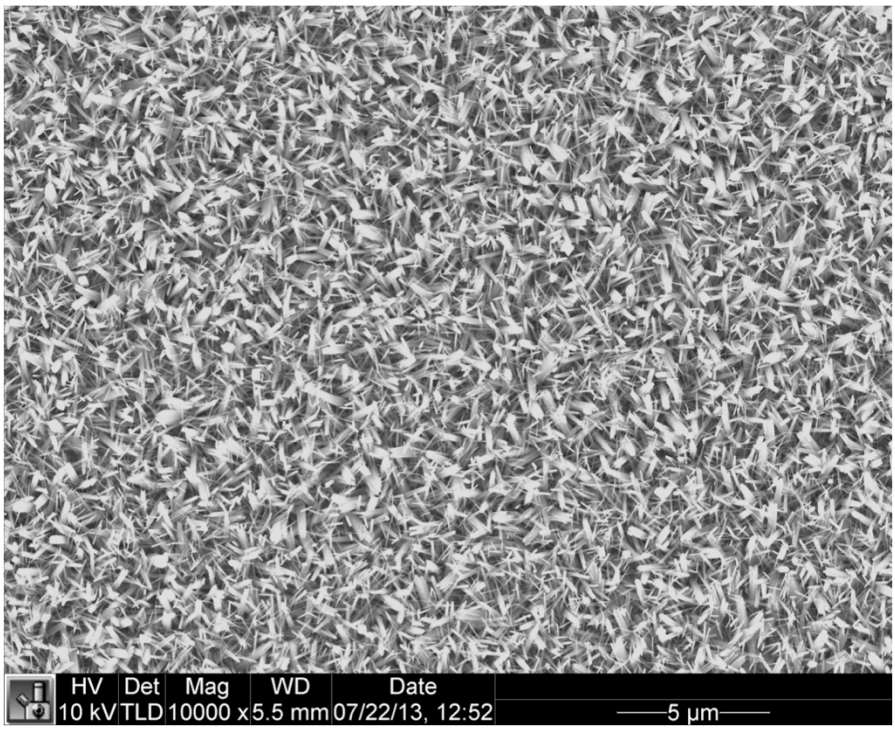

Figure 52: SEM image of PEC electrode consisting of TiO_2 nanowires on FTO substrate (top view)

An external bias of 0.2 V was applied on the working electrode versus the reference electrode. Samples were drawn at regular intervals after the start of the experiment to measure the total chlorine concentration using the technique described in section 5.2.2.4. Figure 53 shows a plot of total chlorine concentration versus treatment time for a TiO_2-FTO PEC electrode in various electrolytes as described above.

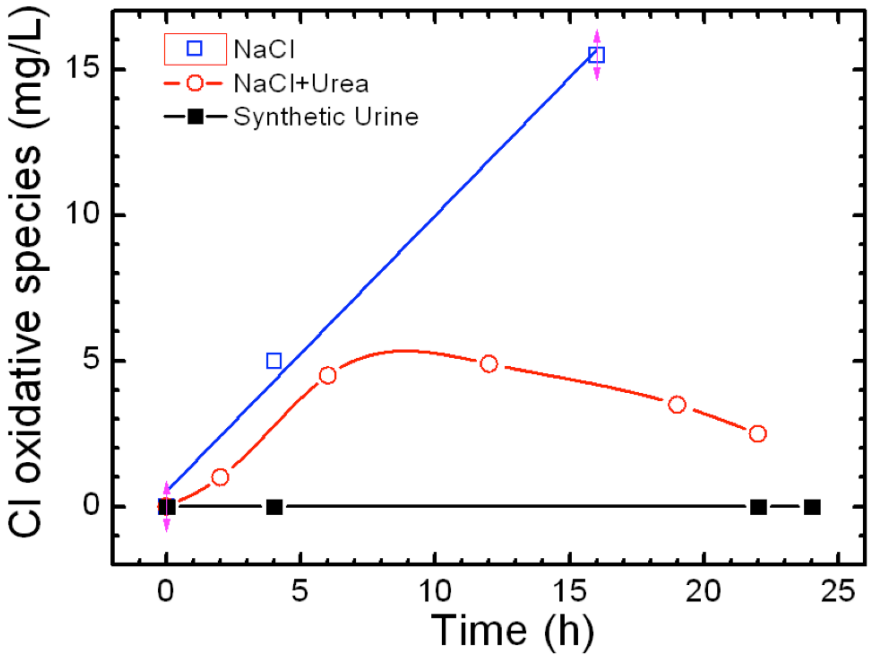

Figure 53: Total chlorine concentration versus treatment time for TiO_2-FTO electrode in 9 g/L NaCl, 9 g/L NaCl + 0.5 M urea, and synthetic urine.

The rate of generation of chlorine species was highest with NaCl. The urea present in NaCl + urea has a lower oxidation potential than chlorine evolution and hence the rate of chlorine species generation was lower. Finally, synthetic urine consists of uric acid apart from urea and other chemicals. Uric acid also has an oxidation potential lower

than that of chlorine evolution and so it had the lowest rate of chlorine species generation. Hence the disinfection rate may be lower in urine than NaCl + urea.

To demonstrate PEC disinfection using TiO_2-FTO electrode, 200 mL 9 g/L NaCl solution was spiked with *E. Coli* obtained from centrifuged and washed incubated broth. The starting concentration of *E. Coli* was ~$5x10^{10}$ CFU/100 mL. Figure 54 shows that over a period of 25 hours, the PEC process was able to cause reduction in *E. Coli* CFU count when compared to the control sample kept at ambient dark conditions.

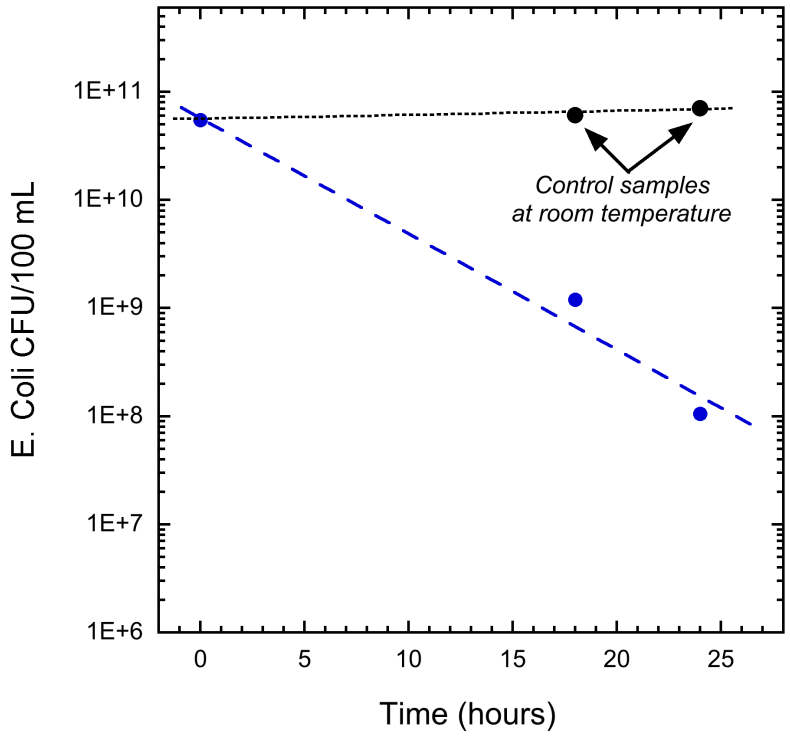

Figure 54: *E. Coli* CFU concentration versus treatment time for PEC treatment 9 g/L saline spiked with *E. Coli* and a control sample kept in ambient dark conditions

While the PEC process can be used for disinfection, even with just NaCl solution the disinfection rate was not very high. It would be even lower when tested in synthetic

urine due to the side reactions of oxidation of urea and uric acid. Further research is required to select an electrode material that can absorb light across a broad spectrum and generate a photocurrent that can overcome side reactions and generate enough disinfecting oxidants. Moreover, the effect of turbidity due to suspended fecal matter particles will also need to be investigated. Finally, an appropriate electrode material would need to be selected and tested with high volume of turbid human liquid waste that can be treated within a reasonable amount of time.

Appendices

Appendix A: Experimental Details of Design of Experiments Study

The full experimental design incorporated temperature, gas ratio, pretreatment time, deposition time, and catalyst thickness as factors; and capacitance, Raman D/G ratio, CNT diameter, presence of CNTs, presence of CNSs, and second order Raman scattering from Si as responses. The DOE design was full factorial and the roles and ranges of the factors are given in Figure 55. Note that the values of pretreatment time and growth time are natural logarithm values.

Name	Role	Changes	Values		
Temperature	Continuous	Easy	750		1100
Pretreatement Time	Continuous	Easy	1.6		9.1
Gas Ratio	Continuous	Easy	1		8
Catalyst Thickness	Discrete Numeric	Easy	1	5	10
Growth Time	Continuous	Easy	3.4		6.17

Figure 55: Role and ranges of the factors included in the DOE study

Based on these parameters a parameter space was defined using JMP software. The full list of experiments is listed in Table 9.

Table 9: List of runs for design of experiments

Temperature (°C)	Pretreatment Time (s)	Gas Ratio (CH_4:NH_3)	Catalyst Thickness (Å)	Growth Time (s)
750	725.96	1	5	29.96
925	210.61	4.5	5	119.70
1100	4.95	8	1	478.19
925	210.61	4.5	5	119.70
925	4.95	4.5	5	478.19
1100	8955.29	1	1	478.19
925	210.61	1	5	478.19

750	4.95	4.5	10	478.19
750	8955.29	4.5	5	478.19
925	8955.29	1	10	29.96
925	210.61	4.5	5	119.70
1100	210.61	4.5	5	29.96
925	8955.29	8	5	29.96
1100	3018.45	8	10	478.19
750	4.95	1	1	29.96
750	210.61	8	1	478.19
750	4.95	8	5	29.96
1100	4.95	1	10	119.70
1100	8955.29	5	5	119.70
1100	4.95	5	5	119.70
800	8955.29	2	5	119.70
800	4.95	2	5	119.70
800	8955.29	5	5	119.70
800	4.95	5	5	119.70
1100	8955.29	2	5	119.70

Appendix B: Model Electrolyte Study for Electrochemical Analysis of Synthetic and Real Urine

In order to compare the electrochemical properties of synthetic urine with real urine, various electrochemical tests were performed. First, CV scans were performed in a three-terminal cell consisting of a BDD wafer as the working electrode, Pt mesh as counter electrode and saturated Ag/AgCl reference electrode. The electrolytes that were analyzed were synthetic urine (same recipe as in section 5.2.1.3) and real human urine collected anonymously using appropriate protocol. Two types of real urines were used –

(1) fresh human urine (< 48 hours since collection) and (2) stale human urine (> 1 week after collection).

Figure 56 shows the CV scan of the three types of urine. There was a peak in the positive scan at ~0.6 V for synthetic and real fresh urine. This peak was well attenuated for real stale urine. It is likely that the reaction at ~0.6 V was not present in real stale urine. It is important to identify this reaction since it will subvert the applied charge from chlorine and hydroxyl evolution reactions.

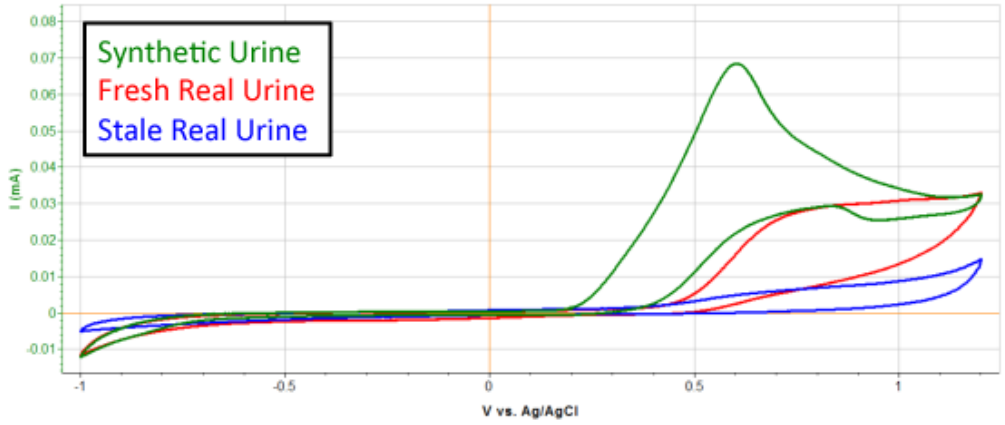

Figure 56: CV scans of synthetic, real fresh and real stale urine in a three-terminal cell at 100 mV/s with BDD wafer as working electrode, Pt mesh as counter and saturated Ag/AgCl as reference electrode.

The solution resistance of synthetic urine, real fresh urine and real stale urine were measured from the Nyquist plots in the same setup as that in Figure 56. Table 10 shows the solution as measured at 200 kHz. It is evident that the solution resistance of synthetic urine and real fresh urine are similar.

Table 10: Solution resistance of synthetic and real human urine from Nyquist plot at 200 kHz

Electrolyte	Solution resistance from Nyquist plot at 200 kHz
Synthetic urine	230 Ω
Real fresh urine	197 Ω
Real stale urine	436 Ω

Appendix C: Oxidation of Uric Acid

To further investigate the reaction causing the peak observed in Figure 56, a three-terminal tests were conducted with BDD working electrode, Pt mesh, saturated Ag/AgCl reference and two different electrolytes – (a) synthetic urine without urea, uric acid, sodium citrate and creatinine and (b) synthetic urine without urea, creatinine and sodium citrate. The corresponding CV scans were compared to the one from CV scan of synthetic urine in Figure 56. The three CV scans are shown in Figure 57. It is evident that the peak appears only in the recipe with uric acid present and is absent in any other electrolyte. Thus the peak at ~0.6 V can be attributed to a reaction associated with uric acid.

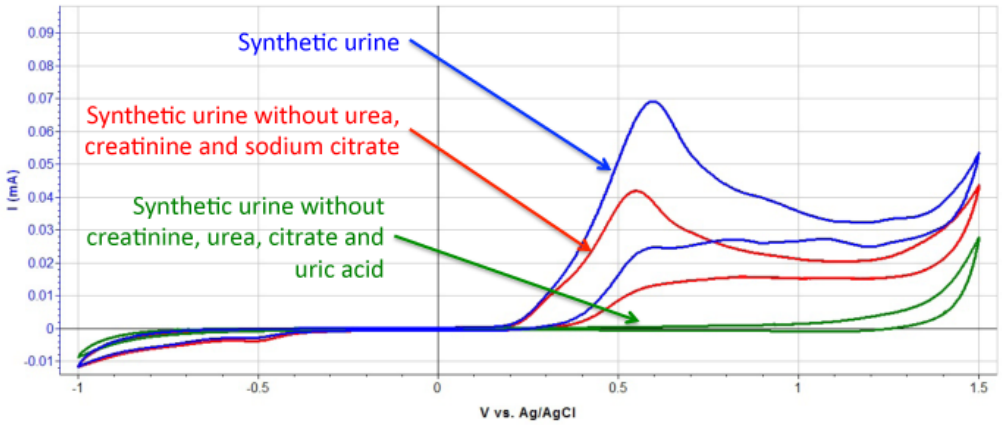

Figure 57: CV scans of model electrolytes of synthetic urine in a three-terminal cell at 100 mV/s with BDD wafer as working electrode, Pt mesh as counter and saturated Ag/AgCl as reference electrode.

The oxidation peak for uric acid has been reported in literature (178). Figure 58 (178) shows the CV scan of 0.3 mM uric acid in 1 M acetic acid at the graphite electrode and standard calomel reference electrode. There is a clear peak ~0.58V that is associated with oxidation of uric acid.

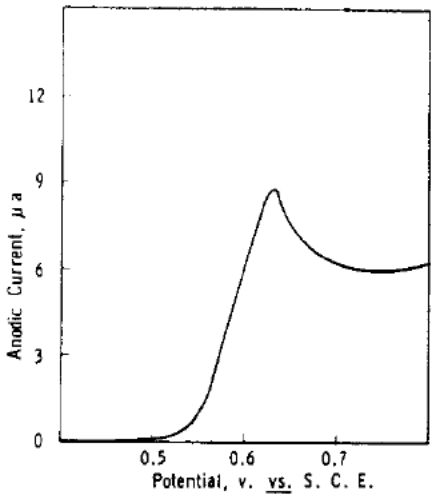

Figure 58: CV scan of 0.3 mM uric acid in 1 M acetic acid at the graphite electrode and standard calomel reference electrode and Pt counter electrode (178)

Appendix D: Oxidation of Urea

Apart from oxidation of uric acid, urea also undergoes oxidation at 0.55 V vs. Hg/HgO (179). Figure 59 (179) shows the anodic CV scan in 5 M KOH and 5 M KOH + 0.33 M urea with a Ti foil working electrode, Pt foil as counter and Hg/HgO reference electrode. It is clear that there is broad anodic wave in the solution containing urea as opposed to that without urea at ~0.55 V.

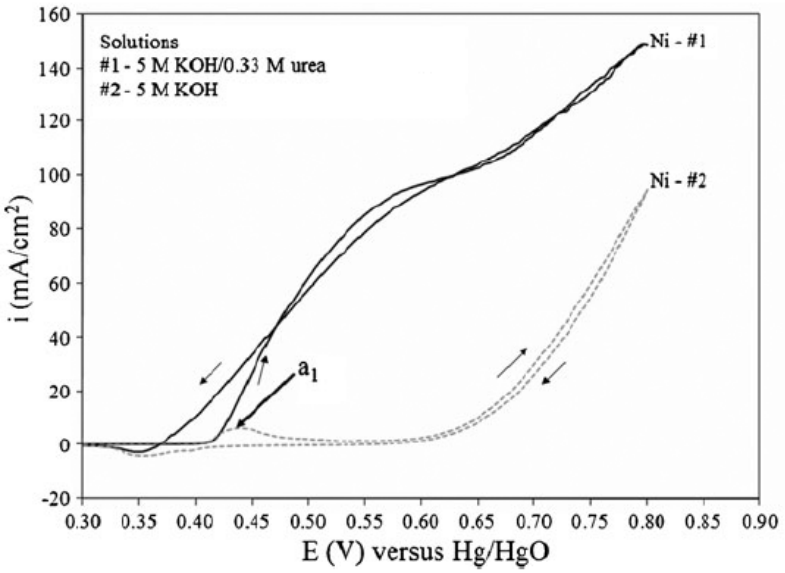

Figure 59: Anodic CV scan in 5 M KOH and 5 M KOH + 0.33 M urea with a Ti foil working electrode, Pt foil as counter electrode and Hg/HgO reference electrode (179)

The oxidation of urea yields nitrogen, hydrogen and carbon dioxide gas according to the equation below:

$$CO(NH_2)_{2(aq)} + H_2O_{(l)} \rightarrow N_{2(g)} + 3H_{2(g)} + CO_{2(g)}$$

Oxidation of urea was investigated by CV at 50 mV/s in 9 g/L NaCl solution and 9 g/L NaCl + 0.5 M urea solutions with BDD wafer as working electrode, Pt mesh as

counter electrode and saturated Ag/AgCl as reference electrode. As seen in the CV scan in Figure 60 there was an increase in background current in the NaCl solution containing urea versus the one without.

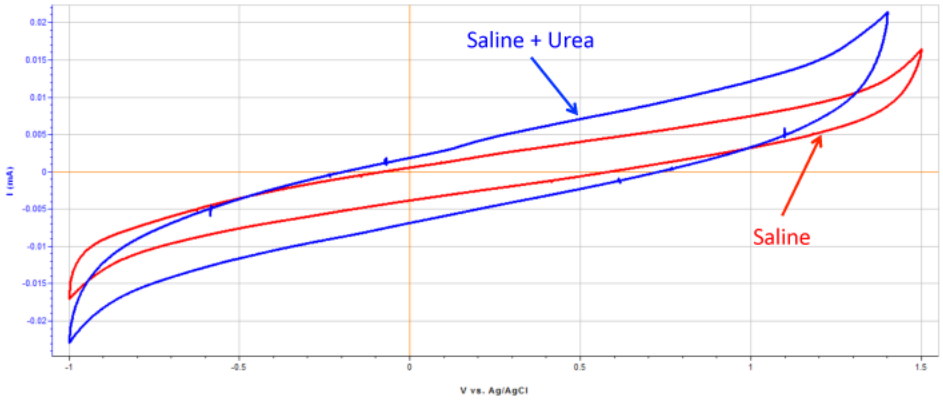

Figure 60: CV scan of 9 g/L NaCl solution and 9 g/L NaCl + 0.5 M urea solutions with BDD wafer as working electrode, Pt mesh as counter electrode and saturated Ag/AgCl as reference electrode

To confirm the presence of urea oxidation peak, EIS data was collected at 0 V versus OCP in the same setup as that in Figure 60. There is a change in the low frequency side of the Nyquist plot at 0.55 V vs. OCV. This change is not observed at 0 V vs. OCV. This confirms the presence of a urea related reaction at 0.55 V vs. OCV.

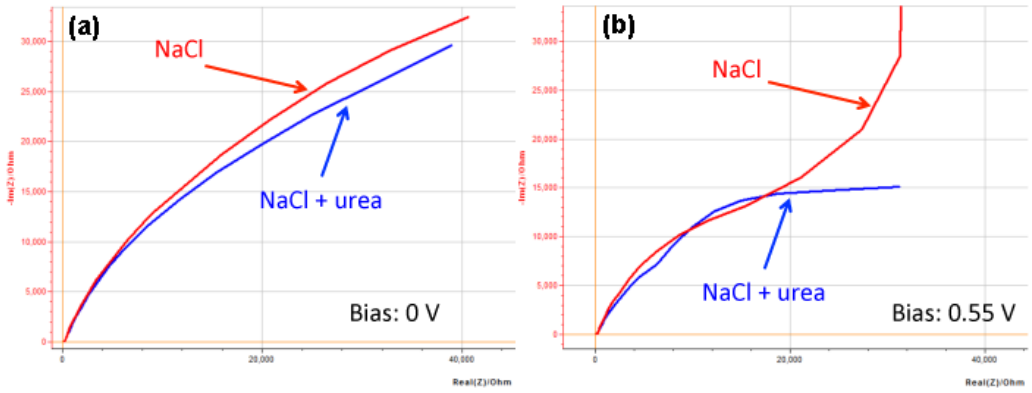

Figure 61: Nyquist plot of 9 g/L NaCl solution and 9 g/L NaCl + 0.5 M urea solutions with BDD wafer as working electrode, Pt mesh as counter electrode and saturated Ag/AgCl as reference electrode at (a) 0 V bias and (b) 0.55 V bias

References

1. http://www.who.int/water_sanitation_health/mdg1/en/, in, World Health Organization (2014).

2. C. L. Kane and E. J. Mele, "Size, Shape, and Low Energy Electronic Structure of Carbon Nanotubes" *Physical Review Letters*, 78 (1997).

3. P. Harris, *Carbon Nanotube Science. Synthesis Properties and Applications*, p. 107, Cambridge University Press (2009).

4. R. Saito, G. Dresselhaus and M. S. Dresselhaus, "Trigonal warping effect of carbon nanotubes" *Physical Review B*, 61 (2000).

5. V. N. Popov, "Carbon nanotubes: properties and application" *Materials Science and Engineering*, 43, 61 (2004).

6. M. B. Kannan Balasubramanian, "Electrochemically functionalized carbon nanotubes for device applications" *Journal of Materials Chemistry*, 18 (2008).

7. P. Poncharal, C. Berger, Y. Yi, ZL Wang and W. A. d. Heer, "Room temperature ballistic conduction in carbon nanotubes" *Journal of Physical Chemistry B*, 106 (2002).

8. M. Meyyappan, L. Delzeit, A. Cassell and D. Hash, "Carbon nanotube growth by PECVD: a review" *Plasma Sources Science and Technology*, 12 (2003).

9. P. Harris, *Carbon Nanotube Science. Synthesis Properties and Applications*, p. 110, Cambridge University Press (2009).

10. A. V. Melechko, V. I. Merkulov, T. E. McKnight, M. A. Guillorn, K. L. Klein, D. H. Lowndes and M. L. Simpson, "Vertically aligned carbon nanofibers and related structures: Controlled synthesis and directed assembly" *Applied Physics Reviews*, 97 (2005).

11. M. L. Terranova, V. Sessa and M. Rossi, "TheWorld of Carbon Nanotubes: An Overview of CVD Growth Methodologies" *Chemical Vapor Deposition*, 12, 315 (2006).

12. H. Cui, O. Zhou and B. R. Stoner, "Deposition of aligned bamboo-like carbon nanotubes via microwave plasma enhanced chemical vapor deposition" *Journal of Applied Physics*, 88 (2000).

13. B. Brown, Growth, Characterization, and Modification of Vertically Aligned Carbon Nanotube Films for Use as a Neural Stimulation Electrode, in, Duke University (2011).

14. A. G. Pandolfo and A. F. Hollenkamp, "Carbon properties and their role in supercapacitors" *Journal of Power Sources*, 157, 11 (2006).

15. E. Frackowiak and F. Beguin, "Carbon materials for the electrochemical storage of energy in capacitors" *Carbon*, 39, 937 (2001).

16. K. H. An, W. S. Kim, Y. S. Park, Y. C. Choi, S. M. Lee, D. C. Chung, D. J. Bae, S. C. Lim and Y. H. Lee, "Supercapacitors Using Single-Walled Carbon Nanotube Electrodes" *Advanced Materials*, 13 (2001).

17. C. Niu, E. K. Sichel, R. Hoch, D. Moy and H. Tennent, "High power electrochemical capacitors based on carbon nanotube electrodes" *Applied Physics Letters*, 70 (1997).

18. B. E. Conway, *Electrochemical Supercapacitors: Scientific Fundamentals and Technological Applications, p453*, Kluwer Academic/Plenum (1999).

19. Obreja and V. N. Vasile, "On the performance of supercapacitors with electrodes based on carbon nanotubes and carbon activated material—A review" *Physica E*, 40 (2008).

20. Q. Jiang, M. Z. Qu, G. M. Zhou, B. L. Zhang and Z. L. Yu, "A study of activated carbon nanotubes as electrochemical supercapacitors electrode materials" *Materials Letters*, 57 (2002).

21. Y.-T. Kim, Y. Ito, K. Tadai and T. Mitani, "Drastic change of electric double layer capacitance by surface functionalization of carbon nanotubes

" *Applied Physics Letters*, 87 (2005).

22. B. L. Zhang, J. Liang, C. L. Xu, B. Q. Wei, D. B. Ruan and D. H. Wu, "Electric double-layer capacitors using carbon nanotube electrodes and organic electrolyte" *Materials Letters*, 51 (2001).

23. P.-C. Chen, G. Shen, S. Sukcharoenchoke and C. Zhoua, "Flexible and transparent supercapacitor based on In2O3 nanowire/carbon nanotube heterogeneous films" *Applied Physics Letters*, 94 (2009).

24. C. Zhou and S. Kumar, "Functionalized Single Wall Carbon Nanotubes Treated with Pyrrole for Electrochemical Supercapacitor Membranes" *Chemical Materials*, 17 (2005).

25. G. Arabale, D. Wagh, M. Kulkarni, I. S. Mulla, S. P. Vernekar, K. Vijayamohanan and A. M. Rao, "Enhanced supercapacitance of multiwalled carbon nanotubes functionalized with ruthenium oxide" *Chemical Physics Letters*, 376 (2003).

26. H. Jiang, P. S. Lee and C. Li, "3D carbon based nanostructures for advanced supercapacitors" *Energy & Environmental Science*, 6, 41 (2013).

27. F. Zhou, Q. Liu, D. Kang, J. Gu, W. Zhang and D. Zhang, "A 3D hierarchical hybrid nanostructure of carbon nanotubes and activated carbon for high-performance supercapacitors" *Journal of Materials Chemistry A*, 2, 3505 (2014).

28. T. Kim, G. Jung, S. Yoo, K. S. Suh and R. S. Ruoff, "Activated Graphene-Based Carbons as Supercapacitor Electrodes with Macro- and Mesopores" *ACS Nano*, 7, 6899 (2013).

29. C. Zhou, Y. Zhang, Y. Li and J. Liu, "Construction of High-Capacitance 3D CoO@Polypyrrole Nanowire Array Electrode for Aqueous Asymmetric Supercapacitor" *Nano Letters*, 13, 2078 (2013).

30. C. Cui, W. Qian, Y. Yu, C. Kong, B. Yu, L. Xiang and F. Wei, "Highly Electroconductive Mesoporous Graphene Nanofibers and Their Capacitance Performance at 4 V" *Journal of the American Chemical Society*, 136, 2256 (2014).

31. W. Yu, X. Jiang, S. Ding and B. Q. Li, "Preparation and electrochemical characteristics of porous hollow spheres of NiO nanosheets as electrodes of supercapacitors" *Journal of Power Sources*, 256, 440 (2014).

32. C. Zhang, Z. Peng, J. Lin, Y. Zhu, G. Ruan, C.-C. Hwang, W. Lu, R. H. Hauge and J. M. Tour, "Splitting of a Vertical Multiwalled Carbon Nanotube Carpet to a Graphene Nanoribbon Carpet and Its Use in Supercapacitors" *ACS Nano*, 7, 5151 (2013).

33. Y. Bai, M. Du, J. Chang, J. Sun and L. Gao, "Supercapacitors with high capacitance based on reduced graphene oxide/carbon nanotubes/NiO composite electrodes" *Journal of Materials Chemistry A*, 2, 3834 (2014).

34. P. M. Kharade, S. G. Chavan, D. J. Salunkhe, P. B. Joshi, S. M. Mane and S. B. Kulkarni, "Synthesis and characterization of PANI/MnO2 bi-layered electrode and its electrochemical supercapacitor properties" *Materials Research Bulletin*, 52, 37 (2014).

35. C. N. Haas, in *Water Quality and Treatment: A Handbook of Community Water Supplies, Fifth Edition*, 5th ed., McGraw-Hill, Inc (1999).

36. C. A. Martinez-Huitle and E. Brillas, "Electrochemical alternatives for drinking water disinfection" *Angewandte Chemie-International Edition*, 47, 1998 (2008).

37. C. N. Haas, in *From Water Quality and Treatment: A Handbook of Community Water Supplies*, McGraw-Hill, Inc. (1999).

38. J. Xu, M. C. Granger, Q. Chen, J. W. Strojek, T. E. Lister and G. M. Swain, "Peer reviewed: boron-doped diamond thin-film electrodes" *Analytical Chemistry*, 69, 591A (1997).

39. N. Vinokur, B. Miller, Y. Avyigal and R. Kalish, "Electrochemical Behavior of Boron-Doped Diamond Electrodes" *Journal of The Electrochemical Society*, 143, L238 (1996).

40. M. C. Granger, M. Witek, J. Xu, J. Wang, M. Hupert, A. Hanks, M. D. Koppang, J. E. Butler, G. Lucazeau and M. Mermoux, "Standard electrochemical behavior of high-

quality, boron-doped polycrystalline diamond thin-film electrodes" *Analytical Chemistry*, 72, 3793 (2000).

41. K. Nishimura, K. Das and J. Glass, "Material and electrical characterization of polycrystalline boron-doped diamond films grown by microwave plasma chemical vapor deposition" *Journal of applied physics*, 69, 3142 (1991).

42. S. Ferro, A. De Battisti, I. Duo, C. Comninellis, W. Haenni and A. Perret, "Chlorine Evolution at Highly Boron-Doped Diamond Electrodes" *Journal of The Electrochemical Society*, 147, 2614 (2000).

43. T. Yano, D. Tryk, K. Hashimoto and A. Fujishima, "Electrochemical Behavior of Highly Conductive Boron-Doped Diamond Electrodes for Oxygen Reduction in Alkaline Solution" *Journal of The Electrochemical Society*, 145, 1870 (1998).

44. M. Chang, C. Gao and J. Jiang, "Electrochemical oxidation of organic compounds using boron-doped diamond electrode" *Journal of The Electrochemical Society*, 156, E50 (2009).

45. I. Tröster, M. Fryda, D. Herrmann, L. Schäfer, W. Hänni, A. Perret, M. Blaschke, A. Kraft and M. Stadelmann, "Electrochemical advanced oxidation process for water treatment using DiaChem electrodes" *Diamond and Related Materials*, 11, 640 (2002).

46. P. L. Hagans, P. M. Natishan, B. R. Stoner and W. E. O'Grady, "Electrochemical Oxidation of Phenol Using Boron-Doped Diamond Electrodes" *Journal of The Electrochemical Society*, 148, E298 (2001).

47. B. Sarada, T. N. Rao, D. Tryk and A. Fujishima, "Electrochemical oxidation of histamine and serotonin at highly boron-doped diamond electrodes" *Analytical Chemistry*, 72, 1632 (2000).

48. T. N. Rao, I. Yagi, T. Miwa, D. Tryk and A. Fujishima, "Electrochemical oxidation of NADH at highly boron-doped diamond electrodes" *Analytical Chemistry*, 71, 2506 (1999).

49. E. Brillas, B. Boye, I. Sirés, J. A. Garrido, R. M. a. Rodríguez, C. Arias, P.-L. s. Cabot and C. Comninellis, "Electrochemical destruction of chlorophenoxy herbicides by anodic oxidation and electro-Fenton using a boron-doped diamond electrode" *Electrochimica Acta*, 49, 4487 (2004).

50. D. Gandini, E. Mahé, P. A. Michaud, W. Haenni, A. Perret and C. Comninellis, "Oxidation of carboxylic acids at boron-doped diamond electrodes for wastewater treatment" *Journal of applied electrochemistry*, 30, 1345 (2000).

51. T. Christen and M. W. Carlen, "Theory of Ragone plots" *Journal of Power Sources*, 91 (2000).

52. J. R. Miller and A. F. Burke, Electric Vehicle Capacitor Test Procedures Manual, in, Idaho National Engineering Laboratory and U. S. D. o. Energy Editors, 45 (1994).

53. L. R. F. Allen J. Bard, *Electrochemical Methods: Fundamentals and Applications*, p. 27, John Wiley & Sons, Inc (2001).

54. R. H. Baughman, A. A. Zakhidov and W. A. de Heer, "Carbon Nanotubes--the Route Toward Applications" *Science*, 297, 787 (2002).

55. D. Dunn-Rankin, E. Martins Leal and D. C. Walther, "Personal power systems" *Progress in Energy and Combustion Science*, 31 (2005).

56. T. Christen and M. W. Carlen, "Optimizing energy storage devices using Ragone plots" *Journal of Power Sources*, 110 (2002).

57. J. Chmiola, G. Yushin, Y. Gogotsi, C. Portet, P. Simon and P. L. Taberna, "Anomalous Increase in Carbon Capacitance at Pore Sizes Less Than 1 Nanometer" *Science*, 313, 1760 (2006).

58. J. R. Miller and A. F. Burke, Electric Vehicle Capacitor Test Procedures Manual, in, Idaho National Engineering Laboratory, U. S. Department of Energy (1994).

59. A. S. Raut, C. B. Parker and J. T. Glass, "A method to obtain a Ragone plot for evaluation of carbon nanotube supercapacitor electrodes" *Journal of Materials Research*, 25, 1500 (2010).

60. I. Plitz, A. DuPasquier, F. Badway, J. Gural, N. Pereira, A. Gmitter and G. G. Amatucci, "The design of alternative nonaqueous high power chemistries" *Applied Physics A*, 82, 615 (2006).

61. A. Peigney, C. Laurent, E. Flahaut, R. R. Bacsa and A. Rousset, "Specific surface area of carbon nanotubes and bundles of carbon nanotubes" *Carbon*, 39 (2001).

62. H. Cui, Nucleation and growth of nanoscaled one-dimensional materials, in, The University of North Carolina at Chapel Hill (2001).

63. C. Ye, Z. M. Lin and S. Z. Hui, "Electrochemical and Capacitance Properties of Rod-Shaped MnO2 for Supercapacitor" *Journal of The Electrochemical Society*, 152, A1272 (2005).

64. H. Y. Chu, Q. Y. Lai, Y. J. Hao, Y. Zhao and X. Y. Xu, "Study of electrochemical properties and the charge/discharge mechanism for Li4Mn5O12/MnO2-AC hybrid supercapacitor" *Journal of Applied Electrochemistry*, 39 (2009).

65. H.-Y. Chu, Q.-Y. Lai, L. Wang, J.-F. Lu and Y. Zhao, "Preparation of MnO2/WMNT composite and MnO2/AB composite by redox deposition method and its comparative study as supercapacitive materials" *Ionics*, 16, 233 (2010).

66. A. E. Fischer, M. P. Saunders, K. A. Pettigrew, D. R. Rolison and J. W. Long, "Electroless Deposition of Nanoscale MnO2 on Ultraporous Carbon Nanoarchitectures: Correlation of Evolving Pore-Solid Structure and Electrochemical Performance" *Journal of The Electrochemical Society*, 155, A246 (2008).

67. A. S. Raut, C. B. Parker, B. R. Stoner and J. T. Glass, "Effect of porosity variation on the electrochemical behavior of vertically aligned multi-walled carbon nanotubes" *Electrochemistry communications*, 19, 138 (2012).

68. G. G. Wildgoose, C. E. Banks, H. C. Leventis and R. G. Compton, "Chemically modified carbon nanotubes for use in electroanalysis" *Microchimica Acta*, 152, 187 (2006).

69. J. H. Zagal, S. Griveau, K. I. Ozoemena, T. Nyokong and F. Bedioui, "Carbon Nanotubes, Phthalocyanines and Porphyrins: Attractive Hybrid Materials for Electrocatalysis and Electroanalysis" *Journal of Nanoscience and Nanotechnology*, 9, 2201 (2009).

70. J. Li, J. E. Koehne, A. M. Cassell, H. Chen, H. T. Ng, Q. Ye, W. Fan, J. Han and M. Meyyappan, "Inlaid multi-walled carbon nanotube nanoelectrode arrays for electroanalysis" *Electroanalysis*, 17, 15 (2005).

71. D. Lozano-Castello, D. Cazorla-Amoros, A. Linares-Solano, S. Shiraishi, H. Kurihara and A. Oya, "Influence of pore structure and surface chemistry on electric double layer capacitance in non-aqueous electrolyte" *Carbon*, 41, 1765 (2003).

72. A. B. Fuertes, F. Pico and J. M. Rojo, "Influence of pore structure on electric double-layer capacitance of template mesoporous carbons" *Journal of Power Sources*, 133, 329 (2004).

73. H. Yamada, I. Moriguchi and T. Kudo, "Electric double layer capacitance on hierarchical porous carbons in an organic electrolyte" *Journal of Power Sources*, 175, 651 (2008).

74. G. Salitra, A. Soffer, L. Eliad, Y. Cohen and D. Aurbach, "Carbon Electrodes for Double-Layer Capacitors I. Relations Between Ion and Pore Dimensions" *Journal of The Electrochemical Society*, 147, 2486 (2000).

75. J. Zhao, C. Lai, Y. Dai and J. Xie, "Pore structure control of mesoporous carbon as supercapacitor material" *Materials Letters*, 61, 4639 (2007).

76. M. Endo, T. Maeda, T. Takeda, Y. J. Kim, K. Koshiba, H. Hara and M. S. Dresselhaus, "Capacitance and Pore-Size Distribution in Aqueous and Nonaqueous Electrolytes Using Various Activated Carbon Electrodes" *Journal of The Electrochemical Society*, 148, A910 (2001).

77. J. Chmiola, G. Yushin, Y. Gogotsi, C. Portet, P. Simon and P. L. Taberna, "Anomalous Increase in Carbon Capacitance at Pore Sizes Less Than 1 Nanometer" *Science*, 313, 1760 (2006).

78. O. Barbieri, M. Hahn, A. Herzog and R. Kotz, "Capacitance limits of high surface area activated carbons for double layer capacitors" *Carbon*, 43, 1303 (2005).

79. H. Cui, O. Zhou and B. R. Stoner, "Deposition of aligned bamboo-like carbon nanotubes via microwave plasma enhanced chemical vapor deposition" *Journal of Applied Physics*, 88, 6072 (2000).

80. W. S. Rasband, ImageJ, U. S. National Institutes of Health, Bethesda, Maryland, USA, http://imagej.nih.gov/ij/, 1997-2011.

81. Q. Wu, Y. Xu, Z. Yao, A. Liu and G. Shi, "Supercapacitors Based on Flexible Graphene/Polyaniline Nanofiber Composite Films" *ACS Nano*, 4, 1963 (2010).

82. V. Subramanian, H. Zhu and B. Wei, "Synthesis and electrochemical characterizations of amorphous manganese oxide and single walled carbon nanotube composites as supercapacitor electrode materials" *Electrochemistry Communications*, 8, 827 (2006).

83. H. Zhang, G. Cao, Y. Yang and Z. Gu, "Comparison Between Electrochemical Properties of Aligned Carbon Nanotube Array and Entangled Carbon Nanotube Electrodes" *Journal of The Electrochemical Society*, 155, K19 (2008).

84. A. Peigney, C. Laurent, E. Flahaut, R. R. Bacsa and A. Rousset, "Specific surface area of carbon nanotubes and bundles of carbon nanotubes" *Carbon*, 39, 507 (2001).

85. M. C. Henstridge, E. J. F. Dickinson and R. G. Compton, "On the estimation of the diffuse double layer of carbon nanotubes using classical theory: Curvature effects on the Gouy Chapman limit" *Chemical Physics Letters*, 485, 167 (2010).

86. J.-P. Randin and E. Yeager, "Differential Capacitance Study of Stress-Annealed Pyrolytic Graphite Electrodes" *Journal of Electrochemical Society*, 118, 711 (1971).

87. B. R. Stoner, A. S. Raut, B. Brown, C. B. Parker and J. T. Glass, "Graphenated carbon nanotubes for enhanced electrochemical double layer capacitor performance" *Applied Physics Letters*, 99, 183104 (2011).

88. B. Brown, C. B. Parker, B. R. Stoner, W. M. Grill and J. T. Glass, "Electrochemical Charge Storage Properties of Vertically Aligned Carbon Nanotube Films: The Activation-Enhanced Length Effect" *Journal of The Electrochemical Society*, 158, K217 (2011).

89. M. Sevilla, S. Alvarez, T. A. Centeno, A. B. Fuertes and F. Stoeckli, "Performance of templated mesoporous carbons in supercapacitors" *Electrochimica Acta*, 52, 3207 (2007).

90. C. H. Hou, X. Q. Wang, C. D. Liang, S. Yiacoumi, C. Tsouris and S. Dai, "Molecular-sieving capabilities of mesoporous carbon membranes" *Journal of Physical Chemistry B*, 112, 8563 (2008).

91. J. S. Huang, B. G. Sumpter and V. Meunier, "Theoretical model for nanoporous carbon supercapacitors" *Angewandte Chemie-International Edition*, 47, 520 (2008).

92. J.-P. Randin and E. Yeager, "Differential Capacitance Study of Stress-Annealed Pyrolytic Graphite Electrodes" *Journal of The Electrochemical Society*, 118, 711 (1971).

93. T. Kim, S. Lim, K. Kwon, S.-H. Hong, W. Qiao, C. K. Rhee, S.-H. Yoon and I. Mochida, "Electrochemical Capacitances of Well-Defined Carbon Surfaces" *Langmuir*, 22, 9086 (2006).

94. W. Yuan, Y. Zhou, Y. Li, C. Li, H. Peng, J. Zhang, Z. Liu, L. Dai and G. Shi, "The edge- and basal-plane-specific electrochemistry of a single-layer graphene sheet" *Nature Scientific Reports*, 3 (2013).

95. A. T. Valota, I. A. Kinloch, K. S. Novoselov, C. Casiraghi, A. Eckmann, E. W. Hill and R. A. W. Dryfe, "Electrochemical Behavior of Monolayer and Bilayer Graphene" *ACS Nano*, 5, 8809 (2011).

96. S. F. Cogan, "Neural Stimulation and Recording Electrodes" *Annual Review of Biomedical Engineering*, 10, 275 (2008).

97. S. Natarajan, K. H. Gilchrist, J. R. Piascik, C. B. Parker, J. T. Glass and B. R. Stoner, "Simulation and testing of a lateral, microfabricated electron-impact ion source" *Applied Physics Letters*, 94 (2009).

98. R. Kurt, A. Karimi and V. Hoffmann, "Growth of decorated carbon nano-tubes" *Chemical Physics Letters*, 335, 545 (2001).

99. O. Lourie and H. D. Wagner, "Evidence of stress transfer and formation of fracture clusters in carbon nanotube-based composites" *Composites Science and Technology*, 59, 975 (1999).

100. R. Kurt and A. Karimi, "Influence of Nitrogen on the Growth Mechanism of Decorated C:N Nanotubes" *ChemPhysChem*, 2, 388 (2001).

101. R. Kurt, C. Klinke, J. M. Bonard, K. Kern and A. Karimi, "Tailoring the diameter of decorated C-N nanotubes by temperature variations using HF-CVD" *Carbon*, 39, 2163 (2001).

102. D. Mata, M. Ferro, A. J. S. Fernandes, M. Amaral, F. J. Oliveira, P. M. F. J. Costa and R. F. Silva, "Wet-etched Ni foils as active catalysts towards carbon nanofiber growth" *Carbon*, 48, 2839 (2010).

103. C. B. Parker, A. S. Raut, B. Brown, B. R. Stoner and J. T. Glass, "Three-dimensional arrays of graphenated carbon nanotubes" *Journal of Materials Research*, 27, 1046 (2012).

104. M. Endo, K. Takeuchi, T. Hiraoka, T. Furuta, T. Kasai, X. Sun, C. H. Kiang and M. S. Dresselhaus, "Stacking nature of graphene layers in carbon nanotubes and nanofibres" *Journal of Physics and Chemistry of Solids*, 58, 1707 (1997).

105. M. Zhu, J. Wang, B. C. Holloway, R. A. Outlaw, X. Zhao, K. Hou, V. Shutthanandan and D. M. Manos, "A mechanism for carbon nanosheet formation" *Carbon*, 45, 2229 (2007).

106. D. A. Porter and K. E. Easterling, *Phase Transformations in Metals and Alloys*, p. 514, Chapman & Hall, New York (1992).

107. D. K. Singh, P. K. Iyer and P. K. Giri, "Diameter dependence of interwall separation and strain in multiwalled carbon nanotubes probed by X-ray diffraction and Raman scattering studies" *Diamond and Related Materials*, 19, 1281 (2010).

108. A. C. Ferrari, J. C. Meyer, V. Scardaci, C. Casiraghi, M. Lazzeri, F. Mauri, S. Piscanec, D. Jiang, K. S. Novoselov, S. Roth and A. K. Geim, "Raman spectrum of graphene and graphene layers" *Physical Review Letters*, 97, 187401/1 (2006).

109. C. Faugeras, A. Nerriere, M. Potemski, A. Mahmood, E. Dujardin, C. Berger and W. A. de Heer, "Few-layer graphene on SiC, pyrolitic graphite, and graphene: A Raman scattering study" *Applied Physics Letters*, 92, 011914 (2008).

110. M. S. Dresselhaus, A. Jorio, M. Hofmann, G. Dresselhaus and R. Saito, "Perspectives on Carbon Nanotubes and Graphene Raman Spectroscopy" *Nano Letters*, 10, 751 (2010).

111. L. Chang and C. Hui-Ming, "Carbon nanotubes for clean energy applications" *Journal of Physics D: Applied Physics*, 14, R231 (2005).

112. C. Du, J. Yeh and N. Pan, "High power density supercapacitors using locally aligned carbon nanotube electrodes" *Nanotechnology*, 16, 350 (2005).

113. J. Li and R. J. Andrews, in *Operative Neuromodulation*, p. 537 (2007).

114. S. Minnikanti, P. Skeath and N. Peixoto, "Electrochemical characterization of multi-walled carbon nanotube coated electrodes for biological applications" *Carbon*, 47, 884 (2009).

115. T. D. B. Nguyen-Vu, C. Hua, A. M. Cassell, R. J. Andrews, M. Meyyappan and L. Jun, "Vertically Aligned Carbon Nanofiber Architecture as a Multifunctional 3-D Neural Electrical Interface" *Biomedical Engineering, IEEE Transactions on*, 54, 1121 (2007).

116. T. S. Phely-Bobin, T. Tiano, B. Farrell, R. Fooksa, L. Robblee, D. J. Edell and R. Czerw, in *Materials Research Society Symposium*, p. CC04, Boston (2006).

117. K. Wang, H. A. Fishman, H. Dai and J. S. Harris, "Neural stimulation with a carbon nanotube microelectrode array" *Nano Letters*, 6, 2043 (2006).

118. A. Mazzatenta, M. Giugliano, S. Campidelli, L. Gambazzi, L. Businaro, H. Markram, M. Prato and L. Ballerini, "Interfacing Neurons with Carbon Nanotubes: Electrical Signal Transfer and Synaptic Stimulation in Cultured Brain Circuits" *J. Neurosci.*, 27, 6931 (2007).

119. S. Minnikanti, M. G. Pereira, S. Jaraiedi, K. Jackson, C. M. Costa-Neto, Q. Li and N. Peixoto, "In vivo electrochemical characterization and inflammatory response of multiwalled carbon nanotube-based electrodes in rat hippocampus" *J Neural Eng*, 7, 16002 (2010).

120. S. R. Yeh, Y. C. Chen, H. C. Su, T. R. Yew, H. H. Kao, Y. T. Lee, T. A. Liu, H. Chen, Y. C. Chang and P. Chang, "Interfacing neurons both extracellularly and intracellularly using carbon-nanotube probes with long-term endurance" *Langmuir*, 25, 7718 (2009).

121. A. Kuperman and I. Aharon, "Battery-ultracapacitor hybrids for pulsed current loads: A review" *Renewable and Sustainable Energy Reviews*, 15, 981 (2011).

122. J. M. Miller and P. Mitchell, *Ultracapacitor Applications*, The Institution of Engineering and Technology (2011).

123. K. Yu, G. Lu, Z. Bo, S. Mao and J. Chen, "Carbon Nanotube with Chemically Bonded Graphene Leaves for Electronic and Optoelectronic Applications" *The Journal of Physical Chemistry Letters*, 2, 1556 (2011).

124. R. J. Rice and R. L. McCreery, "Quantitative relationship between electron transfer rate and surface microstructure of laser-modified graphite electrodes" *Analytical Chemistry*, 61, 1637 (1989).

125. R. J. Rice, N. M. Pontikos and R. L. McCreery, "Quantitative correlations of heterogeneous electron-transfer kinetics with surface properties of glassy carbon electrodes" *Journal of the American Chemical Society*, 112, 4617 (1990).

126. J. R. Miller, R. A. Outlaw and B. C. Holloway, "Graphene Double-Layer Capacitor with ac Line-Filtering Performance" *Science*, 329, 1637 (2010).

127. R. L. McCreery, "Advanced Carbon Electrode Materials for Molecular Electrochemistry" *Chemical Reviews*, 108, 2646 (2008).

128. B. R. Stoner, A. S. Raut, B. Brown, C. B. Parker and J. T. Glass, "Graphenated carbon nanotubes for enhanced electrochemical double layer capacitor performance" *Applied Physics Letters*, 99, 183104 (2011).

129. S. F. Cogan, P. R. Troyk, J. Ehrlich, C. M. Gasbarro and T. D. Plante, "The influence of electrolyte composition on the in vitro charge-injection limits of activated iridium oxide (AIROF) stimulation electrodes" *Journal of Neural Engineering*, 4, 79 (2007).

130. C. B. Parker, A. S. Raut, B. Brown, B. R. Stoner and J. T. Glass, "Three-dimensional arrays of graphenated carbon nanotubes" *Journal of Materials Research*, 27, 1046 (2012).

131. K. R. Kneten and R. L. McCreery, "Effects of redox system structure on electron-transfer kinetics at ordered graphite and glassy carbon electrodes" *Analytical Chemistry*, 64, 2518 (1992).

132. M. Inaba, Z. Siroma, A. Funabiki, Z. Ogumi, T. Abe, Y. Mizutani and M. Asano, "Electrochemical Scanning Tunneling Microscopy Observation of Highly Oriented Pyrolytic Graphite Surface Reactions in an Ethylene Carbonate-Based Electrolyte Solution" *Langmuir*, 12, 1535 (1996).

133. S. Flandrois and B. Simon, "Carbon materials for lithium-ion rechargeable batteries" *Carbon*, 37, 165 (1999).

134. J. V. Zoval, J. Lee, S. Gorer and R. M. Penner, "Electrochemical Preparation of Platinum Nanocrystallites with Size Selectivity on Basal Plane Oriented Graphite Surfaces" *The Journal of Physical Chemistry B*, 102, 1166 (1998).

135. C. van Gulijk, K. M. de Lathouder and R. Haswell, "Characterizing herring bone structures in carbon nanofibers using selected area electron diffraction and dark field transmission electron microscopy" *Carbon*, 44, 2950 (2006).

136. J. Wang, M. Zhu, R. Outlaw, X. Zhao, D. Manos, B. Holloway and V. Mammana, "Free-standing subnanometer graphite sheets" *Applied Physics Letters*, 85, 1265 (2004).

137. R. Ryoo, S. H. Joo, M. Kruk and M. Jaroniec, "Ordered Mesoporous Carbons" *Advanced Materials*, 13, 677 (2001).

138. S. M. Ubnoske, A. S. Raut, B. Brown, C. B. Parker, B. R. Stoner and J. T. Glass, "Perspectives on the Growth of High Edge Density Carbon Nanostructures: Transitions from Vertically Oriented Graphene Nanosheets to Graphenated Carbon Nanotubes" *Submitted to The Journal of Physical Chemistry C* (2014).

139. B. R. Stoner and J. T. Glass, "Carbon nanostructures: A morphological classification for charge density optimization" *Diamond and Related Materials*, 23, 130 (2012).

140. J.-P. Randin and E. Yeager, "Differential capacitance study on the basal plane of stress-annealed pyrolytic graphite" *Journal of Electroanalytical Chemistry and Interfacial Electrochemistry*, 36, 257 (1972).

141. J.-P. Randin and E. Yeager, "Differential capacitance study on the edge orientation of pyrolytic graphite and glassy carbon electrodes" *Journal of Electroanalytical Chemistry and Interfacial Electrochemistry*, 58, 313 (1975).

142. D. Qu, "Studies of the activated carbons used in double-layer supercapacitors" *Journal of Power Sources*, 109, 403 (2002).

143. B. R. Stoner and J. T. Glass, "Carbon nanostructures: A morphological classification for charge density optimization" *Diamond and Related Materials*, 23, 130 (2012).

144. F. Tuinstra and J. L. Koenig, "Raman Spectrum of Graphite" *The Journal of Chemical Physics*, 53, 1126 (1970).

145. M. J. Matthews, M. A. Pimenta, G. Dresselhaus, M. S. Dresselhaus and M. Endo, "Origin of dispersive effects of the Raman D band in carbon materials" *Physical Review B*, 59, R6585 (1999).

146. http://abettertoilet.org/toilet-technologies/ in, RTI International (2014).

147. M. Diao, X. Y. Li, J. D. Gu, H. C. Shi and Z. M. Xie, "Electron microscopic investigation of the bactericidal action of electrochemical disinfection in comparison with chlorination, ozonation and Fenton reaction" *Process Biochemistry*, 39, 1421 (2004).

148. I. Tröster, M. Fryda, D. Herrmann, L. Schäfer, W. Hänni, A. Perret, M. Blaschke, A. Kraft and M. Stadelmann, "Electrochemical advanced oxidation process for water treatment using DiaChem electrodes" *Diamond and Related Materials*, 11, 640 (2002).

149. M. Panizza and G. Cerisola, "Application of diamond electrodes to electrochemical processes" *Electrochimica Acta*, 51, 191 (2005).

150. H. B. Martin, A. Argoitia, U. Landau, A. B. Anderson and J. C. Angus, "Hydrogen and Oxygen Evolution on Boron-Doped Diamond Electrodes" *Journal of The Electrochemical Society*, 143, L133 (1996).

151. J.-H. Chang, T.-J. Yang and C.-H. Tung, "Performance of nano- and nonnano-catalytic electrodes for decontaminating municipal wastewater" *Journal of Hazardous Materials*, 163, 152 (2009).

152. A. Kraft, "Electrochemical Water Disinfection: A Short Review. Electrodes using Platinum group metal oxides" *Platinum Metals Review*, 52, 177 (2008).

153. J. Jeong, C. Kim and J. Yoon, "The effect of electrode material on the generation of oxidants and microbial inactivation in the electrochemical disinfection processes" *Water Research*, 43, 895 (2009).

154. A. M. Polcaro, A. Vacca, M. Mascia, S. Palmas, R. Pompei and S. Laconi, "Characterization of a stirred tank electrochemical cell for water disinfection processes" *Electrochimica Acta*, 52, 2595 (2007).

155. C. Rabinovitch and P. S. Stewart, "Removal and inactivation of Staphylococcus epidermidis biofilms by electrolysis" *Applied and Environmental Microbiology*, 72, 6364 (2006).

156. X. Xing, X. Zhu, H. Li, Y. Jiang and J. Ni, "Electrochemical oxidation of nitrogen-heterocyclic compounds at boron-doped diamond electrode" *Chemosphere*, 86, 368 (2012).

157. G. E. Stoner, G. L. Cahen, M. Sachyani and E. Gileadi, "The Mechanism Of Low-frequency AC Electrochemical Disinfection" *Bioelectrochemistry and Bioenergetics*, 9, 229 (1982).

158. L. R. Arias and L. Yang, "Inactivation of Bacterial Pathogens by Carbon Nanotubes in Suspensions" *Langmuir*, 25, 3003 (2009).

159. H. Li, X. Zhu and J. Ni, "Inactivation of Escherichia coli in Na2SO4 electrolyte using boron-doped diamond anode" *Electrochimica Acta*, 56, 448 (2010).

160. Y. Yao, Y. Kubota, T. Murakami, T. Ochiai, H. Ishiguro, K. Nakata and A. Fujishima, "Electrochemical inactivation kinetics of boron-doped diamond electrode on waterborne pathogens" *Journal of Water and Health*, 9, 534 (2011).

161. V. Schmalz, T. Dittmar, D. Haaken and E. Worch, "Electrochemical disinfection of biologically treated wastewater from small treatment systems by using boron-doped diamond (BDD) electrodes - Contribution for direct reuse of domestic wastewater" *Water Research*, 43, 5260 (2009).

162. G. Perez, P. Gomez, R. Ibanez, I. Ortiz and A. M. Urtiaga, "Electrochemical disinfection of secondary wastewater treatment plant (WWTP) effluent" *Water Science and Technology*, 62, 892 (2010).

163. M. Wu, G. Zhao, M. Li, L. Liu and D. Li, "Applicability of boron-doped diamond electrode to the degradation of chloride-mediated and chloride-free wastewaters" *Journal of Hazardous Materials*, 163, 26 (2009).

164. T. Furuta, H. Tanaka, Y. Nishiki, L. Pupunat, W. Haenni and P. Rychen, "Legionella inactivation with diamond electrodes" *Diamond and Related Materials*, 13, 2016 (2004).

165. A. M. Polcaro, A. Vacca, M. Mascia and F. Ferrara, "Product and by-product formation in electrolysis of dilute chloride solutions" *Journal of applied electrochemistry*, 38, 979 (2008).

166. J. A. Carlisle and O. Auciello, Ultrananocrystalline diamond, in *Electrochemical Society Interface*, p. 28 (2003).

167. A. S. Raut, G. B. Cunningham, C. B. Parker, E. J. Klem, B. R. Stoner, M. A. Deshusses and J. T. Glass, "Electrochemical Disinfection of Human Urine for Water-Free

and Additive-Free Toilets Using Boron-Doped Diamond Electrodes" *ECS Transactions*, 53, 1 (2013).

168. L. Barker, S. Pallante, H. Eisenberg, J. Joule, G. Becker and J. Howard, "Simple synthetic and natural urines have equivalent anticalcifying properties" *Investigative Urology*, 12, 79 (1974).

169. J. R. Burns and B. Finlayson, "A proposal for a standard reference artificial urine in in vitro urolithiasis experiments" *Investigative Urology*, 18, 167 (1980).

170. Alternative Disinfectants and Oxidants, in, United States Environmental Protection Agency (1999).

171. World Health Organization, Guidelines for the safe use of wastewater, excreta and greywater, in (2006).

172. Y.-j. Lee and S.-h. Nam, "Reflection on Kinetic Models to the Chlorine Disinfection for Drinking Water Production" *The Journal of Microbiology*, 40, 119 (2002).

173. M. A. Rodrigo, P. Canizares, A. Sanchez-Carretero and C. Saez, "Use of conductive-diamond electrochemical oxidation for wastewater treatment" *Catalysis Today*, 151, 173 (2010).

174. M. I. Kerwick, S. M. Reddy, A. H. L. Chamberlain and D. M. Holt, "Electrochemical disinfection, an environmentally acceptable method of drinking water disinfection?" *Electrochimica Acta*, 50, 5270 (2005).

175. A. Kongkanand, R. M. Domínguez and P. V. Kamat, "Single wall carbon nanotube scaffolds for photoelectrochemical solar cells. Capture and transport of photogenerated electrons" *Nano Lett*, 7, 676 (2007).

176. A. Javey, H. Kim, M. Brink, Q. Wang, A. Ural, J. Guo, P. McIntyre, P. McEuen, M. Lundstrom and H. Dai, "High-κ dielectrics for advanced carbon-nanotube transistors and logic gates" *Nature materials*, 1, 241 (2002).

177. http://solarenergyfactsblog.com/solar-energy-basics/, in, Solar Energy Facts (2014).

178. W. A. Struck and P. J. Elving, "Electrolytic Oxidation of Uric Acid: Products and Mechanism" *Biochemistry*, 4, 1343 (1965).

179. B. K. Boggs, R. L. King and G. G. Botte, "Urea electrolysis: direct hydrogen production from urine" *Chemical Communications*, 4859 (2009).

Biography

Akshay Raut was born on July 5, 1983 in Pune, Maharashtra, India. He obtained his Bachelors degree in Electronics and Telecommunications Engineering in June 2005 from University of Pune. He worked as an embedded software engineer in Aftek Ltd., Pune, India from July 2005 to November 2007. He came to the United States in December 2007 his Masters in Engineering Management from Duke University. He transferred to the doctoral program in Electrical and Computer Engineering at Duke University in August 2008. Concurrently he also gained his Master of Engineering degree from Duke University. During his doctoral program, he worked as a research Scientist intern at RTI International in Durham, NC, USA from May 2013 to December 2013. His research interests include electrochemistry, carbon nanomaterials, energy storage technology, and disinfection and water quality.

Publications:

1. Stephen M. Ubnoske, **Akshay S. Raut**, Billyde Brown, Charles B. Parker, Brian R. Stoner, Jeffrey T. Glass. "Perspectives on the Growth of High Edge Density Carbon Nanostructures: Transitions from Vertically Oriented Graphene Nanosheets to Graphenated Carbon Nanotubes." (Submitted to *The Journal of Physical Chemistry C*) 2014
2. **Akshay S. Raut**, Garry B. Cunningham, Charles B. Parker, Ethan J.D. Klem, Brian R. Stoner, Marc A. Deshusses, Jeffrey T. Glass. "Electrochemical disinfection of human urine for water-free and additive-free toilets using boron doped diamond electrodes." *ECS Transactions*, 53 (17), 2013
3. **Akshay S. Raut**, Charles B. Parker, Brian R. Stoner, Jeffrey T. Glass. "Effect of porosity variation on the electrochemical behavior of vertically aligned multi-walled carbon nanotubes." *Electrochemistry Communications* (19), 2012
4. Charles B. Parker, **Akshay S. Raut**, Billyde Brown, Brian R. Stoner, Jeffrey T. Glass. "Three-dimensional arrays of graphenated carbon nanotubes." *Journal of Materials Research* (27), 2012
5. Brian R. Stoner, **Akshay S. Raut**, Billyde Brown, Charles B. Parker, Jeffrey T. Glass. "Graphenated carbon nanotubes for enhanced electrochemical double layer capacitor performance." *Applied Physics Letters* (99), 2011
6. **Akshay S. Raut**, Charles B. Parker, Jeffrey T. Glass. "A method to obtain a Ragone plot for evaluation of carbon nanotube supercapacitor electrodes." *Journal of Materials Research* (25), 2010